Cell

Structural basis for channel conduction in the pump-like channelrhodopsin ChRmine

Graphical abstract

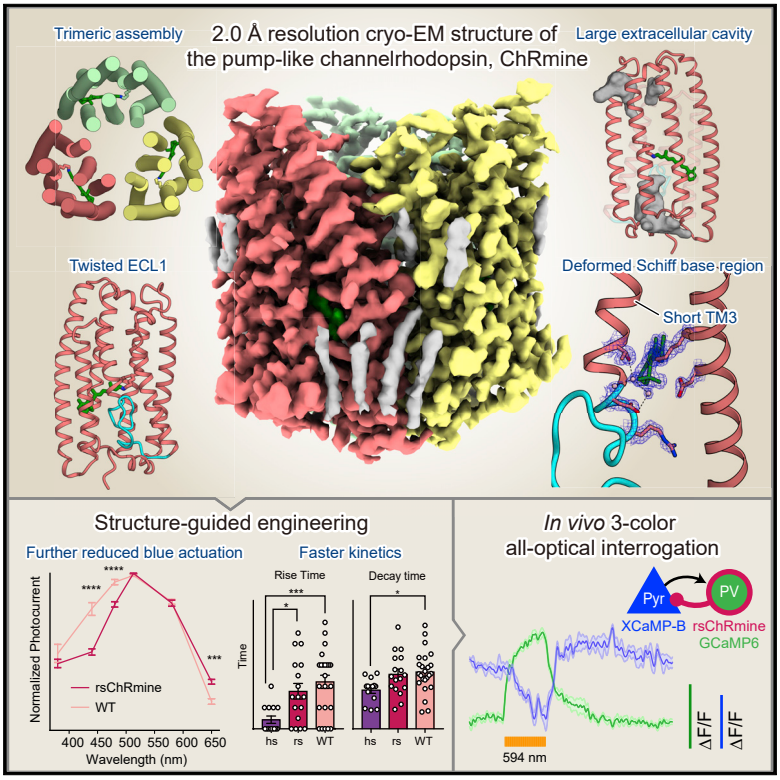

Highlights

- The cryo-EM structure of a pump-like channelrhodopsin, at 2.0 Å resolution
- Identification of key features distinguishing ChRmine from other channelrhodopsins
- Identification of key features distinguishing ChRmine from ion pump rhodopsins
- Structure-guided design of ChRmine variants for all-optical neuroscience

Authors

Koichiro E. Kishi, Yoon Seok Kim, Masahiro Fukuda, ..., Keiichi Inoue, Karl Deisseroth, Hideaki E. Kato

Correspondence

deissero@stanford.edu (K.D.), hekato@bio.c.u-tokyo.ac.jp (H.E.K.)

In brief

Structure of a pump-like channelrhodopsin, ChRmine, reveals design principles and enables the creation of faster and red-light-specific optogenetic tools.

Kishi et al., 2022, Cell *185*, 672–689
February 17, 2022
https://doi.org/10.1016/j.cell.2022.01.007

CellPress

CellPress
OPEN ACCESS

Cell

Article

Structural basis for channel conduction in the pump-like channelrhodopsin ChRmine

Koichiro E. Kishi,[1,17] Yoon Seok Kim,[2,17] Masahiro Fukuda,[1,17] Masatoshi Inoue,[2,17] Tsukasa Kusakizako,[3,17] Peter Y. Wang,[2,17] Charu Ramakrishnan,[4] Eamon F.X. Byrne,[2] Elina Thadhani,[2,5] Joseph M. Paggi,[5] Toshiki E. Matsui,[1] Keitaro Yamashita,[6] Takashi Nagata,[7,8] Masae Konno,[7,8] Sean Quirin,[2] Maisie Lo,[2] Tyler Benster,[2] Tomoko Uemura,[9] Kehong Liu,[9] Mikihiro Shibata,[10,11] Norimichi Nomura,[9] So Iwata,[9,12] Osamu Nureki,[3] Ron O. Dror,[5,13] Keiichi Inoue,[7] Karl Deisseroth,[2,4,14,15,18,*] and Hideaki E. Kato[1,3,8,16,*]

[1]Komaba Institute for Science, The University of Tokyo, Meguro, Tokyo, Japan
[2]Department of Bioengineering, Stanford University, Stanford, CA, USA
[3]Department of Biological Sciences, Graduate School of Science, The University of Tokyo, Bunkyo, Tokyo, Japan
[4]CNC Program, Stanford University, Palo Alto, CA, USA
[5]Department of Computer Science, Stanford University, Stanford, CA, USA
[6]MRC Laboratory of Molecular Biology, Cambridge Biomedical Campus, Cambridge, UK
[7]Institute for Solid State Physics, The University of Tokyo, Kashiwa, Japan
[8]PRESTO, Japan Science and Technology Agency, Kawaguchi, Saitama, Japan
[9]Department of Cell Biology, Graduate School of Medicine, Kyoto University, Kyoto, Sakyo, Japan
[10]WPI Nano Life Science Institute (WPI-NanoLSI), Kanazawa University, Kakuma, Kanazawa, Japan
[11]High-Speed AFM for Biological Application Unit, Institute for Frontier Science Initiative, Kanazawa University, Kakuma, Kanazawa, Japan
[12]RIKEN SPring-8 Center, Kouto, Sayo-cho, Sayo-gun, Hyogo, Japan
[13]Institute for Computational and Mathematical Engineering, Stanford University, Stanford, CA, USA
[14]Howard Hughes Medical Institute, Stanford University, Stanford, CA, USA
[15]Department of Psychiatry and Behavioral Sciences, Stanford University, Stanford, CA, USA
[16]FOREST, Japan Science and Technology Agency, Kawaguchi, Saitama, Japan
[17]These authors contributed equally
[18]Lead contact
*Correspondence: deissero@stanford.edu (K.D.), hekato@bio.c.u-tokyo.ac.jp (H.E.K.)
https://doi.org/10.1016/j.cell.2022.01.007

SUMMARY

ChRmine, a recently discovered pump-like cation-conducting channelrhodopsin, exhibits puzzling properties (large photocurrents, red-shifted spectrum, and extreme light sensitivity) that have created new opportunities in optogenetics. ChRmine and its homologs function as ion channels but, by primary sequence, more closely resemble ion pump rhodopsins; mechanisms for passive channel conduction in this family have remained mysterious. Here, we present the 2.0 Å resolution cryo-EM structure of ChRmine, revealing architectural features atypical for channelrhodopsins: trimeric assembly, a short transmembrane-helix 3, a twisting extracellular-loop 1, large vestibules within the monomer, and an opening at the trimer interface. We applied this structure to design three proteins (rsChRmine and hsChRmine, conferring further red-shifted and high-speed properties, respectively, and frChRmine, combining faster and more red-shifted performance) suitable for fundamental neuroscience opportunities. These results illuminate the conduction and gating of pump-like channelrhodopsins and point the way toward further structure-guided creation of channelrhodopsins for applications across biology.

INTRODUCTION

Light—a crucial energy source and environmental signal—is typically captured by motile organisms using rhodopsins, which are largely classified into two groups: microbial and animal, both consisting of a seven-transmembrane (7TM) protein (opsin) and a covalently bound chromophore (retinal). Light absorption induces retinal isomerization followed by photocycle, a series of photochemical reactions (Zhang et al., 2011; Ernst et al., 2014; Deisseroth and Hegemann, 2017), which in microbial rhodopsins ultimately exerts direct biochemical action (examples include pumps, channels, sensors, and enzymes) (Kandori, 2020; Kato, 2021). Targeted expression of these proteins (especially of the channel- and pump-type) in specific cell types, when applied along with precise light delivery, enables causal study of cellular activity in behaving organisms (optogenetics) (Deisseroth, 2015, 2021; Kurihara and Sudo, 2015).

In optogenetics, cation-conducting channelrhodopsins (cation ChRs or CCRs) are typically used for activation of target cells (Deisseroth and Hegemann, 2017). The initial description of a CCR (*Cr*ChR1 from the chlorophyte *C. reinhardtii*; Nagel et al., 2002) was followed by characterization of variants that were

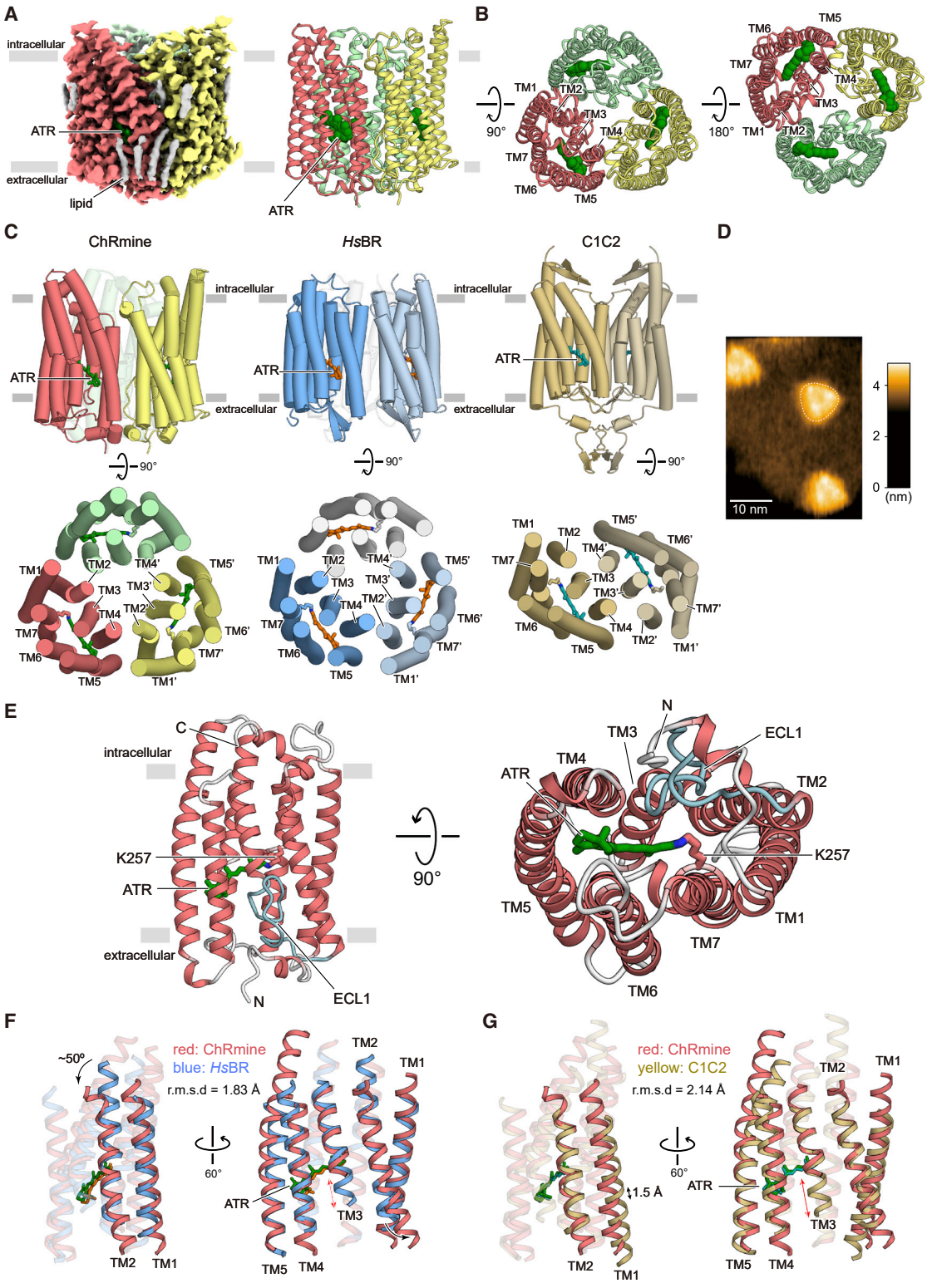

Figure 1. Cryo-EM structure of ChRmine and comparison with *Hs*BR and C1C2

(A) Cryo-EM density map (left) and ribbon representation (right) of ChRmine homotrimer, colored by protomer (red, yellow, and light green), ATR (green), and lipid (gray).

(B) Ribbon representation of the ChRmine homotrimer, viewed from the intracellular (left) and extracellular side (right).

(legend continued on next page)

discovered or designed with new functions spanning ion selectivity, photocurrent amplitude, absorption, sensitivity, and speed (Deisseroth and Hegemann, 2017). Natural CCRs include *Cr*ChR2 (ChR2 from *C. reinhardtii*) (Nagel et al., 2003), VChR1 (ChR1 from *V. carteri*) (Zhang et al., 2008), and Chrimson (from *C. noctigama*) (Klapoetke et al., 2014); these were initially described chiefly from chlorophyte algae, but identification of ChRs from other classes of organism further expanded the toolkit. A subfamily of microbial rhodopsins was reported from the cryptophyte *G. theta* (Govorunova et al., 2016; Yamauchi et al., 2017), identified as CCRs but more homologous to archaeal ion pumps, such as *H. salinarum* bacteriorhodopsin (*Hs*BR). Moreover, unlike chlorophyte CCRs, cryptophyte CCRs share three amino acids on TM3 crucial for outward proton (H^+) pumping (the DTD motif [Inoue et al., 2013]; D85, T89, and D96 in *Hs*BR) and have been referred to as bacteriorhodopsin-like cation ChRs or BCCRs (Sineshchekov et al., 2017; Figures S1A and S1B). ChRmine, a member of this subfamily discovered through structure-guided mining (Marshel et al., 2019), exhibits extremely high current and light sensitivity, as well as a markedly red-shifted spectrum; these properties have enabled all-optical investigation of hundreds of individually specified single neurons (Marshel et al., 2019) and fully non-invasive fast control of deep-brain circuitry (Chen et al., 2021).

A high-resolution structure for this major branch of the channelrhodopsin family would be vital both for understanding structure-function relationships among pump- and channel-type rhodopsins and for designing next-generation optogenetic tools (a process that previously led to the creation of the initial anion-conducting ChRs [ACRs; Berndt et al., 2014, 2016; Kato et al., 2012; Wietek et al., 2014]). Here, we present the cryo-electron microscopy (cryo-EM) structure of ChRmine at 2.0 Å resolution and leverage this information to create variants with faster speed and greater red shift (while preserving high current and light sensitivity), creating opportunities for all-optical neuroscience and for targeted functional analysis in diverse systems.

RESULTS

Structural determination

Our initial efforts to crystallize ChRmine yielded low-resolution crystals; we, therefore, turned to single-particle cryo-EM (Figure S2). The fundamental limitation of single-particle cryo-EM is that images of small membrane proteins in detergent micelles have insufficient features for image alignment in data processing. Indeed, due to the compactness of ChRmine (~35 kDa without extracellular or intracellular domains), particles from an initial cryo-EM dataset were not well aligned and failed to yield 3D reconstructions (Figures S2A–S2C and S2G). To provide a defined feature for image alignment, we generated a conformation-specific antibody against ChRmine, Fab02 (STAR Methods; Figures S3A and S3B). We spectroscopically analyzed the ChRmine-Fab02 complex alongside ChRmine to confirm that Fab02 binding did not affect the photocycle; both ChRmine and ChRmine-Fab02 complexes exhibited K, L_1, L_2, M_1, and M_2 intermediates with similar lifetimes (Figures S3C–S3G and S3L). Using Fab02, the structure of the ChRmine-Fab02 complex in the dark state was determined at an overall resolution of 2.0 Å (Figures S2D–S2F, S2H–S2J, S3H, and S3I; Table S1). The density was of excellent quality, allowing accurate modeling of ChRmine continuously from residues 10 to 279, excluding the disordered N-terminal nine residues and C-terminal 25 residues (Figures S2K–S2R; STAR Methods), and clearly resolved several lipids, water molecules, and the retinal (with the specific all-*trans* retinal conformer confirmed by high-performance liquid chromatography [HPLC]; Figures S2K–S2N, S3J, and S3K). Signals of putative hydrogen atoms were observed in the difference (F_o-F_c) map (Figures S2O and S2P; Yamashita et al., 2021)—not previously achieved for rhodopsins, and now enabled by this high resolution.

Overall structure and comparison with *Hs*BR and C1C2

The cryo-EM density map revealed that the quaternary structure of ChRmine is strikingly different from that of other structure-resolved ChRs (Kato et al., 2012; Figures 1A and 1B). Instead of the classical ChR dimer, ChRmine forms a trimer, and TM2 interacts with TM4 of adjacent protomers as observed in archaeal ion-pumping rhodopsins, including *Hs*BR (Pebay-Peyroula et al., 1997) and *Hs*HR (Kolbe et al., 2000; Figure 1C). To confirm this result under more physiological conditions, we reconstituted ChRmine in a lipid bilayer and performed high-speed atomic force microscopy (HS-AFM), which clearly revealed trimeric structure as well (Figure 1D).

The monomer of ChRmine consists of an extracellular N-terminal domain (residues 10–26), an intracellular C-terminal domain (residues 271–279), and 7 TM domains (within residues 27–270), connected by three intracellular loops (ICL1–ICL3) and three extracellular loops (ECL1–ECL3) (Figure 1E). TM1–TM7 adopt a canonical rhodopsin-like topology with a covalently linked retinal at K257 on TM7, but TM3 markedly diverges from the classical framework, exhibiting an unwound configuration in the middle of the TM region, leading to a long twisting ECL1 (residues 95–115) and a resulting C-shaped structure that is stabilized by an extensive H-bonding network (Figure S2N).

To explore how ChRmine can be structurally similar to ion-pumping rhodopsins and yet function as a channel, we compared ChRmine with an archaeal ion-pumping rhodopsin (*Hs*BR) and a chlorophyte CCR (C1C2, the chimera derived from *Cr*ChR1 and *Cr*ChR2). Consistent with the sequence similarity (Figures S1A and S1B), ChRmine can be better superimposed onto *Hs*BR; the root-mean-square deviation (RMSD) values of ChRmine versus *Hs*BR and C1C2 were measured to be 1.83 and 2.14 Å, respectively (Figures 1F and 1G). Although previous structural work had revealed that TM1, TM2, TM3, and TM7 of CCRs form the ion-conducting pathway within each monomer and that positioning of TM1/2 structurally

(C) Overall structure of ChRmine (left), *Hs*BR (middle), and C1C2 (right), viewed parallel to the membrane (top) and viewed from the intracellular side (bottom).
(D) Representative HS-AFM image of ChRmine.
(E) ChRmine monomer, viewed parallel to the membrane (left), and from the extracellular side (right). ATR (stick model) is green, and ECL1 is cyan.
(F and G) ChRmine (red) superimposed onto *Hs*BR (blue) (F) and C1C2 (yellow) (G) from two angles.

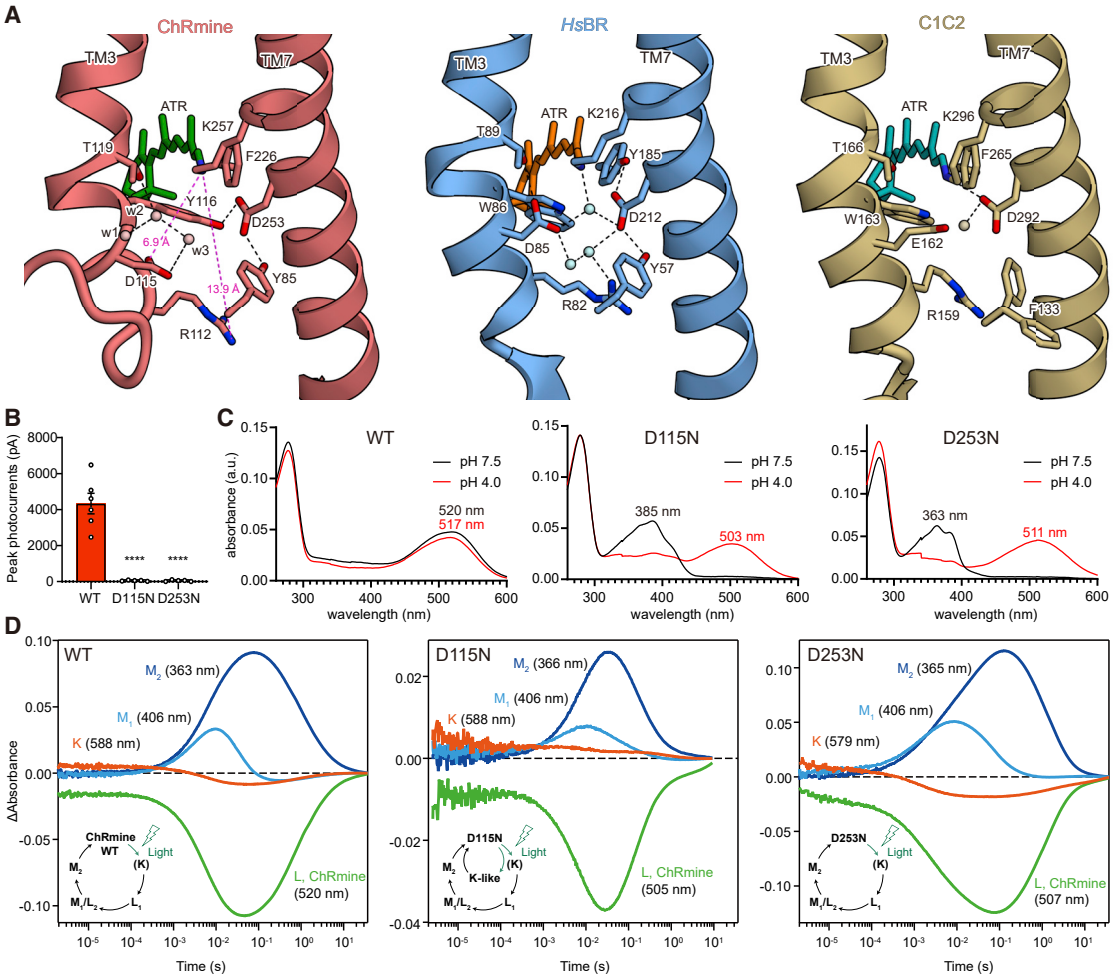

Figure 2. The Schiff base region

(A) The Schiff base regions of ChRmine (left), *Hs*BR (middle), and C1C2 (right). Spheres and black dashed lines represent water molecules and H-bonds, respectively.

(B) Photocurrent amplitudes of wild-type (WT) ChRmine and two mutants. Mean ± SEM (n = 5–6); one-way ANOVA with Dunnett's test. ****p < 0.0001.

(C) Absorption spectra of ChRmine WT (left), D115N (middle), and D253N (right) at pH 7.5 (black) and pH 4.0 (red).

(D) Time-series traces of absorption changes for ChRmine WT (left), D115N (middle), and D253N (right) at 363–366 (blue), 406 (cyan), 505–520 (green), and 579–588 nm (red) probe wavelengths.

distinguishes ChRs from pump-type rhodopsins (Kato et al., 2012), TM1 of ChRmine is positioned more similarly to that of *Hs*BR and is shifted in its entirety by 1.5 Å in ChRmine relative to C1C2 (Figure 1G). The overall positioning (and central region) of TM2 is also similar between ChRmine and *Hs*BR, with the exception that both the intracellular and extracellular regions of TM2 are tilted outward in ChRmine (Figure 1F); these features in TM2 enlarge the cavity within the monomer and may allow ChRmine to function as a CCR.

The Schiff base region

In all microbial rhodopsins, the retinal is covalently bound to a TM7 lysine to form the protonated Schiff base; this positive charge is stabilized by 1–2 carboxylates on the extracellular side (Figure S4A). After photon absorption, the proton is transferred to a carboxylate, a critical step in operation of most ion-transporting rhodopsins; the carboxylate(s) stabilizing the positive charge and receiving the proton (forming the M intermediate) are termed the Schiff base counterion(s) and proton acceptor, respectively (Zhang et al., 2011). To obtain structural insight into ChRmine-channel-gating mechanisms and dynamics, we next focused on the counterion and proton acceptor.

The Schiff base region of ChRmine is strikingly different from that of both types of rhodopsins (*Hs*BR and C1C2; Figure 2A), whereas primary sequence, oligomerization number, and overall monomer structure of ChRmine are similar to those of *Hs*BR (Figures 1E–1G, S1A, and S1B). In *Hs*BR, the protonated Schiff base nitrogen forms a hydrogen (H) bond with a water molecule between the counterions, D85 and D212. D212 is fixed by H-bonds with Y57 and Y185 on TM2 and TM6, respectively, and D85 (which works as the proton acceptor from the Schiff base in the M intermediate; Braiman et al., 1988; Gerwert et al., 1990)

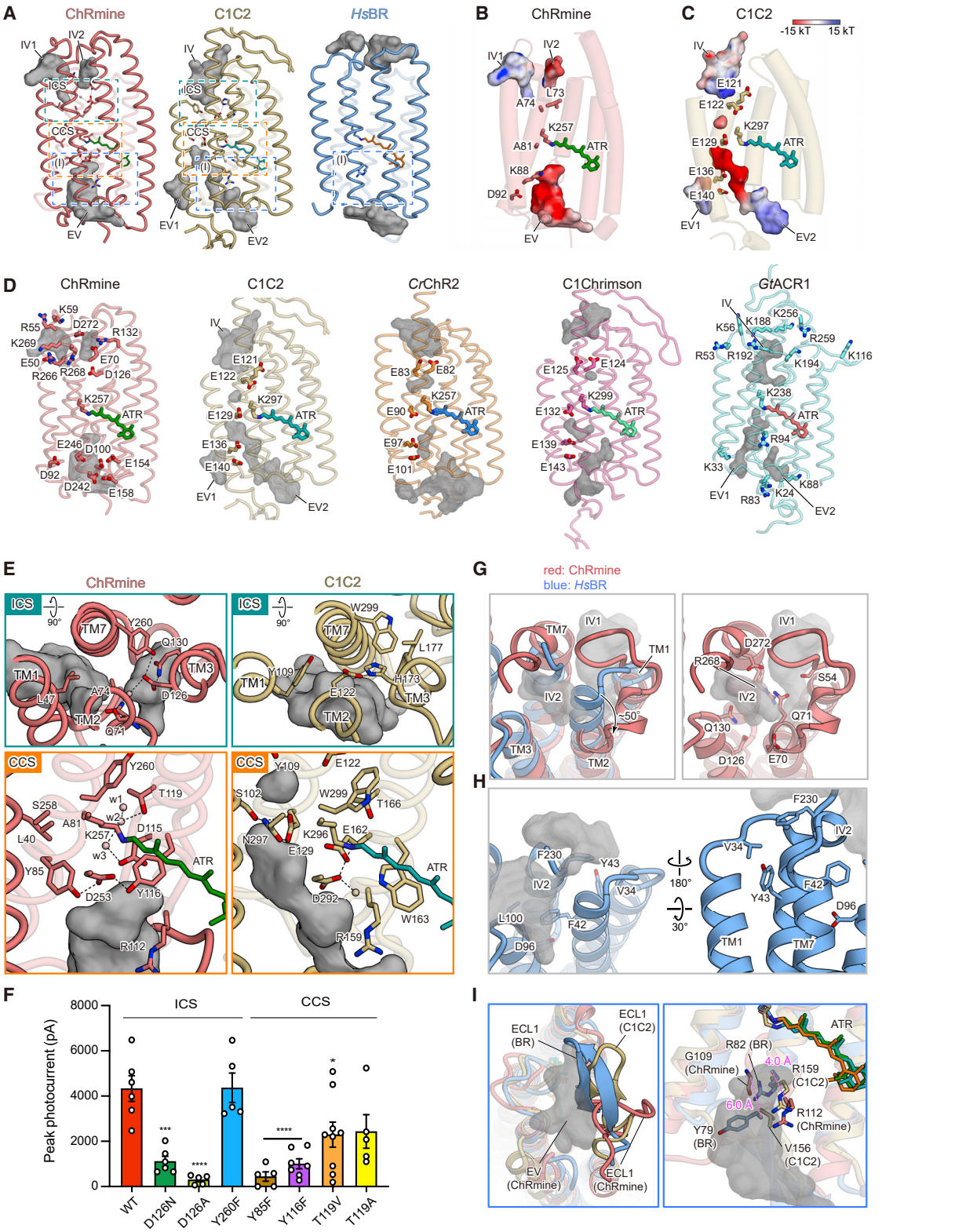

Figure 3. Ion-conducting pathway within the monomer

(A) The extracellular and intracellular vestibules (EV and IV, respectively) of ChRmine (left), C1C2 (middle), and *Hs*BR (right) within the monomer. Vestibules: gray. The intracellular and central constriction sites (ICS and CCS): dashed boxes (green and orange, respectively).

(legend continued on next page)

interacts with R82 via water molecules (Figure 2A). In C1C2, the D85, Y57, and Y185 of *Hs*BR are replaced by E162, F133, and F265, respectively; the Schiff base nitrogen H-bonds with D292, which no longer interacts with F133 and F265 (Figure 2A). D292 acts as the proton acceptor in the M intermediate (Kato et al., 2012; Lórenz-Fonfría et al., 2013), and E162 is dispensable for channel function (Gunaydin et al., 2010; Kato et al., 2012). In contrast, in ChRmine, while the residues corresponding to Y57, R82, D85, and D212 in *Hs*BR are conserved (Y85, R112, D115, and D253), R112 and D115 are displaced far from the Schiff base due to the unwinding of TM3 (Figure 2A); the distances from the Schiff base to R112 and D115 are 13.9 and 6.9 Å, respectively, and such long distances have not been observed in microbial rhodopsin structures (Figures S4B–S4D).

Three water molecules (w1, w2, and w3) occupy the space between the Schiff base and D115 created by the unwinding of TM3. Notably, w2 and w3 are well superposed onto the carboxyl oxygens of D85 in *Hs*BR, suggesting that these waters structurally mimic D85 (Figure S4B) and participate in the counterion complex with D115 and D253. In addition to these structural changes in the TM3 region, the substitutions of Y185 (in *Hs*BR) to F226, and W86 (in *Hs*BR) to Y116, also rearrange the structure in the TM7 region of ChRmine; D253 switches the H-bond from F226 to Y116, and unlike in *Hs*BR, D253 in ChRmine is fixed by two tyrosines (Y85 and Y116) on TM2 and TM3 (Figure 2A).

To explore the function of the counterion and proton-acceptor candidates, D115 and D253, we measured photocurrents of wild-type (WT), D115N, and D253N ChRmine in HEK293 cells; both D115N and D253N abolished photocurrents (Figures 2B and S5A). Spectroscopy revealed strikingly blue-shifted absorption spectra (λ_{max} at pH 7.5 shifting from 520 nm [WT] to 385 nm [D115N] and 363 nm [D253N]), consistent with the loss of function from the baseline deprotonation of the Schiff base (Figure 2C). This is the pattern expected if both D115 and D253 work as Schiff base counterions that must be deprotonated at baseline at physiological pH to stabilize the positive charge of the protonated Schiff base, an idea also supported by the pH titration of WT ChRmine in which λ_{max} is shifted by decreasing pH, possibly due to protonation of D115 and D253 (Figures S4E and S4F).

Next, to identify which carboxylate works as a primary proton acceptor in the M intermediate, we performed flash photolysis of D115N and D253N (Figure 2D). Because rhodopsins with the deprotonated Schiff bases cannot respond to light, photocycles were measured under acidic conditions (pH 4.0) to re-protonate the Schiff base (Figure 2C). Spectroscopy revealed that both mutants have similar photo-intermediates compared with WT, but only D115N shows additional accumulation of a K-like intermediate (long-lived, up to 1 s) with lower accumulation of M intermediates (Figure 2D). Indeed, M_2 intermediate decay was faster in D115N (τ_{M2} = 190 ± 40 ms) compared with WT (τ_{M2} = 1.09 ± 0.06 s) (Figure S3L), consistent with D115 operating as a primary proton acceptor. Although D253 is located closer to the Schiff base than D115, D253 strongly interacts with Y85 and Y116, which would make it difficult for D253 to receive the proton from the Schiff base. D212 of *Hs*BR similarly interacts with two tyrosine residues (Y57 and Y185) and also does not act as the proton acceptor. D115 is located further from the Schiff base but with several waters positioned in between; water rearrangements would allow the proton to transfer from the Schiff base to D115 in the M intermediate.

Ion-conducting pore within the monomer

To explore the location and shape of the ion-conducting pathway, we first analyzed the configuration of cavities within the monomer. ChRmine displays markedly larger intracellular and extracellular cavities compared with C1C2 and *Hs*BR (Figure 3A). As in C1C2, both cavities are mainly formed by TM1, TM2, TM3, and TM7 and occluded by intracellular and central constriction sites (ICS and CCS); however, multiple key differences in the pore pathways of ChRmine and C1C2 were noted. First, although computed electrostatic surface potentials for both ChRmine and C1C2 revealed electronegative pores (Figures 3B and 3C), distribution of negatively charged residues was remarkably different. In C1C2 and several other chlorophyte CCRs, five conserved glutamates (E121, E122, E129, E136, and E140 in C1C2) cooperatively create the electronegative surface potential along the pore, but four of these five residues are substituted with neutral or basic residues in ChRmine (Figures 3B–3D and S1A). Instead, ChRmine displays a distinct set of carboxylates, including E50, E70, D100, D126, E154, E158, D242, E246, and D272, to create cavities suitable for anion exclusion (Berndt and Deisseroth, 2015; Berndt et al., 2014, 2016; Figure 3D, left).

Second, ChRmine exhibits two intracellular vestibules (IV) with distinct electrostatic potentials (Figures 3A and 3B). Notably, the position of ChRmine IV1 is more similar to the IV of the CCR C1C2, and the position of ChRmine IV2 is more similar to the IV of the ACR *Gt*ACR1 (Kato et al., 2012; Kim et al., 2018; Figures 3A–3D), consistent with the fact that ChRmine is phylogenetically closer to *Gt*ACR1 than to chlorophyte CCRs, including C1C2 (Figure S1B). The corresponding electrostatic surface potentials favor a role for IV2 as a cation-conducting pore in the open state (IV1 and IV2 could further connect to create a larger

(B and C) Ion-conducting pore and conserved negatively charged residues (E121, E122, E129, E136, and E140) along the ion-conducting pathway of C1C2 (C), and corresponding residues of ChRmine (B). Pores are colored by electrostatic potential.
(D) Ion-conducting pore and pore-aligning negatively charged residues of ChRmine, C1C2, *Cr*ChR2, C1Chrimson, and positively charged residues of *Gt*ACR1. Gray mesh: ion-conducting pore.
(E) ICS (top) and CCS (bottom) of ChRmine (left) and C1C2 (right). Black dashed lines represent H-bonds.
(F) Mutations in constriction sites. Data mean ± SEM (number of cells, n = 5–9); one-way ANOVA with Dunnett's test. *p < 0.05, ***p < 0.001, and ****p < 0.0001.
(G) The superposed intracellular regions of ChRmine (red) and *Hs*BR (blue) (left) and the intracellular region of ChRmine (right). IV1 and IV2 of ChRmine: gray mesh.
(H) The overall structure of the intracellular region of *Hs*BR. The intracellular vestibules of *Hs*BR: gray mesh.
(I) Magnified views of the blue-boxed region in (A). Comparison of the overall structure (left) and key residues (right) of ECL1 between ChRmine (red), C1C2 (yellow), and *Hs*BR (blue). The extracellular cavity of ChRmine: gray mesh. ECL1 of ChRmine adopts the different conformation shown (left), whereas in *Hs*BR Y79 and R82 efficiently occlude the cavity.

intracellular cavity in the open state, as for extracellular vestibules [EV] in other ChRs; Kato et al., 2018; Takemoto et al., 2015).

Third, the ICS architecture of ChRmine and C1C2 are different. In C1C2, the ICS is mainly formed by Y109, E122, and H173 (E122 and H173 are H-bonded to each other). In ChRmine, the corresponding residues are L47, A74, and D126, respectively, which participate in the formation of the ICS, but D126 forms a more extensive H-bonding network with Q71, Q130, Y260, and a water molecule (Figure 3E). Although the mutation of Y260 does not compromise channel activity, D126 mutants show severely decreased photocurrents—suggesting that the effect of loss of a single H-bond at the ICS is minimal, in contrast to the effect of a single change at the H-bonding network hub (Figures 3F and S5).

Fourth, the size and path of the extracellular cavities differ between ChRmine and C1C2. C1C2 has two extracellular vestibules (EV1 and EV2), but ChRmine lacks the vestibule corresponding to EV1, whereas the volume of ChRmine's sole EV is expanded (due in large part to TM3 unwinding; Figure 3A). In addition, the EV2 of C1C2 is well-separated from the Schiff base and terminates at the CCS formed by S102, E129, and N297; in contrast, the EV of ChRmine extends prominently to the Schiff base region (Figure 3E), and ChRmine's three residues corresponding to the CCS of C1C2 (L40, A81, and S258) do not form a constriction. Instead, the extensive H-bonding network formed by the counterion complexes (including D115, D253, Y85, Y116, T119, and structured water molecules) occlude the pore and define the ChRmine CCS; the importance of this H-bonding network is supported by the loss-of-function electrophysiological properties of Y85F-, Y116F-, and T119V-mutant photocurrents (Figure 3 and S5).

Although ChRmine resembles *Hs*BR in some ways (primary sequence, overall arrangement of the secondary structural elements of the monomer, and quaternary structure of the trimer; Figures 1 and S1A), the size and shape of the cavities within the monomer clearly show higher similarity to those of C1C2, consistent with the cation channel functionality of ChRmine (Figure 3A). Next, we sought to understand which structural elements contribute to the formation of these large cavities that comprise much of the channel pore in ChRmine, by comparing ChRmine and *Hs*BR in more detail. At least two notable features contribute to this formation of the pore structure. First, as described earlier, both ends of TM2 are tilted outward in ChRmine; the cytoplasmic end of TM2 is particularly tilted, by about 50°, which enlarges the intracellular cavity (Figures 1F and 3G). Furthermore, numerous hydrophilic residues (including S54, E70, Q71, D126, Q130, R268, and D272) face into the pore, which together with the structural waters creates an environment suitable for water and ion conduction. In contrast, in *Hs*BR, TM2 remains straight through the end, and 6 of the 7 hydrophilic residues mentioned earlier are replaced by hydrophobic residues, which are tightly packed with no water-accessible cavity (Figures 1F, 3A, right, and 3H).

In a second major channel-enabling feature, the unwinding of TM3 and resulting long ECL1 contribute to the creation of a large extracellular cavity in ChRmine. The helical structure of extracellular TM3 is unfolded beginning at Y116, and the C-shaped structure of ECL1 protrudes to the center of the trimer interface. This contrasts with the ECL1 of *Hs*BR, which forms a β-sheet and is located at a position that half occludes the extracellular pore (Figure 3I, left). In addition to the overall position of ECL1, R82 on TM3 and Y79 on ECL1 protrude into and occlude the extracellular cavity in *Hs*BR (Figure 3I, right). However, Y79 is replaced by G109 in ChRmine, and because of the unfolding of TM3, R112 (R82 in *Hs*BR) and G109 are displaced by 4.0 and 6.0 Å, respectively, from the corresponding residues of *Hs*BR. As a result, these residues do not block the cavity in ChRmine (Figure 3I, right).

Notably, the ECL1 of C1C2 also forms a β-sheet structure similar to *Hs*BR and moderately narrows the entrance of the pore—one of the reasons that the extracellular cavity of C1C2 is smaller than that of ChRmine (Figure 3I, left). Moreover, in C1C2, whereas the residues corresponding to R82 and Y79 of *Hs*BR are similarly positioned, Y79 is replaced by V156, and R159 (R82 in *Hs*BR) adopts a conformation similar to that of R112 in ChRmine, facing toward the extracellular solvent rather than being parallel to the membrane (Figure 3I, right). The outward-facing Arg conformation observed in ChRmine and C1C2 is conserved in other channel-type rhodopsins, including *Cr*ChR2, C1Chrimson, and *Gt*ACR1, and the parallel Arg conformation observed in *Hs*BR is also conserved in other pump-type rhodopsins, such as halorhodopsins (inward Cl^- pump-type), KR2 (outward Na^+ pump-type), and schizorhodopsin (SzR) (inward H^+ pump-type) (Figure S4D; STAR Methods). The Arg in the parallel conformation narrows or blocks the extracellular cavity of the ion-translocating pathway, which would contribute to preventing large ion flux in ion-pumping rhodopsins. Notably, *Cs*R (the outward H^+-pumping rhodopsin from *C. subellipsoidea*) also has Arg (R83) in the parallel conformation in the dark state (Fudim et al., 2019), and R83Q mutation (or mutation of the adjacent Tyr, Y57K) converts protein functionality from H^+ pump to H^+ channel (Vogt et al., 2015). Moreover, computational analysis of *Hs*BR with R82Q or Y57K mutation reveals that these mutations change the conformation of R82Q or R82, respectively; most notably, R82 faces outward in the Y57K simulation (Vogt et al., 2015). These results suggest that, beyond setting overall size of the monomer cavity, the outward-facing Arg conformation in the dark state is a key structural element defining the function of ion-transporting rhodopsins. Interestingly, previous studies have reported that this Arg of some ion-pumping rhodopsins is maintained in the parallel conformation during the photocycle (Kouyama et al., 2015; Kovalev et al., 2020), but the corresponding Arg in *Hs*BR transiently changes from parallel to outward-facing to facilitate proton release to the extracellular solvent (Kühlbrandt, 2000; Nango et al., 2016). Because ChRs presumably evolved from ion-pumping rhodopsins (Inoue et al., 2015), these studies suggest that mutations accumulating near this Arg of ion-pumping rhodopsins gradually stabilized the outward-facing conformation; these rearrangements enlarged the extracellular cavity, enabling the large ion flux of ChRs.

Functional importance of trimeric assembly

Similar to *Hs*BR, ChRmine forms a trimer; here, we find that ChRmine has an unexpected additional opening at the trimer interface (Figure 4A, left). The corresponding region in *Hs*BR is hydrophobic and filled with several lipid molecules, but for

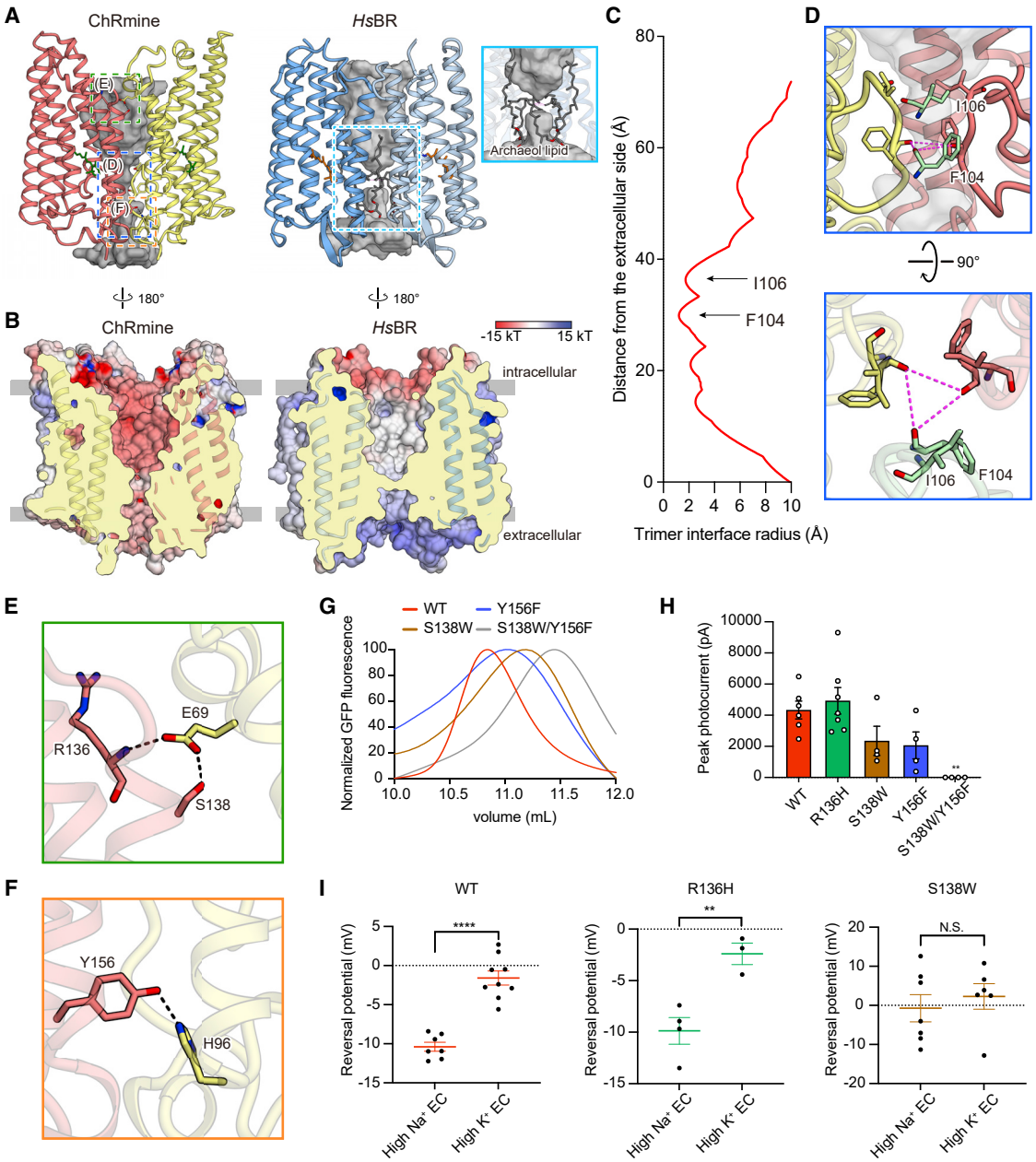

Figure 4. The functional importance of trimeric assembly

(A and B) The opening within the trimer interface in ChRmine (left) and *Hs*BR (right). Opening: gray (A). Electrostatic potential surface (B).

(C) Trimer opening radii of the ChRmine.

(D) Magnified views of the blue-boxed region from (A), the constriction formed by ECL1, from two angles.

(E and F) Magnified views of the green- and orange-boxed regions in (A), the H-bond interactions between protomers at the intracellular (E) and extracellular (F) side.

(G) FSEC traces of ChRmine WT, S138W, Y156F, and S138W/Y156F mutants.

(H) Photocurrent amplitudes for the mutants shown in (E) and (F), as well as R136H (negative control) (n = 4–7).

(I) Reversal potentials of ChRmine WT, R136H, and S138W mutants (n = 3–9). All data mean ± SEM; sample size n denotes the number of cells. One-way ANOVA with Dunnett's test (I) and unpaired t test (H), **p < 0.01 and ****p < 0.0001. N.S., not significant.

ChRmine, this region is relatively hydrophilic and negatively charged (Figures 4A, right, and 4B). The chalice-shaped opening is formed by TM2–TM4 and ECL1 of the protomer, and the narrowest region is created by ECL1; the main-chain carbonyl oxygens of F104 and I106 face toward the center of the trimer and form the central constriction (Figures 4C and 4D).

ChRmine exhibits three intermolecular H-bond interactions between adjacent protomers: S138 with E69, the main-chain

amide of R136 with E69, and Y156 with H96 (Figures 4E and 4F). To analyze the functional importance of trimeric assembly, we introduced mutations to each of these residues to destabilize the trimer. We used fluorescence-detection size exclusion chromatography (FSEC) (Kawate and Gouaux, 2006) to evaluate oligomerization and found that S138W or Y156F mutation shifts the equilibrium to favor monomeric states, and S138W/Y156F double mutation almost completely dissociates the trimer into the monomeric state (Figure 4G). Subsequent electrophysiology revealed that these single and double mutations moderately and severely decrease channel activity, respectively (Figures 4H and S5), and the S138W mutation additionally reduces cation selectivity (Figure 4I). Because S138 and Y156 are unequivocally located far from the canonical ion-conducting pathway within the monomer, and the R136H mutation (which does not affect protomer-protomer interactions) does not change channel activity or cation selectivity, these results support the importance of trimeric assembly for cation conduction and provide the initial evidence for the importance of oligomerization in ChR channel function.

Structure-guided engineering of ChRmine variants with new properties

Next, we sought to enhance the speed and spectral response of ChRmine for all-optical experiments (Figures 5A and 5B). We began with speed—noting that if it were possible, a 2- to 3-fold acceleration of ChRmine kinetics (Marshel et al., 2019) would approach the time constants of principal cells in the brain. One strategy to accelerate closing kinetics would be via mutations to the Schiff base counterion (Gunaydin et al., 2010; Rajasethupathy et al., 2015), but counterion mutations in ChRmine compromise channel function (Figure 2B).

In a separate line of investigation, we had found that other mutations predicted to alter pore electrostatic potential can also affect kinetics (Kato et al., 2018; Kim et al., 2018). However, it was unclear that these mutations along the ion-conduction pathway in dimeric ChRs would translate to the structurally divergent ChRmine, where ion conduction has distinctive properties (for example, we discovered that ChRmine exhibits high monovalent cation selectivity [excluding Ca^{2+} and Mg^{2+}, and strikingly, favoring K^+ over Na^+; Figure S6A], an unusual property of this pump-like ChR [PLCR]). Nevertheless, to test this alternate strategy, we introduced 6 mutations (Figure 5A; H33R, D92N, E154Q, E158Q, D242N, and E246Q) to the pore and tested kinetics. Among these, three (H33R, D92N, and E154Q) exhibited powerful effects; most strikingly, τ_{off} and τ_{on} of H33R were more than 2-fold faster (30 and 10 ms, respectively) than those of the WT (70 and 16 ms, respectively; Figure 5C), further validating the structure-guided design approach—previously successful for CCRs and ACRs (Deisseroth and Hegemann, 2017) – now for PLCRs.

Next, we sought to modify the spectral properties, specifically targeting red-shifted actuation to improve compatibility with blue-light-activated genetically encoded Ca^{2+} indicators (GECIs). Previous studies have shown that mutations in the retinal binding pocket (RBP) can change the spectral properties, including peak and shape of the action spectrum (Kato et al., 2015a; Oda et al., 2018; Pan et al., 2014); however, sequence identity is low (~20%) between ChRmine and structurally resolved CCRs (Marshel et al., 2019), which precluded effective homology modeling of the ChRmine RBP before the structure was solved (Figure 5B). Because tight packing of RBP residues against the retinal polyene chain and polar interactions with the retinal β-ionone ring have been reported to contribute to red-shifted spectra (Kamiya et al., 2013; Oda et al., 2018; Prigge et al., 2012), we designed seven constructs with RBP mutations (I146M, G174S, F178Y, I146M/G174S, I146M/F178Y, G174S/F178Y, and I146M/G174S/F178Y) for testing in cultured neurons (Figures S6B–S6D). Under one-photon (1P) illumination, the double mutant I146M/G174S exhibited a surprisingly large reduction in the blue shoulder and red shift (Figures 5D–5G) (with a decrease in cyan light sensitivity of 2.6× and an increase in red light sensitivity of 1.3×, compared with WT ChRmine; Figures S6E and S6F).

We designated the accelerated-kinetics variant (H33R) as hsChRmine (for high speed) and the optimal, red-shifted variant (I146M/G174S) as rsChRmine (for red-shifted) (Figures 5F and S7). Both variants showed robust expression (Figure S7A), and although many strategies for accelerating channel kinetics and shifting action spectra also reduce photocurrents (Gunaydin et al., 2010; Kato et al., 2018; Mager et al., 2018; Oda et al., 2018), both ChRmine variants exhibited peak photocurrent amplitudes similar to that of WT (Figures 5F and S7F). Consistent with its speed (Figure S7B), we observed that hsChRmine enabled high-fidelity spiking up to 40 Hz (Figures S7C and S7D; STAR Methods). Combining all three mutations (H33R/I146M/G174S) resulted in further accelerated opening (Figure S7B) and greater red shift (Figures S7E and S7F), albeit with reduced photocurrents (still >500 pA; Figure S7F); we designate this variant frChRmine (combining faster and further red-shifted performance).

Finally, we compared two-photon (2P) spectra of ChRmine variants with ChroME2 (Sridharan et al., 2021). We found that the spectral shift of rsChRmine was even greater with 2P; at 825 nm, little rsChRmine current was detected, whereas WT ChRmine at 825 nm exhibited 40% of the maximal photocurrent elicited at 1,050 nm. Furthermore, the 2P spectra of ChroME2f/2s were found to be blue-shifted relative to those of ChRmine, as with 1P stim (Figures 5G, 5H, and S7E–S7H). Together, these ChRmine variants provide major practical advantages, compared with opsins that are otherwise good candidates for all-optical investigation of intact neural circuitry.

Minimal cross talk for all-optical experiments with rsChRmine

A blue shoulder persists in the action spectra of all published ChRs; thus, the distinctive spectral properties of rsChRmine raised the prospect of minimizing the optical cross talk that is problematic for all-optical neuroscience. We characterized spike fidelity as a function of pulse width and irradiance for rs- and WT ChRmine in brain slices (Figure 5I) and cultured neurons (Figures S6G and S6H); in both settings, rsChRmine exhibited the desired properties. In particular, orange-light (580 nm) stimulation of rsChRmine reliably triggered action potentials in brain slices, whereas blue light (440 nm) did not (pulse width 1 ms; irradiance 0.3 mW/mm^2; Figures 5J and 5K). In contrast, spike fidelities

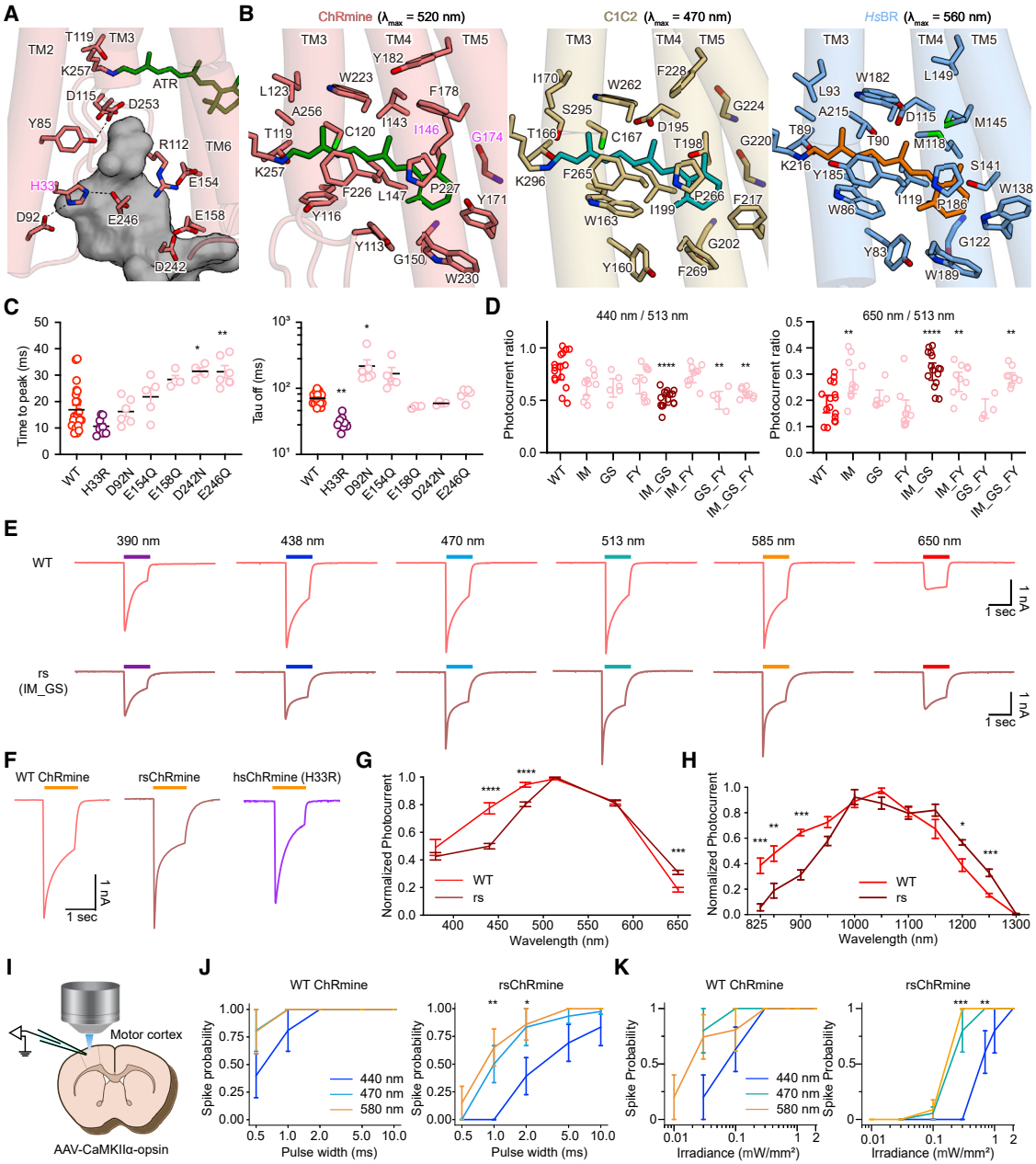

Figure 5. Structure-guided design of ChRmine variants

(A) Residues comprising the EV (dark gray surface) of ChRmine. Dashes denote H-bonds.

(B) RBPs of ChRmine (left), C1C2 (middle), and *Hs*BR (right). Key amino acids and all-*trans* retinal molecules depicted by the stick model.

(C) On (left) and off (right) kinetics (n = 4–23).

(D) Summary of photocurrent ratios (n = 4–16).

(E) Voltage-clamp traces of WT- (top) and rsChRmine- (bottom) expressing neurons stimulated by indicated light wavelengths.

(F) Example traces of opsins.

(G) Normalized action spectra of WT and rsChRmine (n = 16 for WT and 15 for rs).

(H) 2P action spectra of WT (n = 6) and rsChRmine (n = 5).

(I) Schematic of brain slice physiology.

(J) Spike probability versus pulse width in slices (5 Hz/4 s, 1 mW/mm^2, n = 5 for WT, n = 6 for rs).

(K) Spike probability versus light power in slices (at 5 Hz for 5 s, pulse width = 5 ms, n = 5 for WT, n = 6 for rs). All data mean ± SEM; sample size n denotes the number of cells. Wilcoxon rank sum test for G and Kruskal-Wallis test with Dunn's test for the rest. *p < 0.05, **p < 0.01, ***p < 0.001, and ****p < 0.0001.

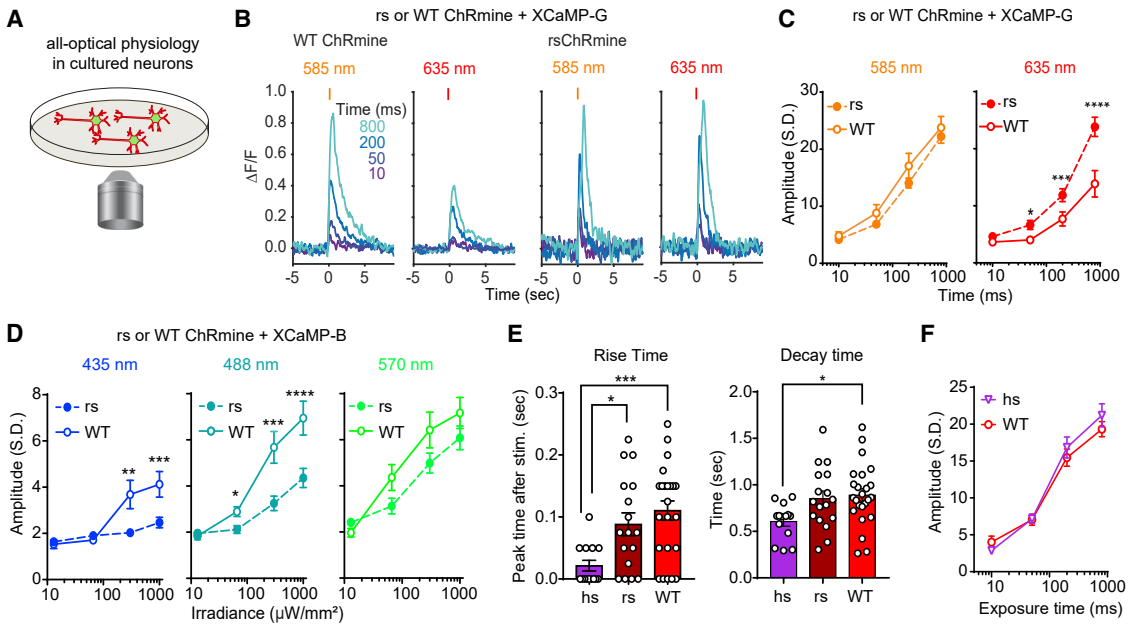

Figure 6. *In vitro* demonstration of rsChRmine application

(A) Schematic: all-optical physiology.

(B) Representative traces of XCaMP-G response to orange (585 nm) or red (635 nm) light stimulation in WT (left) or rsChRmine (right) neurons.

(C) Peak XCaMP-G responses to orange and red light (n = 14 for rs; n = 15 for WT, two-tailed Mann-Whitney U test).

(D) Peak XCaMP-B responses to blue (435 nm; left), cyan (488 nm; middle), and green (570 nm; right) light stimulation (n = 31 for rs, n = 32 for WT, two-tailed Mann-Whitney U test).

(E) Summary of rise and decay kinetics of XCaMP-G transients (n = 14 for hs; n = 17 for rs; n = 24 for WT, one-way ANOVA with Turkey's test).

(F) Peak XCaMP-G responses to 585 nm light stimulation (2.0 mW/mm^2) (n = 14 for hs and 10 for WT). All data mean ± SEM; sample size n denotes the number of cells. *p < 0.05, **p < 0.01, ***p < 0.001, and ****p < 0.0001.

under orange and blue light for WT ChRmine were similar for all pulse widths and irradiance levels. Thus, the blue shoulder reduction of rsChRmine minimized optical cross talk, assessed with the crucial readout of neuronal spiking.

To test potential utility for all-optical experiments, we characterized spectral compatibility with the green GECI, XCaMP-G (Inoue et al., 2019) in cultured neurons using 1P stimulation (Figure 6A). Indeed, rsChRmine markedly increased responses to red (635 nm) but not orange (585 nm) light (Figures 6B and 6C). Furthermore, in testing readout from the blue GECI XCaMP-B (Inoue et al., 2019) using an excitation wavelength of 385 nm, we found that rsChRmine exhibited reduced sensitivity to blue (435 nm) and cyan (488 nm) light, whereas no difference was observed for green (570 nm) light (Figure 6D), revealing that structure-guided design of rsChRmine indeed resulted in suitably optimized properties for all-optical experiments. Also, of note, we observed faster kinetics of hsChRmine-elicited XCaMP-G responses compared with those of WT ChRmine, whereas no difference in response amplitude was measured for the same light-exposure time (Figures 6E and 6F).

In vivo simultaneous activity recording and optogenetic control in mice

These results indicated that rsChRmine could be useful for exploring new kinds of simultaneous optical imaging and control *in vivo*. To explicitly test this, we first applied frame-projected independent-fiber photometry (FIP) for simultaneous recording (Kim et al., 2016) and perturbation of activity in pyramidal (Pyr) neurons of medial prefrontal cortex (mPFC) of mice (Figures 7A and 7B), coexpressing GCaMP6m and opsin to compare rsChRmine with other opsins (WT ChRmine and ChrimsonR; Klapoetke et al., 2014; Marshel et al., 2019; Figure 7C). We first measured GCaMP6m responses evoked by rsChRmine activation at 594 nm, using interleaved 2.5 μW of 470 nm imaging light to measure neural responses. In line with previous findings (Marshel et al., 2019) and our results in cultured neurons (Figures 6A–6D), 594 nm light generated markedly larger GCaMP6m response amplitudes (4-fold larger ΔF/F) that were 2× more sensitive to the irradiance level in cells expressing rsChRmine or WT ChRmine, compared with those expressing ChrimsonR (Figures 7D–7F).

To quantify the independence of optical information channels in a practical setting, we tested for incidental stimulation of the targeted cells by 470 nm blue-light pulses that are intended for GCaMP imaging, not red-shifted opsin stimulation. rsChRmine- and ChrimsonR-expressing cells exhibited little evoked change in fluorescence even up to 20 μW of 470 nm light, whereas WT ChRmine exhibited significant fluorescent changes from 3 μW (Figure 7G). Concordant with this improvement, we also detected a side effect of fluorescence ramping at the beginning of recording with 470 nm imaging light but only with WT ChRmine (Figure 7H). rsChRmine was, thus, distinctive in jointly maximizing red shift

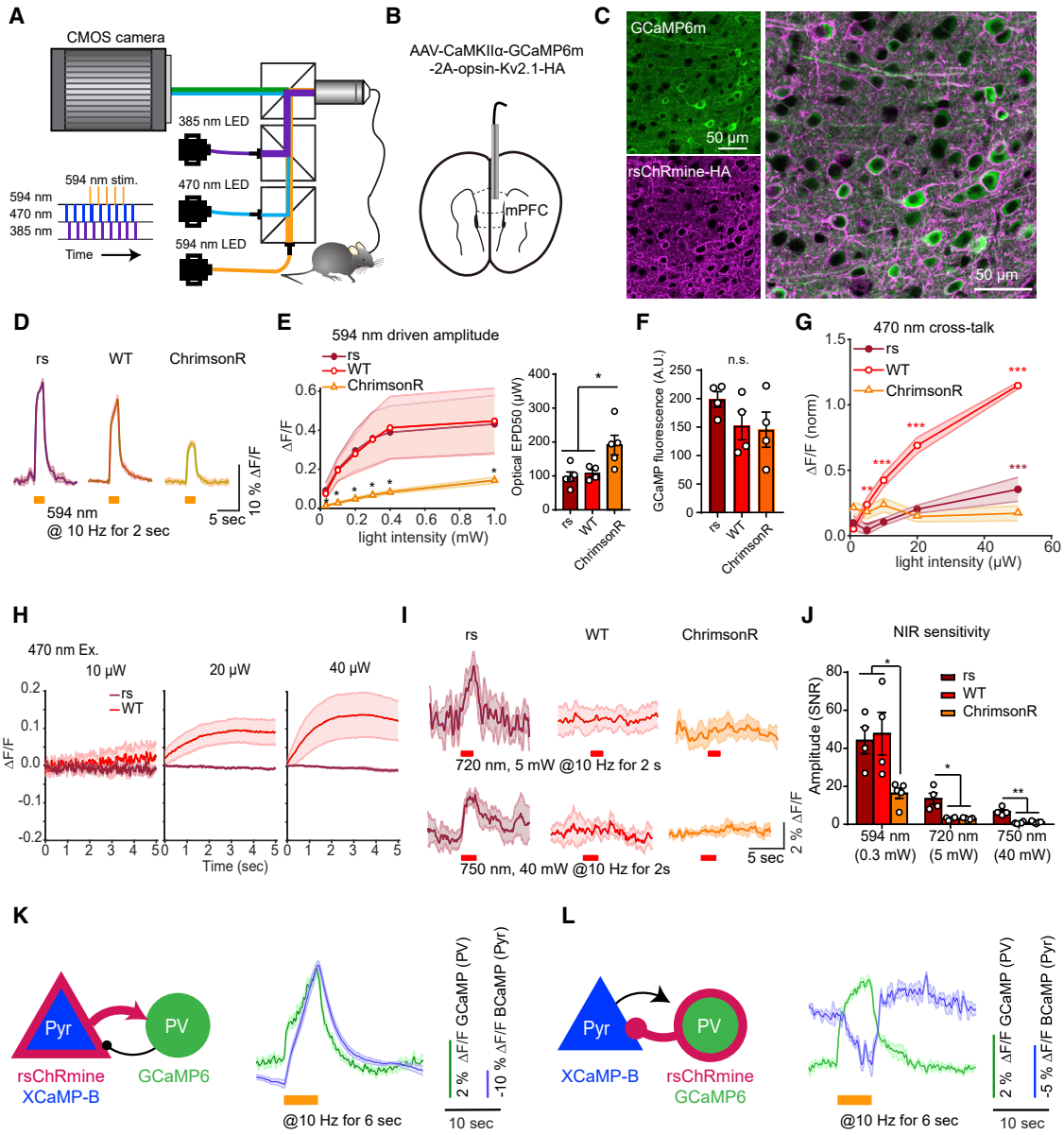

Figure 7. *In vivo* demonstration of rsChRmine application

(A) Schematic: FIP rig for simultaneous Ca^{2+} recording and optogenetic stimulation.

(B) Schematic: virus delivery and fiber placement in mPFC.

(C) Expression of GCaMP6m and rsChRmine in neurons.

(D) GCaMP6m traces in response to 594 nm stimulation in freely moving mice expressing opsins (n = 4 mice, 4 trials per mouse).

(E) Left: mean response to various light powers. Right: EPD50.

(F) Quantification of baseline GCaMP6m fluorescence in rsChRmine, WT ChRmine, and ChrimsonR-expressing mice.

(G) Mean amplitudes evoked at 470 nm normalized to the peak amplitude evoked at 594 nm stimulation for mice expressing each opsin.

(H) GCaMP6m fluorescence at the start of imaging at different 470 nm light powers.

(I) GCaMP6m traces in response to 720 (top) and 750 nm (bottom) stimulation in freely moving mice expressing opsins (n = 4 mice, 4 trials per mouse).

(J) Mean response to 594, 720, and 750 nm stimulation of the indicated opsins.

(K and L) Pyr to PV (K) and PV to Pyr (L) Ca^{2+} recordings. Left, transgene expression in mPFC PV and CaMKIIα-positive Pyr neurons. Right, representative averaged simultaneous 2-color photometry traces aligned to the start of 594 nm stimulation (green, GCaMP6; blue, XCaMP-B). All data mean (curves) ± SEM (shading around curves); sample size n denotes the number of cells unless otherwise noted. One-way ANOVA with Turkey's test. *p < 0.05, **p < 0.01, ***p < 0.001, and ****p < 0.0001.

and size of photocurrent for a given light level, prompting us to further examine sensitivity and efficacy at even longer wavelengths *in vivo*. rsChRmine-expressing neurons responded to 720 and 750 nm light stimulation, albeit at higher power than with red light, whereas neurons expressing WT ChRmine and ChrimsonR did not (Figures 7I and 7J); thus, rsChRmine represents the initial ChR reported to drive neural responses in this near-infrared (i.e., >740 nm) illumination band.

Lastly, we asked whether the shifted spectrum of rsChRmine might allow the stimulation of activity in a targeted neural population during the simultaneous recording of activity in both the stimulated and downstream neural populations, a configuration of great practical value. We, therefore, combined presynaptic rsChRmine stimulation with XCaMP-B recording, alongside postsynaptic GCaMP6f recording, by expressing both rsChRmine and XCaMP-B in Pyr neurons, and GCaMP6f in parvalbumin-expressing (PV) interneurons in mPFC (Figure 7K). 1P light was delivered at 380 nm to excite XCaMP-B, 470 nm to excite GCaMP6, and 590 nm to stimulate rsChRmine. After a burst of optical stimulation of Pyr neurons, we were able to track the temporal evolution of excitation in the stimulated Pyr population while also observing downstream activity responses in PV neurons. Conversely, when the targeting strategy was inverted (XCaMP-B to Pyr neurons and GCaMP6m/rsChRmine to PV neurons), the opposite result was obtained: upon optical stimulation of PV neurons, which gave rise to increased activity in the PV-cell population, detected activity of Pyr neurons was potently reduced (Figure 7L). The use of rsChRmine to measure such a type-to-type impulse response between cell populations in alert animals (and thus obtain a calibrated measure of the instantaneous influence of one cell type on another) is a key step toward more controlled and realistic analysis of the complexities of intact-brain dynamics.

DISCUSSION

The unusual properties of ChRmine have opened up new avenues of investigation for optogenetics in the study of cell-specific activity within biological systems (Chen et al., 2021; Marshel et al., 2019); alongside extremely large photocurrents, red-shifted actuation, and light sensitivity (Marshel et al., 2019), ChRmine exhibits virtually no Ca^{2+} conductance (Figure S6A), a valuable property in long-timescale optogenetics applications for avoiding incidental induction of Ca^{2+}-dependent plasticity. Here, we have revealed structure-function relationships underlying the properties of ChRmine, along with insights into evolution of microbial opsins. First, despite its fundamentally distinct channel-based mechanism, we find that ChRmine is surprisingly similar to the *Hs*BR pump in terms of oligomerization number (Figure 1C), overall monomeric structure (Figure 1E), and proton acceptor (Figure 2D), suggesting that ChRmine evolved from archaeal ion-pumping rhodopsins. In *Hs*BR, D85 and D96 of the DTD motif perform critical functions as relays for the pumping transfer of a single proton from the intracellular to extracellular side, in response to the absorbed photon. In ChRmine, these two Asps are conserved (D115 and D126) but not for H^+-pumping relay purposes; rather, they form the two constriction sites (ICS and CCS) of the passive ion-conducting pore within the monomer.

Thus, these two residues continue to play critical roles in gating the channel, rather than as relay points for H^+ transport. In *Hs*BR, D85 receives a H^+ from the protonated Schiff base and releases it to the extracellular bulk solvent; D96 receives a H^+ from the intracellular bulk solvent and provides it to the deprotonated Schiff base. These proton movements generate net flow of protons from the intracellular to extracellular side; these two functionally important residues, together with T89, are called the DTD motif. In *Gt*CCR2 (a ChRmine homolog), D85 and D96 are conserved (D87/D98, respectively), but the apparent H^+ translocation pathway is different; *Gt*CCR2 does not show outward proton-pumping activity (Sineshchekov et al., 2017), and the H^+ is shuttled back and forth between the Schiff base and D87. Although deprotonation and re-protonation of D98 are assumed to occur, with deprotonation necessary for the channel gating, D98 never provides the H^+ to the deprotonated Schiff base (Sineshchekov et al., 2017). If some ChRs retain residual pumping activity, D85 homologs presumably could release a H^+ to the extracellular bulk solvent after receiving a H^+ from the Schiff base, but in contrast to the H^+ acceptor, it remains elusive which residue works as a H^+ donor to the deprotonated Schiff base. D96 in *Hs*BR is also conserved in ChRmine (D126) but is exposed to intracellular bulk solvent in our structure, and the calculated pKa of D126 is as low as 6.27. D126 may, thus, be unlikely to work as the sole H^+ donor (Figure 3G) although is possible that the deprotonated Schiff base directly receives a H^+ from water molecules. Future studies will be needed to reveal the molecular nature of the H^+ donor and to understand how H^+ translocation is involved in channel gating of ChRmine.

Despite similarities to *Hs*BR, ChRmine exhibits several atypical properties in its high-resolution structure, including its long twisted ECL1. ECL1 not only significantly distorts the architecture around the Schiff base but also enlarges the extracellular cavity within the monomer. Interestingly, the length and sequence of ECL1 are not highly conserved in this subfamily, and cation selectivity has been reported to be different between PLCRs that we would predict to have long versus short ECL1 domains (Sineshchekov et al., 2020). Furthermore, we report that ChRmine (with its long ECL1) is remarkably selective for monovalent cations (especially K^+; Figure S6A), whereas *Hc*KCR1 and *Hc*KCR2 (recently discovered members of the same pump-like subfamily as ChRmine, with shorter ECL1 motifs) are reported to similarly exclude divalent cations and exhibit further selectivity for K^+ over Na^+ (Govorunova et al., 2021). Multiple molecular features within ECL1 may be relevant (for example, the conserved Arg residue [R112 in ChRmine] on ECL1 is replaced by Trp in *Hc*KCR1 and *Hc*KCR2), and ECL1 could be explored for roles in cation conduction and selectivity. Indeed, given the knowledge reported here regarding ChRmine's unusual structural and electrophysiological properties (especially, the distinctive ECL1 feature [Figures S1A and S4B] and high monovalent cation selectivity shared by ChRmine's close relatives but not seen in other rhodopsins [Govorunova et al., 2021; Shigemura et al., 2019; Figure S6A]), an updated inclusive name for this growing family of pump-like channelrhodopsins would be PLCRs (Figure S1A and S1B); these do not specifically resemble bacteriorhodopsin

more than the other pumps, nor—as we now know—do they generally conduct all cations).

To deepen understanding, additional studies (including structural determination of intermediate states in ChRmine and other PLCRs, such as *Hc*KCR1 and *Hc*KCR2) will be important (STAR Methods). Indeed, our current structural information of ChRmine has already provided a framework for further development of ChRmine-based optogenetic tools: hs, rs, and frChRmine (Figures 5–7). It was a surprise to see the blue shoulder reduction, which had been extraordinarily difficult to address despite more than 15 years of focused effort across many laboratories (Deisseroth and Hegemann, 2017). In the future, the structure of rs or frChRmine may therefore turn out to be of further value in elucidating the mechanism of this effect, and in porting these properties to other microbial opsins. Other design goals may include combining the key properties of rs, hs, and frChRmine with other ideas that have arisen in the course of opsin engineering (Deisseroth, 2021). For example, we previously found it productive to combine the mutations that enabled chloride flux (via conversion from cation-to-anion selectivity) with the mutations that gave rise to greatly increased light sensitivity (via slowed kinetics), resulting in a single chloride-conducting step function ChR exhibiting bistable inhibitory currents (Berndt et al., 2016). The high-resolution ChRmine structure and the new variants described here may point the way to such integration.

Before this study, published structures of ChRs were experimentally determined only using crystallography. However, we find that the combination of antibody and single-particle cryo-EM techniques (Wu et al., 2012) is powerful enough to determine the high-resolution structure of small proteins, such as ChRmine, thus representing a promising strategy for structural analysis of microbial rhodopsins alongside X-ray crystallography. The two technologies, as well as structure prediction methods, may complement each other and thus expedite structural biology of microbial rhodopsins, and the resulting information will lead to both further development of optogenetics and basic mechanistic understanding of these remarkable photoreceptor proteins.

Further structural work of value will include molecular dynamics simulations and structures of the intermediate states. Investigating the cooperativity/allostery properties linking different monomers within the trimer may not only help tune the light-response properties of optogenetic tools but also could further illustrate the basic science of ChR origins, including the conversion from trimer to dimer assembly logic during the evolutionary separation of non-PLCRs from presumably pump-like ancestors. Recent discoveries and applications using optogenetics may be extended with these ChRmine variants to a broad range of opportunities, capitalizing upon the high photocurrents and light sensitivity of the parent opsin and improved properties of the variants (Bansal et al., 2021; Sahel et al., 2021). Structural insight and structure-guided design of microbial opsins continue to open up pathways for discovery and understanding, extending now to the third of the three major known ChR types: CCRs (Kato et al., 2012), ACRs (Kim et al., 2018; Kato et al., 2018), and PLCRs.

Limitations of the study

This study provides a structural framework for understanding the ion conduction and channel gating properties of ChRs in general and ChRmine specifically, but several important questions remain. First, our structural and electrophysiological analyses reveal the functional importance of trimeric assembly in ChRmine, but the reason oligomerization is important for channel function remains elusive. One possibility is that intermolecular interactions, for example, between TM2 of one protomer and TM4 of the next protomer, are important to enlarge the cavities within the monomer by stabilizing the outward tilt of TM2 and facilitate ion conduction (Figures 1C and 3G); another possibility is that channel gating (opening and closing) is coupled between monomers in the trimer (i.e., cooperativity of gating). Finally, the central opening within the trimer interface might be directly involved in ion conduction (Figure 4A).

During preparation of this manuscript, the deep-learning-based protein-structure prediction program AlphaFold2 was released (Jumper et al., 2021); therefore, we generated the predicted structures (hereafter referred to as AF2 models) of ChRmine for comparison with our cryo-EM structure (Figures S1C–S1F). Aspects of the overall structure of ChRmine could be predicted and the AF2 models could be partially superposed onto the cryo-EM structure (Figure S1D). However, striking differences were observed in N- and C-terminal regions, the cytoplasmic sides of TM5–7, and ICL1 and ECL1 (Figure S1D). In particular, the predicted local distance difference test (pLDDT) score (Mariani et al., 2013; Tunyasuvunakool et al., 2021) of most ECL1 was so low that no AF2 models could accurately predict the structure of ECL1 and the resulting pore within the trimer interface (Figures S1C–S1E). In addition, although D115 exhibited an exceptionally high pLDDT score (>90) in ECL1, its unique conformation was not reproduced by AF2 models; the models incorrectly predict the canonical conformation for D115, an outcome readily explicable due to biasing by the previously solved microbial rhodopsin structures deposited to the PDB database (Figures S4C and S1F). These results indicate that AlphaFold2 is an outstanding program for structure prediction, but an experimentally determined structure was clearly needed to discover and interpret the critical novel features of ChRmine, including the unique architecture of the Schiff base. A general cautionary note for the field is that when using the AF2 models, it would be important to carefully interpret the structures even if the pLDDT score is high.

Our cryo-EM structure represents a snapshot of the dark state, and initial structural changes of ChRmine can be inferred (Figures S2Q and S2R; STAR Methods), but subsequent studies are needed to understand the conformational changes driven by light activation. Moreover, our current structural information allowed us to potently modify the kinetics and action spectrum of ChRmine, but other properties, including ion selectivity and light sensitivity, remained to be explored and serve as important targets for next-generation work, all enabled by this initial high-resolution structure of ChRmine (a starting point for better understanding of the form and function of this natural protein and optogenetic tool).

STAR★METHODS

Detailed methods are provided in the online version of this paper and include the following:

- KEY RESOURCES TABLE
- RESOURCE AVAILABILITY
  - Lead contact
  - Material availability
  - Data and code availability
- EXPERIMENTAL MODEL AND SUBJECT DETAILS
  - Insect cell culture
  - Animals used for antibody generation
  - Primary neuron and HEK293 cell culture
  - Animals used for surgeries
- METHOD DETAILS
  - Cloning, Protein Expression, and Purification
  - Antibody generation
  - Formation and purification of the ChRmine-Fab02 complex
  - Cryo-EM data acquisition and image processing
  - Model building and refinement
  - Pore analysis
  - Analysis of F_o-F_c difference densities
  - Analysis of conserved Arg conformations among microbial rhodopsins
  - High performance liquid chromatography (HPLC) analysis of retinal isomers
  - Preparation of lipid-reconstituted ChRmine for high-speed AFM imaging
  - High-speed AFM measurements
  - Measurement of UV absorption spectra
  - Laser flash photolysis
  - Molecular cloning
  - Primary cell transfection
  - Virus production
  - *In vitro* electrophysiology in HEK293 cells
  - Ion selectivity testing in HEK293 cells
  - *In vitro* one-photon electrophysiology in cultured hippocampal neurons
  - *In vitro* two-photon electrophysiology
  - Stereotactic surgeries
  - Acute slice electrophysiology
  - *In vitro* characterization using all-optical physiology methods
  - FIP setup and analysis
  - Histology and Confocal Microscopy
- QUANTIFICATION AND STATISTICAL ANALYSIS

SUPPLEMENTAL INFORMATION

Supplemental information can be found online at https://doi.org/10.1016/j.cell.2022.01.007.

ACKNOWLEDGMENTS

We thank R. Danev, M. Kikkawa, K. Hasegawa (Univ. of Tokyo), A. Kotecha (Thermo Fisher), A. Maturana (Nagoya Univ.), and C. Delacruz (Stanford Univ.) for technical and administrative support. This work was supported by the MRC, as part of UKRI (MC_UP_A025_1012 to K.Y.), Osamu Hayaishi Memorial Scholarship for Study Abroad (M.I.), the Nakajima Foundation (H.E.K.), the Yamada Science Foundation (H.E.K.), the Nakatani Foundation (H.E.K.), the UTEC-UTokyo FSI Research Grant Program (H.E.K.), AMED/BINDS (JP18am0101079 [support no. 2165] and JP20am0101115 [support no. 2841]), AMED (JP21wm0525018 to H.E.K.), JSPS KAKENHI (JP20K21383 and JP21H01875 to K.I. and 21H05142 to H.E.K.), JST PRESTO (JPMJPR1888 to T.N. and JPMJPR1782 to H.E.K.), JST FOREST (JPMJFR204S to H.E.K.), JST CREST (JPMJCR21P3 to H.E.K.), the NSF NeuroNex program (K.D.), the NOMIS Foundation (K.D.), the Else Kroner-Fresenius Foundation (K.D.), the Gatsby Foundation (K.D.), and a grant for ChR structure determination from NIMH (R01MH075957 to K.D.).

AUTHOR CONTRIBUTIONS

K.E.K. and M.F. produced the proteins and prepared cryo-EM grids. T.K. obtained cryo-EM images, using the platform developed by O.N. T.K. and T.E.M. processed cryo-EM data. K.E.K., K.Y., and H.E.K. built the model and refined the structure. Y.S.K. and P.Y.W. performed electrophysiology with the support of C.R. and S.Q. K.E.K., M.F., and H.E.K. and Y.S.K., P.Y.W., C.R. and K.D. designed ChRmine variants. E.T., J.M.P., and R.O.D. provided input on structural considerations. E.F.X.B. and Y.S.K. performed crystallography at an early stage. E.F.X.B. generated the predicted AF2 structures. T.B. and M.I. provided input on electrophysiology. K.E.K. measured UV-vis absorption spectra. M.K. and K.I. performed flash photolysis. T.N. performed HPLC analysis. M.S. performed HS-AFM experiments. T.U. and K.L. produced the Fab02 using the platform developed by S.I. and N.N. M.I. performed all-optical physiology with support from C.R., M.L., and S.Q. K.E.K., Y.S.K., M.I., P.Y.W., K.D., and H.E.K. wrote the manuscript with input from all authors. K.D. and H.E.K. supervised all aspects of the research.

DECLARATION OF INTERESTS

The ChRmine antibody (Fab02) and ChRmine variants are described in the pending patent application material; these tools and all methods, protocols, clones, and sequences are freely available to nonprofit institutions and investigators. K.D. is a member of the *Cell* advisory board.

Received: October 31, 2021
Revised: December 13, 2021
Accepted: January 11, 2022
Published: February 2, 2022

REFERENCES

Baker, N.A., Sept, D., Joseph, S., Holst, M.J., and McCammon, J.A. (2001). Electrostatics of nanosystems: application to microtubules and the ribosome. Proc Natl Acad Sci USA *98*, 10037–10041.

Bansal, H., Gupta, N., and Roy, S. (2021). Theoretical analysis of optogenetic spiking with ChRmine, bReaChES and CsChrimson-expressing neurons for retinal prostheses. J. Neural Eng. *18*, 0460b8.

Bayburt, T.H., Grinkova, Y.V., and Sligar, S.G. (2002). Self-assembly of discoidal phospholipid bilayer nanoparticles with membrane scaffold proteins. Nano Lett. *2*, 853–856.

Berndt, A., and Deisseroth, K. (2015). OPTOGENETICS. Expanding the optogenetics toolkit. Science *349*, 590–591.

Berndt, A., Lee, S.Y., Ramakrishnan, C., and Deisseroth, K. (2014). Structure-guided transformation of Channelrhodopsin into a light-activated chloride channel. Science *344*, 420–424.

Berndt, A., Lee, S.Y., Wietek, J., Ramakrishnan, C., Steinberg, E.E., Rashid, A.J., Kim, H., Park, S., Santoro, A., Frankland, P.W., et al. (2016). Structural foundations of optogenetics: determinants of channelrhodopsin ion selectivity. Proc. Natl. Acad. Sci. USA *113*, 822–829.

Braiman, M.S., Mogi, T., Marti, T., Stern, L.J., Khorana, H.G., and Rothschild, K.J. (1988). Vibrational spectroscopy of bacteriorhodopsin mutants: light-

driven proton transport involves protonation changes of aspartic acid residues 85, 96, and 212. Biochemistry *27*, 8516–8520.

Chan, S.K., Kitajima-Ihara, T., Fujii, R., Gotoh, T., Murakami, M., Ihara, K., and Kouyama, T. (2014). Crystal structure of Cruxrhodopsin-3 from Haloarcula vallismortis. PLoS One *9*, e108362.

Chen, R., Gore, F., Nguyen, Q.-A., Ramakrishnan, C., Patel, S., Kim, S.H., Raffiee, M., Kim, Y.S., Hsueh, B., Krook-Magnusson, E., et al. (2021). Deep brain optogenetics without intracranial surgery. Nat. Biotechnol. *39*, 161–164.

Chen, V.B., Arendall, W.B., Headd, J.J., Keedy, D.A., Immormino, R.M., Kapral, G.J., Murray, L.W., Richardson, J.S., and Richardson, D.C. (2010). MolProbity: all-atom structure validation for macromolecular crystallography. Acta Crystallogr. D Biol. Crystallogr. *66*, 12–21.

Deisseroth, K. (2015). Optogenetics: 10 years of microbial opsins in neuroscience. Nat. Neurosci. *18*, 1213–1225.

Deisseroth, K. (2021). From microbial membrane proteins to the mysteries of emotion. Cell *184*, 5279–5285.

Deisseroth, K., and Hegemann, P. (2017). The form and function of channelrhodopsin. Science *357*, eaan5544.

Denisov, I.G., and Sligar, S.G. (2016). Nanodiscs for structural and functional studies of membrane proteins. Nat. Struct. Mol. Biol. *23*, 481–486.

Dolinsky, T.J., Nielsen, J.E., McCammon, J.A., and Baker, N.A. (2004). PDB2PQR: an automated pipeline for the setup of Poisson-Boltzmann electrostatics calculations. Nucleic Acids Res. *32*, W665–W667.

Emsley, P., and Cowtan, K. (2004). Coot : model-building tools for molecular graphics. Acta Crystallogr. D Biol. Crystallogr. *60*, 2126–2132.

Enami, N., Yoshimura, K., Murakami, M., Okumura, H., Ihara, K., and Kouyama, T. (2006). Crystal structures of Archaerhodopsin-1 and -2: common structural motif in archaeal light-driven proton pumps. J. Mol. Biol. *358*, 675–685.

Ernst, O.P., Lodowski, D.T., Elstner, M., Hegemann, P., Brown, L.S., and Kandori, H. (2014). Microbial and animal rhodopsins: structures, functions, and molecular mechanisms. Chem. Rev. *114*, 126–163.

Fenno, L.E., Ramakrishnan, C., Kim, Y.S., Evans, K.E., Lo, M., Vesuna, S., Inoue, M., Cheung, K.Y.M., Yuen, E., Pichamoorthy, N., et al. (2020). Comprehensive dual- and triple-feature intersectional single-vector delivery of diverse functional payloads to cells of behaving mammals. Neuron *107*, 836–853.e11.

Fudim, R., Szczepek, M., Vierock, J., Vogt, A., Schmidt, A., Kleinau, G., Fischer, P., Bartl, F., Scheerer, P., and Hegemann, P. (2019). Design of a light-gated proton channel based on the crystal structure of Coccomyxa rhodopsin. Sci. Signal. *12*, eaav4203.

Gerwert, K., Souvignier, G., and Hess, B. (1990). Simultaneous monitoring of light-induced changes in protein side-group protonation, chromophore isomerization, and backbone motion of bacteriorhodopsin by time-resolved Fourier-transform infrared spectroscopy. Proc. Natl. Acad. Sci. USA *87*, 9774–9778.

Goddard, T.D., Huang, C.C., Meng, E.C., Pettersen, E.F., Couch, G.S., Morris, J.H., and Ferrin, T.E. (2018). UCSF ChimeraX: meeting modern challenges in visualization and analysis. Protein Sci. *27*, 14–25.

Gordeliy, V.I., Labahn, J., Moukhametzianov, R., Efremov, R., Granzin, J., Schlesinger, R., Büldt, G., Savopol, T., Scheidig, A.J., Klare, J.P., et al. (2002). Molecular basis of transmembrane signalling by sensory rhodopsin II–transducer complex. Nature *419*, 484–487.

Govorunova, E.G., Gou, Y., Sineshchekov, O.A., Li, H., Wang, Y., Brown, L.S., Xue, M., and Spudich, J.L. (2021). Kalium rhodopsins: natural light-gated potassium channels. bioRxiv, 2021.09.17.460684.

Govorunova, E.G., Sineshchekov, O.A., and Spudich, J.L. (2016). Structurally distinct cation channelrhodopsins from cryptophyte algae. Biophys. J. *110*, 2302–2304.

Gunaydin, L.A., Yizhar, O., Berndt, A., Sohal, V.S., Deisseroth, K., and Hegemann, P. (2010). Ultrafast optogenetic control. Nat. Neurosci. *13*, 387–392.

Hasegawa, N., Jonotsuka, H., Miki, K., and Takeda, K. (2018). X-ray structure analysis of bacteriorhodopsin at 1.3 Å resolution. Sci. Rep. *8*, 13123.

Higuchi, A., Shihoya, W., Konno, M., Ikuta, T., Kandori, H., Inoue, K., and Nureki, O. (2021). Crystal structure of schizorhodopsin reveals mechanism of inward proton pumping. Proc. Natl. Acad. Sci. USA *118*, e2016328118.

Inoue, K., Ono, H., Abe-Yoshizumi, R., Yoshizawa, S., Ito, H., Kogure, K., and Kandori, H. (2013). A light-driven sodium ion pump in marine bacteria. Nat. Commun. *4*, 1678.

Inoue, K., Tsukamoto, T., Shimono, K., Suzuki, Y., Miyauchi, S., Hayashi, S., Kandori, H., and Sudo, Y. (2015). Converting a light-driven proton pump into a light-gated proton channel. J. Am. Chem. Soc. *137*, 3291–3299.

Inoue, M., Takeuchi, A., Manita, S., Horigane, S.I., Sakamoto, M., Kawakami, R., Yamaguchi, K., Otomo, K., Yokoyama, H., Kim, R., et al. (2019). Rational engineering of XCaMPs, a multicolor GECI suite for *in vivo* imaging of complex brain circuit dynamics. Cell *177*, 1346–1360.e24.

Jaenecke, F., Nakada-Nakura, Y., Nagarathinam, K., Ogasawara, S., Liu, K., Hotta, Y., Iwata, S., Nomura, N., and Tanabe, M. (2018). Generation of conformation-specific antibody fragments for crystallization of the multidrug resistance transporter MdfA. Methods Mol. Biol. *1700*, 97–109.

Jumper, J., Evans, R., Pritzel, A., Green, T., Figurnov, M., Ronneberger, O., Tunyasuvunakool, K., Bates, R., Žídek, A., Potapenko, A., et al. (2021). Highly accurate protein structure prediction with AlphaFold. Nature *596*, 583–589.

Kamiya, M., Kato, H.E., Ishitani, R., Nureki, O., and Hayashi, S. (2013). Structural and spectral characterizations of C1C2 channelrhodopsin and its mutants by molecular simulations. Chem. Phys. Lett. *556*, 266–271.

Kandori, H. (2020). Biophysics of rhodopsins and optogenetics. Biophys. Rev. *12*, 355–361.

Kato, H.E. (2021). Structure-function relationship of channelrhodopsins. Adv. Exp. Med. Biol. *1293*, 35–53.

Kato, H.E., Inoue, K., Abe-Yoshizumi, R., Kato, Y., Ono, H., Konno, M., Hososhima, S., Ishizuka, T., Hoque, M.R., Kunitomo, H., et al. (2015b). Structural basis for Na+ transport mechanism by a light-driven Na+ pump. Nature *521*, 48–53.

Kato, H.E., Kamiya, M., Sugo, S., Ito, J., Taniguchi, R., Orito, A., Hirata, K., Inutsuka, A., Yamanaka, A., Maturana, A.D., et al. (2015a). Atomistic design of microbial opsin-based blue-shifted optogenetics tools. Nat. Commun. *6*, 7177.

Kato, H.E., Kim, Y.S., Paggi, J.M., Evans, K.E., Allen, W.E., Richardson, C., Inoue, K., Ito, S., Ramakrishnan, C., Fenno, L.E., et al. (2018). Structural mechanisms of selectivity and gating in anion channelrhodopsins. Nature *561*, 349–354.

Kato, H.E., Zhang, F., Yizhar, O., Ramakrishnan, C., Nishizawa, T., Hirata, K., Ito, J., Aita, Y., Tsukazaki, T., Hayashi, S., et al. (2012). Crystal structure of the channelrhodopsin light-gated cation channel. Nature *482*, 369–374.

Kawate, T., and Gouaux, E. (2006). Fluorescence-detection size-exclusion chromatography for Precrystallization screening of integral membrane proteins. Structure *14*, 673–681.

Kim, C.K., Yang, S.J., Pichamoorthy, N., Young, N.P., Kauvar, I., Jennings, J.H., Lerner, T.N., Berndt, A., Lee, S.Y., Ramakrishnan, C., et al. (2016). Simultaneous fast measurement of circuit dynamics at multiple sites across the mammalian brain. Nat. Methods *13*, 325–328.

Kim, Y.S., Kato, H.E., Yamashita, K., Ito, S., Inoue, K., Ramakrishnan, C., Fenno, L.E., Evans, K.E., Paggi, J.M., Dror, R.O., et al. (2018). Crystal structure of the natural anion-conducting channelrhodopsin *Gt*ACR1. Nature *561*, 343–348.

Kishi, K.E., Kim, Y.S., Fukuda, M., Kusakizako, T., Thadhani, E., Byrne, E.F.X., Paggi, J.M., Ramakrishnan, C., Matsui, T.E., Yamashita, K., et al. (2021). Structural basis for channel conduction in the pump-like channelrhodopsin ChRmine. bioRxiv, bioRxiv:2021.08.15.456392.

Klapoetke, N.C., Murata, Y., Kim, S.S., Pulver, S.R., Birdsey-Benson, A., Cho, Y.K., Morimoto, T.K., Chuong, A.S., Carpenter, E.J., Tian, Z., et al. (2014). Independent optical excitation of distinct neural populations. Nat. Methods *11*, 338–346.

Kolbe, M., Besir, H., Essen, L.-O., and Oesterhelt, D. (2000). Structure of the light-driven chloride pump halorhodopsin at 1.8 Å resolution. Science *288*, 1390–1396.

Kouyama, T., Kanada, S., Takeguchi, Y., Narusawa, A., Murakami, M., and Ihara, K. (2010). Crystal structure of the light-driven chloride pump halorhodopsin from Natronomonas pharaonis. J. Mol. Biol. *396*, 564–579.

Kouyama, T., Kawaguchi, H., Nakanishi, T., Kubo, H., and Murakami, M. (2015). Crystal structures of the L1, L2, N, and O States of *pharaonis* Halorhodopsin. Biophys. J. *108*, 2680–2690.

Kovalev, K., Astashkin, R., Gushchin, I., Orekhov, P., Volkov, D., Zinovev, E., Marin, E., Rulev, M., Alekseev, A., Royant, A., et al. (2020). Molecular mechanism of light-driven sodium pumping. Nat. Commun. *11*, 2137.

Kühlbrandt, W. (2000). Bacteriorhodopsin—the movie. Nature *406*, 569–570.

Kumar, S., Stecher, G., and Tamura, K. (2016). MEGA7: Molecular Evolutionary Genetics Analysis Version 7.0 for Bigger Datasets. Mol. Biol. Evol. *33*, 1870–1874.

Kurihara, M., and Sudo, Y. (2015). Microbial rhodopsins: wide distribution, rich diversity and great potential. Biophys. Physicobiol. *12*, 121–129.

Lórenz-Fonfría, V.A., Resler, T., Krause, N., Nack, M., Gossing, M., Fischer von Mollard, G., Bamann, C., Bamberg, E., Schlesinger, R., and Heberle, J. (2013). Transient protonation changes in channelrhodopsin-2 and their relevance to channel gating. Proc. Natl. Acad. Sci. USA *110*, E1273–E1281.

Luecke, H., Schobert, B., Stagno, J., Imasheva, E.S., Wang, J.M., Balashov, S.P., and Lanyi, J.K. (2008). Crystallographic structure of xanthorhodopsin, the light-driven proton pump with a dual chromophore. Proc. Natl. Acad. Sci. USA *105*, 16561–16565.

Mager, T., Lopez de la Morena, D., Senn, V., Schlotte, J., D Errico, A., Feldbauer, K., Wrobel, C., Jung, S., Bodensiek, K., Rankovic, V., et al. (2018). High frequency neural spiking and auditory signaling by ultrafast red-shifted optogenetics. Nat. Commun. *9*, 1750.

Mariani, V., Biasini, M., Barbato, A., and Schwede, T. (2013). lDDT: a local superposition-free score for comparing protein structures and models using distance difference tests. Bioinformatics *29*, 2722–2728.

Marshel, J.H., Kim, Y.S., Machado, T.A., Quirin, S., Benson, B., Kadmon, J., Raja, C., Chibukhchyan, A., Ramakrishnan, C., Inoue, M., et al. (2019). Cortical layer-specific critical dynamics triggering perception. Science *365*, eaaw5202.

Mastronarde, D.N. (2005). Automated electron microscope tomography using robust prediction of specimen movements. J. Struct. Biol. *152*, 36–51.

Morizumi, T., Ou, W.-L., Van Eps, N., Inoue, K., Kandori, H., Brown, L.S., and Ernst, O.P. (2019). X-ray crystallographic structure and oligomerization of Gloeobacter rhodopsin. Sci. Rep. *9*, 11283.

Murshudov, G.N., Skubák, P., Lebedev, A.A., Pannu, N.S., Steiner, R.A., Nicholls, R.A., Winn, M.D., Long, F., and Vagin, A.A. (2011). REFMAC 5 for the refinement of macromolecular crystal structures. Acta Crystallogr. D Biol. Crystallogr. *67*, 355–367.

Nagel, G., Ollig, D., Fuhrmann, M., Kateriya, S., Musti, A.M., Bamberg, E., and Hegemann, P. (2002). Channelrhodopsin-1: a light-gated proton channel in green algae. Science *296*, 2395–2398.

Nagel, G., Szellas, T., Huhn, W., Kateriya, S., Adeishvili, N., Berthold, P., Ollig, D., Hegemann, P., and Bamberg, E. (2003). Channelrhodopsin-2, a directly light-gated cation-selective membrane channel. Proc. Natl. Acad. Sci. USA *100*, 13940–13945.

Nango, E., Royant, A., Kubo, M., Nakane, T., Wickstrand, C., Kimura, T., Tanaka, T., Tono, K., Song, C., Tanaka, R., et al. (2016). A three-dimensional movie of structural changes in bacteriorhodopsin. Science *354*, 1552–1557.

Oda, K., Nomura, T., Nakane, T., Yamashita, K., Inoue, K., Ito, S., Vierock, J., Hirata, K., Maturana, A.D., Katayama, K., et al. (2021). Time-resolved serial femtosecond crystallography reveals early structural changes in channelrhodopsin. Elife *10*, e62389.

Oda, K., Vierock, J., Oishi, S., Rodriguez-Rozada, S., Taniguchi, R., Yamashita, K., Wiegert, J.S., Nishizawa, T., Hegemann, P., and Nureki, O. (2018). Crystal structure of the red light-activated channelrhodopsin Chrimson. Nat. Commun. *9*, 3949.

Oppermann, J., Fischer, P., Silapetere, A., Liepe, B., Rodriguez-Rozada, S., Flores-Uribe, J., Peter, E., Keidel, A., Vierock, J., Kaufmann, J., et al. (2019). MerMAIDs: a family of metagenomically discovered marine anion-conducting and intensely desensitizing channelrhodopsins. Nat. Commun. *10*, 3315.

Pan, Z.-H., Ganjawala, T.H., Lu, Q., Ivanova, E., and Zhang, Z. (2014). ChR2 Mutants at L132 and T159 with improved operational light sensitivity for vision restoration. PLoS One *9*, e98924.

Pebay-Peyroula, E., Rummel, G., Rosenbusch, J.P., and Landau, E.M. (1997). X-ray structure of bacteriorhodopsin at 2.5 angstroms from microcrystals grown in lipidic cubic phases. Science *277*, 1676–1681.

Pei, J., Kim, B.H., and Grishin, N.V. (2008). PROMALS3D: a tool for multiple protein sequence and structure alignments. Nucleic Acids Res. *36*, 2295–2300.

Pettersen, E.F., Goddard, T.D., Huang, C.C., Couch, G.S., Greenblatt, D.M., Meng, E.C., and Ferrin, T.E. (2004). UCSF Chimera?A visualization system for exploratory research and analysis. J. Comput. Chem. *25*, 1605–1612.

Prigge, M., Schneider, F., Tsunoda, S.P., Shilyansky, C., Wietek, J., Deisseroth, K., and Hegemann, P. (2012). Color-tuned channelrhodopsins for multiwavelength optogenetics. J. Biol. Chem. *287*, 31804–31812.

Rajasethupathy, P., Sankaran, S., Marshel, J.H., Kim, C.K., Ferenczi, E., Lee, S.Y., Berndt, A., Ramakrishnan, C., Jaffe, A., Lo, M., et al. (2015). Projections from neocortex mediate top-down control of memory retrieval. Nature *526*, 653–659.

Ramlaul, K., Palmer, C.M., Nakane, T., and Aylett, C.H.S. (2020). Mitigating local over-fitting during single particle reconstruction with SIDESPLITTER. J. Struct. Biol. *211*, 107545.

Ran, T., Ozorowski, G., Gao, Y., Sineshchekov, O.A., Wang, W., Spudich, J.L., and Luecke, H. (2013). Cross-protomer interaction with the photoactive site in oligomeric proteorhodopsin complexes. Acta Crystallogr. D Biol. Crystallogr. *69*, 1965–1980.

Robert, X., and Gouet, P. (2014). Deciphering key features in protein structures with the new ENDscript server. Nucleic Acids Res. *42*, W320–W324.

Rohou, A., and Grigorieff, N. (2015). CTFFIND4: fast and accurate defocus estimation from electron micrographs. J. Struct. Biol. *192*, 216–221.

Rozenberg, A., Oppermann, J., Wietek, J., Fernandez Lahore, R.G., Sandaa, R.-A., Bratbak, G., Hegemann, P., and Béjà, O. (2020). Lateral gene transfer of anion-conducting channelrhodopsins between green algae and giant viruses. Curr. Biol. *30*, 4910–4920.e5.

Sahel, J.-A., Boulanger-Scemama, E., Pagot, C., Arleo, A., Galluppi, F., Martel, J.N., Esposti, S.D., Delaux, A., de Saint Aubert, J.-B., de Montleau, C., et al. (2021). Partial recovery of visual function in a blind patient after optogenetic therapy. Nat. Med. *27*, 1223–1229.

Saitou, N., and Nei, M. (1987). The neighbor-joining method: a new method for reconstructing phylogenetic trees. Mol. Biol. Evol. *4*, 406–425.

Shibata, M., Inoue, K., Ikeda, K., Konno, M., Singh, M., Kataoka, C., Abe-Yoshizumi, R., Kandori, H., and Uchihashi, T. (2018). Oligomeric states of microbial rhodopsins determined by high-speed atomic force microscopy and circular dichroic spectroscopy. Sci. Rep. *8*, 8262.

Shibata, M., Nishimasu, H., Kodera, N., Hirano, S., Ando, T., Uchihashi, T., and Nureki, O. (2017). Real-space and real-Time dynamics of CRISPR-Cas9 visualized by high-speed atomic force microscopy. Nat. Commun. *8*, 1430.

Shigemura, S., Hososhima, S., Kandori, H., and Tsunoda, S.P. (2019). Ion channel properties of a cation channelrhodopsin. Gt_CCR4. Appl. Sci. *9*, 3440.

Shihoya, W., Inoue, K., Singh, M., Konno, M., Hososhima, S., Yamashita, K., Ikeda, K., Higuchi, A., Izume, T., Okazaki, S., et al. (2019). Crystal structure of heliorhodopsin. Nature *574*, 132–136.

Sineshchekov, O.A., Govorunova, E.G., Li, H., and Spudich, J.L. (2017). Bacteriorhodopsin-like channelrhodopsins: alternative mechanism for control of cation conductance. Proc. Natl. Acad. Sci. USA *114*, E9512–E9519.

Sineshchekov, O.A., Govorunova, E.G., Li, H., Wang, Y., Melkonian, M., Wong, G.K.S., Brown, L.S., and Spudich, J.L. (2020). Conductance mechanisms of rapidly desensitizing cation channelrhodopsins from cryptophyte algae. mBio *11*, 1–12.

Sridharan, S., Gajowa, M., Ogando, M.B., Jagadisan, U., Abdeladim, L., Sadahiro, M., Bounds, H., Hendricks, W.D., Tayler, I., Gopakumar, K., et al. (2021). High performance microbial opsins for spatially and temporally precise perturbations of large neuronal networks. bioRxiv, bioRxiv:2021.04.01.438134.

Takemoto, M., Kato, H.E., Koyama, M., Ito, J., Kamiya, M., Hayashi, S., Maturana, A.D., Deisseroth, K., Ishitani, R., and Nureki, O. (2015). Molecular dynamics of channelrhodopsin at the early stages of channel opening. PLoS One *10*, 1–15.

Tittor, J., Paula, S., Subramaniam, S., Heberle, J., Henderson, R., and Oesterhelt, D. (2002). Proton translocation by bacteriorhodopsin in the absence of substantial conformational changes. J. Mol. Biol. *319*, 555–565.

Trehan, A., Liu, R.S.H., Shichida, Y., Imamoto, Y., Nakamura, K., and Yoshizawa, T. (1990). On retention of chromophore configuration of rhodopsin isomers derived from three dicis retinal isomers. Bioorg. Chem. *18*, 30–40.

Tucker, A., Sridharan, S., Adesnik, H., and Brohawn, S.G. (2021). Cryo-EM structures of the channelrhodopsin ChRmine in lipid nanodiscs. bioRxiv, 2021.11.21.469454.

Tunyasuvunakool, K., Adler, J., Wu, Z., Green, T., Zielinski, M., Žídek, A., Bridgland, A., Cowie, A., Meyer, C., Laydon, A., et al. (2021). Highly accurate protein structure prediction for the human proteome. Nature *596*, 590–596.

Vogt, A., Guo, Y., Tsunoda, S.P., Kateriya, S., Elstner, M., and Hegemann, P. (2015). Conversion of a light-driven proton pump into a light-gated ion channel. Sci. Rep. *5*, 16450.

Volkov, O., Kovalev, K., Polovinkin, V., Borshchevskiy, V., Bamann, C., Astashkin, R., Marin, E., Popov, A., Balandin, T., Willbold, D., et al. (2017). Structural insights into ion conduction by channelrhodopsin 2. Science *358*, eaan8862.

Vonck, J. (2000). Structure of the bacteriorhodopsin mutant F219L N intermediate revealed by electron crystallography. EMBO J. *19*, 2152–2160.

Weinert, T., Skopintsev, P., James, D., Dworkowski, F., Panepucci, E., Kekilli, D., Furrer, A., Brünle, S., Mous, S., Ozerov, D., et al. (2019). Proton uptake mechanism in bacteriorhodopsin captured by serial synchrotron crystallography. Science *365*, 61–65.

Wietek, J., Wiegert, J.S., Adeishvili, N., Schneider, F., Watanabe, H., Tsunoda, S.P., Vogt, A., Elstner, M., Oertner, T.G., and Hegemann, P. (2014). Conversion of Channelrhodopsin into a light-gated chloride channel. Science *344*, 409–412.

Wu, S., Avila-Sakar, A., Kim, J., Booth, D.S., Greenberg, C.H., Rossi, A., Liao, M., Li, X., Alian, A., Griner, S.L., et al. (2012). Fabs enable single particle cryoEM studies of small proteins. Structure *20*, 582–592.

Yamashita, K., Palmer, C.M., Burnley, T., and Murshudov, G.N. (2021). Cryo-EM single-particle structure refinement and map calculation using Servalcat. Acta Crystallogr. D Struct. Biol. *77*, 1282–1291.

Yamauchi, Y., Konno, M., Ito, S., Tsunoda, S.P., Inoue, K., and Kandori, H. (2017). Molecular properties of a DTD channelrhodopsin from *Guillardia theta*. Biophys. Physicobiol. *14*, 57–66.

Yoshimura, K., and Kouyama, T. (2008). Structural role of bacterioruberin in the trimeric structure of Archaerhodopsin-2. J. Mol. Biol. *375*, 1267–1281.

Yun, J.-H., Li, X., Yue, J., Park, J.-H., Jin, Z., Li, C., Hu, H., Shi, Y., Pandey, S., Carbajo, S., et al. (2021). Early-stage dynamics of chloride ion-pumping rhodopsin revealed by a femtosecond X-ray laser. Proc. Natl. Acad. Sci. USA *118*, e2020486118.

Zhang, F., Prigge, M., Beyrière, F., Tsunoda, S.P., Mattis, J., Yizhar, O., Hegemann, P., and Deisseroth, K. (2008). Red-shifted optogenetic excitation: a tool for fast neural control derived from *Volvox carteri*. Nat. Neurosci. *11*, 631–633.

Zhang, J., Mizuno, K., Murata, Y., Koide, H., Murakami, M., Ihara, K., and Kouyama, T. (2013). Crystal structure of deltarhodopsin-3 from haloterrigena thermotolerans. Proteins *81*, 1585–1592.

Zhang, F., Vierock, J., Yizhar, O., Fenno, L.E., Tsunoda, S., Kianianmomeni, A., Prigge, M., Berndt, A., Cushman, J., Polle, J., et al. (2011). The microbial opsin family of optogenetic tools. Cell *147*, 1446–1457.

Zheng, S.Q., Palovcak, E., Armache, J.-P., Verba, K.A., Cheng, Y., and Agard, D.A. (2017). MotionCor2: anisotropic correction of beam-induced motion for improved cryo-electron microscopy. Nat. Methods *14*, 331–332.

Zivanov, J., Nakane, T., Forsberg, B.O., Kimanius, D., Hagen, W.J.H., Lindahl, E., and Scheres, S.H.W. (2018). New tools for automated high-resolution cryo-EM structure determination in RELION-3. Elife *7*, e42166.

Zivanov, J., Nakane, T., and Scheres, S.H.W. (2019). A Bayesian approach to beam-induced motion correction in cryo-EM single-particle analysis. IUCrJ *6*, 5–17.

Zivanov, J., Nakane, T., and Scheres, S.H.W. (2020). Estimation of high-order aberrations and anisotropic magnification from cryo-EM data sets in RELION-3.1. IUCrJ *7*, 253–267.

STAR★METHODS

KEY RESOURCES TABLE

REAGENT or RESOURCE	SOURCE	IDENTIFIER
Antibodies		
anti-HA	Fisher Scientific	Cat# A26183; RRID: AB_10978021
Mouse monoclonal Anti-ChRmine Fab01	This paper	N/A
Mouse monoclonal Anti-ChRmine Fab02	This paper	N/A
Mouse monoclonal Anti-ChRmine Fab03	This paper	N/A
Mouse monoclonal Anti-ChRmine Fab04	This paper	N/A
Mouse monoclonal Anti-ChRmine Fab05	This paper	N/A
Mouse monoclonal Anti-ChRmine Fab06	This paper	N/A
Bacterial and virus strains		
One shot Stbl3 e-coli	Thermo Fisher Scientific	Cat# C737303
Adeno-Associated Virus Coat Protein 2/8	Constructed in the Deisseroth lab; packaged at the Stanford Gene Vector and Virus Core (GVVC)	AAV8
AAV8-CaMKIIα-ChRmine-oScarlet-Kv2.1	Constructed in the Deisseroth lab; packaged at the Stanford GVVC	N/A
AAV8-CaMKIIα-rsChRmine-oScarlet-Kv2.1	Constructed in the Deisseroth lab; packaged at the Stanford GVVC	N/A
AAV8-CaMKIIα-hsChRmine-oScarlet-Kv2.1	Constructed in the Deisseroth lab; packaged at the Stanford GVVC	N/A
AAV8-CaMKIIα-XCaMP-G	Constructed in the Deisseroth lab; packaged at the Stanford GVVC	N/A
AAV8-CaMKIIα-XCaMP-B	Constructed in the Deisseroth lab; packaged at the Stanford GVVC	N/A
AAVdj-EF1α-DIO-GCaMP6f	Constructed in the Deisseroth lab; packaged at the Stanford GVVC	N/A
AAV8-EF1α-DIO-GCaMP6m-2A-rsChRmine-Kv2.1-HA	Constructed in the Deisseroth lab; packaged at the Stanford GVVC	N/A
AAV8-CaMKIIα-GCaMP6m-2A-rsChRmine-Kv2.1-HA	Constructed in the Deisseroth lab; packaged at the Stanford GVVC	N/A
AAV8-CaMKIIα-GCaMP6m-2A-ChRmine-Kv2.1-HA	Constructed in the Deisseroth lab; packaged at the Stanford GVVC	N/A
AAV8-CaMKIIα-GCaMP6m-2A-ChrimsonR-Kv2.1-HA	Constructed in the Deisseroth lab; packaged at the Stanford GVVC	N/A
E. coli Mach1	Thermo Fisher Scientific	Cat# C862003
E. coli DH10Bac	Thermo Fisher Scientific	Cat# 10361012
Chemicals, peptides, and recombinant proteins		
AP-V	Tocris	Cat# 0106
CNQX	Tocris	Cat# 0190
Tetrodotoxin	Tocris	Cat# 1078
Fluorodeoxyuridine	Sigma	Cat# F0503
Lipofectamine 2000	Thermo Fisher Scientific	Cat# 11668027
Benzamidine	Nacalai tesque	Cat# M9G4533
Leupeptin	Peptide Institute	Cat# 4041
n-Dodecyl-β-D-maltoside (DDM)	EMD Millipore	Cat# 324355
Glyco-diosgenin (GDN)	Anatrace	Cat# GDN101

(*Continued on next page*)

Continued

REAGENT or RESOURCE	SOURCE	IDENTIFIER
Cholesteryl hemisuccinate (CHS)	Sigma-Aldrich	Cat# C6512
FuGENE	Promega	Cat# E2311
Ni-NTA Superflow	QIAGEN	Cat# 30430
Superdex 200 increase 10/300 GL	Cytiva	Cat# 28990944
ENrich SEC 650 10 × 300	Bio-Rad	Cat# 7801650
All-trans-retinal (ATR)	Sigma-Aldrich	Cat# R2500
StockOptions pH buffer kit	Hampton Research	Cat# HR2-241
ESF 921 Insect Cell Culture Medium, Protein Free	Expression systems	Cat# 96-001-01
Deposited data		
ChRmine – atomic model	From this paper	PDB: 7W9W
ChRmine – Cryo-EM map	From this paper	EMDB-32377
ChRmine in complex with Fab02 – Cryo-EM map	From this paper	EMDB-32378
ChRmine in complex with Fab02 – Cryo-EM movie frames	From this paper	EMPIAR-10926
Experimental models: Cell lines		
Spodoptera frugiperda Sf9 cells	Expression systems	Cat# 94-001F
Primary rat hippocampal neuron	This paper	N/A
HEK293T	ATCC	Cat# CRL-3216
Experimental models: Organisms/strains		
C57BL/6J	Jackson	000664
Mouse: PV-2A-Cre (Pvalbtm1.1(cre)Aibs)	Jackson	012358
Sprague-Dawley rat pups	Charles River	N/A
Recombinant DNA		
pFastBac-ChRmine (WT)-EGFP-His10	This paper	N/A
pFastBac-ChRmine (D115N)-EGFP-His10	This paper	N/A
pFastBac-ChRmine (D253N)-EGFP-His10	This paper	N/A
pAAV-ChRmine(H33R)-eYFP	This paper	N/A
pAAV-ChRmine(R136H)-eYFP	This paper	N/A
pAAV-ChRmine(E70Q)-eYFP	This paper	N/A
pAAV-ChRmine(Y85F)-eYFP	This paper	N/A
pAAV-ChRmine(D115N)-eYFP	This paper	N/A
pAAV-ChRmine(D126N)-eYFP	This paper	N/A
pAAV-ChRmine(Y116F)-eYFP	This paper	N/A
pAAV-ChRmine(Y260F)-eYFP	This paper	N/A
pAAV-ChRmine(C120S)-eYFP	This paper	N/A
pAAV-ChRmine(C120T)-eYFP	This paper	N/A
pAAV-ChRmine(Y156N)-eYFP	This paper	N/A
pAAV-ChRmine(H96R)-eYFP	This paper	N/A
pAAV-ChRmine(S138W)-eYFP	This paper	N/A
pAAV-ChRmine(E69A)-eYFP	This paper	N/A
pAAV-ChRmine(T119A)-eYFP	This paper	N/A
pAAV-ChRmine(T119V)-eYFP	This paper	N/A
pAAV-ChRmine(Q71A)-eYFP	This paper	N/A
pAAV-ChRmine(I143D)-eYFP	This paper	N/A
pAAV-ChRmine(I146M)-eYFP	This paper	N/A
pAAV-ChRmine(G174S)-eYFP	This paper	N/A

(*Continued on next page*)

Continued

REAGENT or RESOURCE	SOURCE	IDENTIFIER
pAAV-ChRmine(F178Y)-eYFP	This paper	N/A
pAAV-ChRmine(I146M/G174S)-eYFP	This paper	N/A
pAAV-ChRmine(I146M/F178Y)-eYFP	This paper	N/A
pAAV-ChRmine(G174S/F178Y)-eYFP	This paper	N/A
pAAV-ChRmine(I146M/G174S/F178Y)-eYFP	This paper	N/A
pAAV-ChRmine(I146M/G174S/H33R)-eYFP	This paper	N/A
pAAV-ChRmine(R112A)-eYFP	This paper	N/A
pAAV-ChRmine(R112Q)-eYFP	This paper	N/A
pAAV-ChRmine(R136K)-eYFP	This paper	N/A
pAAV-ChRmine(R102A)-eYFP	This paper	N/A
pAAV-ChRmine(Q68R)-eYFP	This paper	N/A
pAAV-ChRmine(Q68E)-eYFP	This paper	N/A
pAAV-ChRmine(Q68K)-eYFP	This paper	N/A
pAAV-ChRmine(Q130A)-eYFP	This paper	N/A
pcDNA 3.1-ChRmine-eYFP	This paper	N/A
pcDNA 3.1-ChRmine(H33R)-eYFP	This paper	N/A
pcDNA 3.1-ChRmine(R136H)-eYFP	This paper	N/A
pcDNA 3.1-ChRmine(E70Q)-eYFP	This paper	N/A
pcDNA 3.1-ChRmine(Y85F)-eYFP	This paper	N/A
pcDNA 3.1-ChRmine(D115N)-eYFP	This paper	N/A
pcDNA 3.1-ChRmine(D126N)-eYFP	This paper	N/A
pcDNA 3.1-ChRmine(Y116F)-eYFP	This paper	N/A
pcDNA 3.1-ChRmine(Y260F)-eYFP	This paper	N/A
pcDNA 3.1-ChRmine(Y156N)-eYFP	This paper	N/A
pcDNA 3.1-ChRmine(H96R)-eYFP	This paper	N/A
pcDNA 3.1-ChRmine(S138W)-eYFP	This paper	N/A
pcDNA 3.1-ChRmine(E69A)-eYFP	This paper	N/A
pcDNA 3.1-ChRmine(T119A)-eYFP	This paper	N/A
pcDNA 3.1-ChRmine(T119V)-eYFP	This paper	N/A
pcDNA 3.1-ChRmine(Q71A)-eYFP	This paper	N/A
pAAV-ChroME2f	This paper	N/A
pAAV-ChroME2s	This paper	N/A
Software and algorithms		
Serial EM software	(Mastronarde, 2005)	https://bio3d.colorado.edu/SerialEM/
RELION 3.1	(Zivanov et al., 2018)	https://github.com/3dem/relion
MotionCor2	(Zheng et al., 2017)	https://emcore.ucsf.edu/ucsf-software
UCSF Chimera	(Pettersen et al., 2004)	https://www.cgl.ucsf.edu/chimera/
Chimera X	(Goddard et al., 2018)	https://www.rbvi.ucsf.edu/chimerax/
Coot	(Emsley and Cowtan, 2004)	https://www2.mrc-lmb.cam.ac.uk/personal/pemsley/coot/
CueMol2	N/A	http://www.cuemol.org/ja/index.php?cuemol2
Servalcat	(Yamashita et al., 2021)	https://github.com/keitaroyam/servalcat
MEGA 7	(Kumar et al., 2016)	https://www.megasoftware.net/
MATLAB	Mathworks	Mathworks.com
GraphPad Prism	GraphPad	Graphpad.com

(*Continued on next page*)

Continued

REAGENT or RESOURCE	SOURCE	IDENTIFIER
pClamp 10.6	Molecular Devices	https://www.moleculardevices.com
ImageJ (Fiji 1.48)	NIH	Fiji.sc
Other		
Optic fiber implants	Doric Lenses	Ordering Code: MFC_400/430-0.66_2.5mm_MF2.5_FLT
MultiClamp700B Amplifier	Molecular Devices	https://www.moleculardevices.com
DigiData 1440A	Molecular Devices	https://www.moleculardevices.com
DM-LFSA	Leica	N/A
Power meter	Thorlabs	PM100D
SPECTRA-X Light Engine	Lumencor	https://lumencor.com
R 1.2/1.3 grid: Au 300 mesh	QUANTIFOIL	Cat# N1-C14nAu30-01
AMICON MWCO 50,000	Merck / Millipore	Cat# UFC805024
AKTA pure 25 L1	Cytiva	Cat# 29018225
Fluorescence detection HPLC system	Shimadzu	Model Prominence
V-750 UV-Visible Spectrophotometer	JASCO	https://jascoinc.com/products/spectroscopy/
Vitrobot Mark IV	FEI / Thermo Fisher Scientific	https://www.thermofisher.com/jp/ja/home/electron-microscopy/products/sample-preparation-equipment-em/vitrobot-system.html
300 kV Titan Krios microscope	FEI / Thermo Fisher Scientific	Out of production; https://www.thermofisher.com/jp/ja/home/electron-microscopy/products/transmission-electron-microscopes.html
K3 Summit camera with post-column energy filter	Gatan / Quantum	https://www.gatan.com/K3
Innova S44i R	Eppendorf	Cat# S44I010226

RESOURCE AVAILABILITY

Lead contact

Further information and requests for resources and reagents should be directed to and will be fulfilled by the lead contact, Karl Deisseroth (deissero@stanford.edu).

Material availability

Plasmids/viruses and antibodies detailed in this manuscript are freely available for academic use from the Deisseroth Lab (http://www.optogenetics.org/sequence_info.html) and the Kato lab, respectively.

Data and code availability

The raw images of ChRmine before motion correction have been deposited in the Electron Microscopy Public Image Archive, under accession EMPIAR-10926. The cryo-EM density map and atomic coordinates for ChRmine have been deposited in the Electron Microscopy Data Bank and PDB, under accessions EMDB: EMD-32377 and PDB: 7W9W, respectively. The cryo-EM density map for ChRmine-Fab02 complex has been deposited in the Electron Microscopy Data Bank under accessions EMDB: EMD-32378. All other data are available upon request to the corresponding authors.

EXPERIMENTAL MODEL AND SUBJECT DETAILS

Insect cell culture

Spodoptera frugiperda (Sf9) cells (Expression systems, authenticated by the vendor) were cultured in ESF921 medium (Expression systems) at 27.5°C with 130 rpm in an Innova S44i R shaking incubator (Eppendorf).

Animals used for antibody generation

All the animal experiments conformed to the guidelines of the Guide for the Care and Use of Laboratory Animals of Japan and were approved by the Kyoto University Animal Experimentation Committee.

Primary neuron and HEK293 cell culture

Primary cultured hippocampal neurons were prepared from P0 Sprague-Dawley rat pups (Charles River). CA1 and CA3 were isolated, digested with 0.4 mg ml^{-1} papain (Worthington), and plated onto glass coverslips precoated with 1:30 Matrigel (Becton Dickinson Labware). Cultures were maintained in a 5% CO_2 humid incubator with Neurobasal-A media (Thermo Fisher) containing 1.25% FBS (HyClone), 4% B-27 supplement (Gibco), 2 mM Glutamax (Gibco) and 2 mg/ml fluorodeoxyuridine (FUDR, Sigma), and grown on coverslips in a 24-well plate at a density of 65,000 cells per well. HEK293FT cells (Thermo Fisher, authenticated by the vendor) were maintained in a 5% CO_2 humid incubator with DMEM media (GIBCO) supplemented with 10% FBS (Invitrogen), and 1% Penicillin-Streptomycin (Invitrogen), and were enzymatically passaged at 90% confluence by trypsinization.

Animals used for surgeries

All mouse experiments conformed to guidelines established by the National Institutes of Health and were conducted under protocols approved by the Stanford Administrative Panel on Laboratory Animal Care. All mice were group-housed in a light-regulated colony room (lights on at 07:00, off at 19:00), with food and water available ad libitum. Wild-type male and female C57BL/67 mice were obtained from Jackson Laboratory. Both male and female mice 4-20 weeks of age were used for all studies. Mice were bred in our colony (PV-Cre, PV-2A-Cre (Pvalbtm1.1(cre)Aibs/J, JAX 012358). All stereotactic surgeries were performed with mice under isoflurane anesthesia (4% initially, maintained at 2–3%) with regular monitoring for stable respiratory rate and absent tail pinch response. The scalp was shaved and mice were placed in the stereotactic apparatus and a heating pad was used to prevent hypothermia.

METHOD DETAILS

Cloning, Protein Expression, and Purification

Wild-type ChRmine (M1-R304, five amino acids at the C terminus truncated from the previous construct [Marshel et al., 2019]) was modified to include an N-terminal influenza hemagglutinin (HA) signal sequence and FLAG-tag epitope, and C-terminal enhanced green fluorescent protein (eGFP) and 10 × histidine tag; the N-terminal and C-terminal tags are removable by human rhinovirus 3C protease cleavage. The construct was expressed in *Spodoptera frugiperda* (*Sf9*) insect cells using the pFastBac baculovirus system. *Sf9* insect cells were grown in suspension to a density of 3.5 × 10^6 cells/mL, infected with ChRmine baculovirus and shaken at 27.5°C for 24 h. Then, 10 μM all-trans-retinal (ATR) (Sigma-Aldrich) was supplemented to the culture and shaken continued for 24 more hours. The cell pellets were lysed with a hypotonic lysis buffer (20 mM HEPES-NaOH pH 7.5, 20 mM NaCl, 10 mM $MgCl_2$, 1 mM benzamidine, 1 μg/ml leupeptin, 10 μM ATR), and cell pellets were collected by centrifugation at 10,000 ×g for 30 min. The above process was repeated twice; then, cell pellets were disrupted by homogenizing with a glass dounce homogenizer in a hypertonic lysis buffer (20 mM HEPES-NaOH pH 7.5, 1 M NaCl, 10 mM $MgCl_2$, 1 mM benzamidine, 1 μg/ml leupeptin, 10 μM ATR), and crude membrane fraction was collected by ultracentrifugation (45Ti rotor, 125,000 ×g for 1 h). The above process was repeated twice; then, the membrane fraction was homogenized with a glass douncer in a solubilization buffer (1% *n*-dodecyl-β-D-maltoside (DDM) (EMD Millipore), 0.2% cholesteryl hemisuccinate (CHS) (Sigma-Aldrich), 20 mM HEPES-NaOH pH 7.5, 500 mM NaCl, 20% glycerol, 5 mM imidazole, 1 mM benzamidine, 1 μg/ml leupeptin) and solubilized for 2 h in 4 °C. The insoluble cell debris was removed by centrifugation (125,000 ×g, 1 h), and the supernatant was mixed with the Ni-NTA superflow resin (QIAGEN) for 1 h in 4 °C. The Ni-NTA resin was collected into a glass chromatography column, washed with 2.5 CV wash 1 buffer (0.05% DDM, 0.01% CHS, 20 mM HEPES-NaOH pH7.5, 100 mM NaCl, 50 mM imidazole), 2.5 CV wash 2 buffer (0.05% DDM, 0.06% GDN (glyco-diosgenin), 0.016% CHS, 20 mM HEPES-NaOH pH7.5, 100 mM NaCl, 50 mM imidazole), and 2.5 CV wash 3 buffer (0.06% GDN, 0.006% CHS, 20 mM HEPES-NaOH pH7.5, 100 mM NaCl, 50 mM imidazole), and was eluted in a wash 3 buffer supplemented with 300 mM imidazole. After cleavage of the FLAG tag and eGFP-His_{10} tag His-tagged 3C protease, the sample was reloaded onto the Ni-NTA column to capture the cleaved eGFP-His_{10}. The flow-through containing ChRmine was collected, concentrated, and purified through gel-filtration chromatography in a final buffer (20 mM HEPES-NaOH pH7.5, 100 mM NaCl, 0.03% GDN, 0.003% CHS).

Antibody generation

Mouse monoclonal antibodies against ChRmine were raised according to previously-described methods (Jaenecke et al., 2018). Briefly, a proteoliposome antigen was prepared by reconstituting purified, functional ChRmine at high density into phospholipid vesicles consisting of a 10:1 mixture of chicken egg yolk phosphatidylcholine (egg PC; Avanti Polar Lipids) and the adjuvant lipid A (Sigma-Aldrich) to facilitate immune response. BALB/c mice were immunized with the proteoliposome antigen using three injections at two-week intervals. Antibody-producing hybridoma cell lines were generated using a conventional fusion protocol. Biotinylated proteoliposomes were prepared by reconstituting ChRmine with a mixture of egg PC and 1,2-dipal-mitoyl-*sn*-glycero-3-phosphoethanolamine-N-(cap biotinyl) (16:0 biotinyl Cap-PE; Avanti), and used as binding targets for conformation-specific antibody selection. The targets were immobilized onto streptavidin-coated microplates (Nunc). Hybridoma clones producing anti-

bodies recognizing conformational epitopes in ChRmine were selected by an enzyme-linked immunosorbent assay on immobilized biotinylated proteoliposomes (liposome ELISA), allowing positive selection of the antibodies that recognized the native conformation of ChRmine. Additional screening for reduced antibody binding to SDS-denatured ChRmine was used for negative selection against linear epitope-recognizing antibodies. Stable complex formation between ChRmine and each antibody clone was checked using fluorescence-detection size-exclusion chromatography. The sequence of the Fab from the antibody clone number YN7002_7 (named as Fab02) was determined via standard 5'-RACE using total RNA isolated from hybridoma cells.

Formation and purification of the ChRmine-Fab02 complex

Purified ChRmine was mixed with a fourfold molar excess of Fab, and the coupling reaction proceeded at 4°C overnight. The ChRmine-Fab02 complex was purified by size exclusion chromatography on a Superdex 200 increase 10/300 GL column (Cytiva) in 20 mM HEPES-NaOH pH7.5, 100 mM NaCl, 0.03% GDN, 0.003% CHS. Peak fractions were concentrated to about 15 mg/mL for electron microscopy studies.

Cryo-EM data acquisition and image processing

Cryo-EM images were acquired at 300 kV on a Krios G3i microscope (Thermo Fisher Scientific) equipped with a Gatan BioQuantum energy filter and a K3 direct detection camera in the electron counting mode. The movie dataset was collected in a correlated double sampling (CDS) mode, using a nine-hole image shift strategy in the SerialEM software (Mastronarde, 2005), with a nominal defocus range of 0.8 to 1.6 μm. The 3,528 movies were acquired at a dose rate of 6.3 e^-/pixel/s, at a pixel size of 0.83 Å and a total dose of 46 $e^-/Å^2$.

Image processing was performed in RELION-3.1 (Zivanov et al., 2018). Beam-induced motion correction and dose weighting were performed with RELION's implementation of the MotionCor2 algorithm (Zheng et al., 2017), and CTF parameters were estimated with CTFFIND-4.1.13 (Rohou and Grigorieff, 2015). Particles were first picked using the Laplacian-of-gaussian algorithm, and 2D class average images were generated as templates for reference-based auto-picking. Reference-based picked 2,958,159 particles were subjected to several rounds of 2D and 3D classifications. The selected 555,801 particles were subjected to a 3D auto-refinement, resulting in a 2.8 Å map. Subsequently, Bayesian polishing (Zivanov et al., 2019) and CTF refinement (Zivanov et al., 2020), followed by a 3D auto-refinement, resulted in a 2.6 Å map. Micelle and constant regions of Fab fragments densities were subtracted from particle images, and the subtracted particles were subjected to a masked 3D classification without alignment. After a 3D auto-refinement of selected 185,895 particles, three runs of CTF refinement were performed in order as follows: refining magnification anisotropy; refining optical aberrations; refining per-particle defocus and per-micrograph astigmatism. Another round of 3D auto-refinement yielded a 2.12 Å map. These particles were subjected to a second round of Bayesian polishing, CTF refinement and a transmembrane region-focused 3D auto-refinement with the reconstruction algorithm SIDESPLITTER (Ramlaul et al., 2020), resulting in the final map at a global resolution of 2.02 Å. Following our initial report (Kishi et al., 2021), the utility of cryo-EM for ChRmine was reported in a second preprint (2.7–4.1 Å resolution)(Tucker et al., 2021), suggesting this approach may be broadly useful.

Model building and refinement

An initial model was formed by rigid body fitting of the C1C2 (PDB: 3UG9) (Kato et al., 2012). This starting model was then subjected to iterative rounds of manual and automated refinement in Coot (Emsley and Cowtan, 2004) and Refmac5 (Murshudov et al., 2011) in Servalcat pipeline (Yamashita et al., 2021), respectively. The Refmac5 refinement was performed with the constraint of C3 symmetry. The final model was visually inspected for general fit to the map, and geometry was further evaluated using Molprobity (Chen et al., 2010). The final refinement statistics is summarized in Table S1. All molecular graphics figures were prepared with UCSF Chimera (Pettersen et al., 2004), UCSF ChimeraX (Goddard et al., 2018), and CueMol2 (http://www.cuemol.org).

Pore analysis

The ion-conducting pore pathways were calculated by the software HOLLOW using a grid-spacing of 1.0 Å. The electrostatic potentials of the pores are calculated by PDB2PQR server (Baker et al., 2001; Dolinsky et al., 2004). Trimer opening radii of ChRmine were calculated with HOLE.

Analysis of F_o-F_c difference densities

Our 2.0 Å cryo-EM map allowed accurate modeling of ATR and surrounding residues, but the C13 and C14 atoms of ATR and W223 showed weaker density in this region. Moreover, positive and negative F_o-F_c difference densities were observed around W223, suggesting that this cryo-EM density map contains information on a small population of early intermediate states (possibly the K intermediate; (Figures S2Q and S2R). While we could not detect further structural changes propagated from W223, the extent of the conformational change in ChRmine W223 was significantly larger than that in C1C2 and similar to that of *Hs*BR (Oda et al., 2021; Weinert et al., 2019). Thus, the initial conformational changes of the ChRmine photocycle may be more similar to those of ion-pumping rhodopsins than of canonical chlorophyte channelrhodopsins. In *Hs*BR, it is known that the isomerized retinal pushes against W182 (W223 in ChRmine) and the movement of W182 on TM6 triggers a large outward movement of the cytoplasmic side of TM6 in the later intermediate state (Vonck, 2000; Weinert et al., 2019). Therefore, a similar conformational change (i.e. the outward movement of TM6) may well also occur in later intermediate state in ChRmine, and this would be the key movement for initiation of cation

conduction via enlarging the cytoplasmic pore. It has been reported that large movement of TM6 in *Hs*BR is not necessary for proton pumping (Tittor et al., 2002); thus, if TM6 moves and the TM6 movement is necessary for cation conduction in ChRmine, this may suggest that the TM6 movement of *Hs*BR would be the initial step to acquiring channel function during evolution.

Analysis of conserved Arg conformations among microbial rhodopsins

The Arg conformations have been analyzed for C1C2 (PDB: 3UG9) (Kato et al., 2012), *Cr*ChR2 (PDB: 6EID) (Volkov et al., 2017), C1Chrimson (PDB: 5ZIH) (Oda et al., 2018), *Gt*ACR1 (PDB: 6CSM) (Kim et al., 2018), ChRmine (this study), *Hs*BR (PDB: 5ZIM) (Hasegawa et al., 2018), *Hw*BR (PDB: 4QID), cruxrhodopsin-3 (PDB: 4JR8) (Chan et al., 2014), deltarhodopsin (PDB: 4FBZ) (Zhang et al., 2013), GR (PDB: 6NWD) (Morizumi et al., 2019), Archaerhodopsin-1 (PDB: 1UAZ) (Enami et al., 2006), Archaerhodopsin-2 (PDB: 2EI4) (Yoshimura and Kouyama, 2008), PR from the Mediterranean Sea at a depth of 12 m (*Med12*BPR, PDB: 4JQ6) (Ran et al., 2013), PR from the Pacific Ocean near Hawaii at a depth of 75 m (*HOT75*BPR, PDB: 4KLY) (Ran et al., 2013), *Cs*R (PDB: 6GYH) (Fudim et al., 2019), *Hs*HR (PDB: 1E12) (Kolbe et al., 2000), *Np*HR (PDB: 3A7K) (Kouyama et al., 2010), ClR (PDB: 5ZTK) (Yun et al., 2021), KR2 (PDB: 3X3C) (Kato et al., 2015a), and schizorhodopsin 4 (PDB: 7E4G) (Higuchi et al., 2021).

In all structurally-resolved channelrhodopsins (C1C2, *Cr*ChR2, C1Chrimson, *Gt*ACR1, and ChRmine), the arginine residue faces outward. In contrast, in many ion-pumping rhodopsins, including *Hs*BR, *Hw*BR, cruxrhodopsin-3, deltarhodopsin, GR, Archaerhodopsin-1, Archaerhodopsin-2, *Med12*BPR, *HOT75*BPR, *Cs*R, *Hs*HR, *Np*HR, ClR, KR2, and schizorhodopsin 4, the tip of arginine runs parallel to the membrane and faces TM1. The arginine in the parallel conformation narrows or blocks the extracellular cavity of the ion-translocating pathway; thus, this conformation would contribute to preventing large ion flux in ion-pumping rhodopsins.

High performance liquid chromatography (HPLC) analysis of retinal isomers

The retinal isomers were analyzed with an HPLC system equipped with a silica column (particle size 3 μm, 150 × 6.0 mm; Pack SIL, YMC, Japan), a pump (PU-4580, JASCO, Japan) and a UV–Visible detector (UV-4570, JASCO, Japan). The purified sample in a buffer containing 20 mM HEPES-NaOH pH 7.5, 100 mM NaCl, 0.035% GDN, 0.0035% CHS (GDN:CHS = 10:1) were dark-adapted for two days at 4 °C. A 75 μL sample and 280 μL of 90% (v/v) methanol aqueous solution were mixed on ice and then 25 μL of 2 M hydroxylamine (NH_2OH) was added to convert retinal chromophore into retinal oxime, which was extracted with 800 μL of *n*-hexane. A 200 μL of the extract was injected into the HPLC system. The solvent containing 15% ethyl acetate and 0.15% ethanol in hexane was used as a mobile phase at a flow rate of 1.0 mL min^{-1}. Illumination was performed on ice with green light (530 ± 5 nm) for 20 s for samples under illumination and 60 s for light adaptation. The molar composition of the sample was calculated from the areas of the peaks and the molar extinction coefficients at 360 nm (all-*trans*-15-*syn*: 54,900 $M^{-1}cm^{-1}$; all-*trans*-15-*anti*: 51,600 $M^{-1}cm^{-1}$; 13-*cis*-15-*syn*, 49,000 $M^{-1}cm^{-1}$; 13-*cis*-15-*anti*: 52,100 $M^{-1}cm^{-1}$; 11-*cis*-15-*syn*: 35,000 $M^{-1}cm^{-1}$; 11-*cis*-15-*anti*: 29,600 $M^{-1}cm^{-1}$) (Trehan et al., 1990).

Preparation of lipid-reconstituted ChRmine for high-speed AFM imaging

For HS-AFM imaging of lipid-reconstituted ChRmine, we applied membrane scaffolding proteins (MSP), which were developed for nanodisc technology (Bayburt et al., 2002; Denisov and Sligar, 2016). We followed the manufacturer's protocol for the nanodisc (Sigma-Aldrich, St. Louis, MO, USA) with minor modifications as described previously (Shibata et al., 2018). Briefly, for reconstituted lipids, we used a mixture of phospholipids, asolectin from soybean (Sigma-Aldrich, No. 11145). Asolectin (120 μg) was dissolved in chloroform and then evaporated under N_2 gas to completely remove the solvent. Then, the lipids were suspended in 50 μL buffer A (20 mM HEPES-KOH pH 7.4, 100 mM NaCl, and 4% DDM) and sonicated for ~1 min with a tip-sonicator. Next, dissolved membrane proteins (1 nmol) and MSP (50 μL, 1 mg/mL) (MSP1E3D1, Sigma-Aldrich, No. M7074) were added to the lipid suspension and mixed for ~1 h while rotating in the dark at 4°C. Finally, we added 60 mg Bio-beads SM-2 (Bio-Rad, Hercules, CA, USA, No. 1523920) and dialyzed the samples in detergent overnight at 4°C. According to the manufacturer's protocol, nanodisc samples should be fractionated on a column to purify the nanodiscs based on size (~10 nm in diameter). Here, we did not purify the reconstituted samples, but obtained flat membranes with limited sizes <30 nm in diameter.

High-speed AFM measurements

A homemade HS-AFM operated in tapping mode was used (Shibata et al., 2017, 2018). An optical beam deflection detector detected the cantilever (Olympus, Tokyo, Japan: BL-AC10DS-A2) deflection using an infrared (IR) laser at 780 nm and 0.7 mW. The IR beam was focused onto the back side of the cantilever covered with a gold film through a ×60 objective lens (Nikon, Tokyo, Japan: CFI S Plan Fluor ELWD 60x). The reflected IR beam was detected by a two-segmented PIN photodiode. The free oscillation amplitude of the cantilever was ~1 nm and set-point amplitude was approximately 90% of the free amplitude for feedback control of HS-AFM observation. An amorphous carbon tip (~500 nm length), grown by electron beam deposition by scanning electron microscope, was used as an AFM probe. As a HS-AFM substrate, a mica surface treated with 0.01% (3-aminopropyl) triethoxysilane (Shin-Etsu Silicone, Tokyo, Japan) was used. All HS-AFM experiments were carried out in buffer solution containing 20 mM Tris–HCl pH 8.0 and 100 mM NaCl at room temperature (24–26°C) and data analyses were conducted using laboratory-developed software based on IgorPro 8 software (WaveMetrics, USA). We usually used a scan area of 43 × 32 nm^2 with 130 × 95 pixels. HS-AFM images were captured at frame rates of 2 fps. All HS-AFM images were processed by Gaussian noise-reduction filters.

Measurement of UV absorption spectra

For pH titration, the final purified product (20 mM HEPES-NaOH pH7.5, 100 mM NaCl, 0.03% GDN, 0.003% CHS) was diluted with 100 mM of the respective pH buffer (StockOptions pH Buffer Kit), and the UV-Vis spectra were measured.

Laser flash photolysis

For the laser flash photolysis spectroscopy, wildtype ChRmine was solubilized in 20 mM HEPES-NaOH pH 7.5, 100 mM NaCl, 0.035% GDN, 0.0035% CHS (GDN:CHS = 10:1) or 20 mM sodium acetate pH 4.0, 100 mM NaCl, 0.03% GDN, 0.003% CHS (GDN:CHS = 10:1), and ChRmine D115N and D253N mutants were solubilized in 20 mM sodium acetate pH 4.0, 100 mM NaCl, 0.03% GDN, 0.003% CHS (GDN:CHS = 10:1). The optical density of the protein solution was adjusted to ~0.4 (protein concentration ~0.28 mg/mL) at the absorption maximum wavelengths. The laser flash photolysis measurements were conducted as previously described (Inoue et al., 2013). ChRmine wildtype at pH 7.5 was excited by the second harmonics of a nanosecond-pulsed Nd-YAG laser (excitation wavelength (λ_{exc}) = 532 nm, 4.5 mJ/pulse, 1.4–0.5 Hz, INDI40, Spectra-Physics, CA), and nanosecond pulse from an optical parametric oscillator (4.5 mJ/pulse, basiScan, Spectra-Physics, CA) pumped by the third harmonics of Nd-YAG laser (λ = 355 nm, INDI40, Spectra-Physics, CA) was used for the excitation of ChRmine wildtype at pH 4.0 (λ_{exc} = 505 nm), ChRmine D115N (λ_{exc} = 488 nm) and D253N (λ_{exc} = 500 nm). Transient absorption spectra were obtained by monitoring the intensity change of white-light from a Xe-arc lamp (L9289-01, Hamamatsu Photonics, Japan) passed through the sample with an ICCD linear array detector (C8808-01, Hamamatsu, Japan). To increase the signal-to-noise (S/N) ratio, 45–60 spectra were averaged, and the singular-value-decomposition (SVD) analysis was applied. To measure the time-evolution of transient absorption change at specific wavelengths, the light of Xe-arc lamp (L9289-01, Hamamatsu Photonics, Japan) was monochromated by monochromators (S-10, SOMA OPTICS, Japan) and the change in the intensity after the photo-excitation was monitored with a photomultiplier tube (R10699, Hamamatsu Photonics, Japan). To increase S/N ratio, 100–200 signals were averaged. The time-evolution of transient absorption change was analyzed by global multi-exponential fitting to determine the time constant of each reaction step and absorption spectra of the photo-intermediates. Some reaction steps were reproduced by double or triple exponentials. In this case, the averaged time constant calculated by

$$\tau_{ave} = \frac{\sum_i A_i / k_i}{\sum_i A_i}$$

where A_i and k_i are the amplitude at a wavelength of representing the M-intermediate and the rate constant of i-th exponential function (i = 1–3).

Molecular cloning

All ChRmine mutant plasmids were constructed in AAV-CaMKIIa or pcDNA 3.1 backbones using overlapping PCR as described previously (Fenno et al., 2020; Marshel et al., 2019). Every plasmid was sequence-verified.

Primary cell transfection

For neuronal transfection, 2.0 μg plasmid DNA was mixed with 1.875 μL 2 M $CaCl_2$ (final Ca^{2+} concentration 250 mM) in 15 μL H_2O. To DNA-$CaCl_2$ we added 15 μL of 2× HEPES-buffered saline pH 7.05. After 20 min at room temperature (20–22 °C), the mix was added dropwise into each well (from which the growth medium had been removed and replaced with pre-warmed minimal essential medium (MEM)) and transfection proceeded for 45–60 min at 37 °C, after which each well was washed with 3 × 1 ml warm MEM before the original growth medium was returned. Neurons were allowed to express transfected DNA for 6-8 days prior to experiments.

For HEK cell transfection, 0.8 μg plasmid DNA was mixed with 2 μL Lipofectamine 2000 (Invitrogen) in 100 μL Opti-MEM (Invitrogen, incubated at room temperature (20–22 °C) for 20 minutes, and the mix was added dropwise into each well (from which the growth medium had been removed and replaced with 400 μL pre-warmed Opti-MEM). Transfection proceeded for two hours at 37 °C, after which the transfection media was replaced by normal HEK cells growth media. Cells were allowed to express transfected DNA for 2-3 days prior to experiments.

Virus production

AAV-8 (Y733F), was produced by the Stanford Neuroscience Gene Vector and Virus Core. In brief, AAV8 was produced by standard triple transfection of AAV 293 cells (Agilent). At 72 h post transfection, the cells were collected and lysed by a freeze-thaw procedure. Viral particles were then purified by an iodixanol step-gradient ultracentrifugation method. The iodixanol was diluted and the AAV was concentrated using a 100-kDa molecular mass–cutoff ultrafiltration device. Genomic titer was determined by quantitative PCR. All viruses were tested in cultured neurons for expected expression patterns prior to use *in vivo*.

In vitro electrophysiology in HEK293 cells

HEK293 cells transfected with pcDNA3.1(+) plasmids were placed in an extracellular tyrode medium (150 mM NaCl, 4 mM KCl, 2 mM $CaCl_2$, 2 mM $MgCl_2$, 10 mM HEPES pH 7.4, and 10 mM glucose). Borosilicate patch pipettes (Harvard Apparatus) with resistance of 4 – 6 MOhm were filled with intracellular medium (140 mM potassium-gluconate, 10 mM EGTA, 2 mM $MgCl_2$ and 10 mM HEPES pH

7.2). Light was delivered with the Spectra X Light engine (Lumencor) connected to the fluorescence port of a Leica DM LFSA microscope with a 580 nm filter for orange light generation.

Channel kinetics and photocurrent amplitudes were measured in voltage clamp mode at -70 mV holding potential. To determine channel kinetics and photocurrent amplitudes, traces were first smoothed using a lowpass Gaussian filter with a −3 dB cutoff for signal attenuation and noise reduction at 1,000 Hz and then analysed in Clampfit software (Axon Instruments). Liquid junction potentials were corrected using the Clampex built-in liquid junction potential calculator as previously described. Statistical analysis was performed with t-test or one-way ANOVA, and the Kruskal–Wallis test for non-parametric data, using Prism 7 (GraphPad) software. Data collection across opsins was randomized and distributed to minimize across-group differences in expression time, room temperature, and related experimental factors.

Ion selectivity testing in HEK293 cells

HEK293 cells and devices for the measurement were prepared as described in the previous section. For the high sodium extracellular / high potassium intracellular condition, we used sodium bath solution containing 120 mM NaCl, 4 mM KCl, 2 mM $CaCl_2$, 2 mM $MgCl_2$, and 10 mM HEPES pH 7.2 (with glucose added up to osm 310 mOsm), along with potassium pipette solution containing 120 mM KCl, 10 mM EGTA, 4 mM NaCl, 2 mM $CaCl_2$, 2 mM $MgCl_2$, and 10mM HEPES pH 7.2 (with glucose added up to osm ~290). For the high potassium extracellular / high sodium intracellular condition, NaCl and KCl concentrations were reversed, and all other ionic concentrations were kept constant. For ion selectivity measurements, ions in both bath and pipette solutions were replaced with either 120 mM NaCl, 120 mM KCl, 80 mM $CaCl_2$, 80 mM $MgCl_2$ or 120 mM NMDG-Cl, with all other components at low concentrations (4 mM NaCl, 4 mM KCl, 2 mM $CaCl_2$, 2 mM $MgCl_2$, and 10mM HEPES). Glucose was added to increase intracellular solution to 310 mOsm and extracellular solution to 290 osm. Photocurrent amplitudes were measured at -70 mV holding membrane potential. Equilibrium potentials were measured by holding membrane potentials from -75 mV to + 45 mV in steps of 10 mV.

In vitro one-photon electrophysiology in cultured hippocampal neurons

Primary rat hippocampal cultured neurons were transfected with pAAV ChRmine-bearing plasmids and were measured in the same setup as described in the HEK293 electrophysiology section. Voltage clamp recordings were performed in the presence of bath-applied tetrodotoxin (TTX, 1 μM, Tocris). For screening of action spectra, cells were held at resting potential of -70 mV, with 1.0 mW/mm^2 light delivery for 1 sec at wavelengths (in nm) of 390, 438, 485, 513, 585 and 650, which were generated using filters of corresponding peak wavelengths and 15-30 nm bandwidth. Channel kinetics and photocurrent amplitudes were measured at -70 mV holding membrane potential. Liquid junction potentials were corrected using the Clampex built-in liquid junction potential calculator as previously described. Current clamp measurements were performed in the presence of glutamatergic synaptic blockers: 6-cyano-7-nitroquinoxaline-2,3,-dione (CNQX; 10 μM, Tocris) and D(-)-2-amino-5-phosphonovaleric acid (APV; 25 μM, Tocris).

For light pulse-width experiments, 585 nm light with 5 Hz frequency and 0.7 mW/mm^2 intensity was used at varying pulse-width values (in ms) of 0.5, 1, 2, 5 and 10. For light sensitivity experiments, 585 nm light with 5 Hz frequency and 5 ms pulse-width was used at varying light power densities (in mW/mm^2) of 0.003, 0.01, 0.03, 0.1, 0.3, 0.7, and 1.0. For spike fidelity experiments, 585 nm light with 0.7 mW/mm^2 power density was used, with 1 ms pulse-width for ChRmine variants. Data collection across opsins was randomized and distributed to minimize across-group differences in expression time, room temperature, and related experimental factors. Statistical analysis was performed with t-test or one-way ANOVA, and the Kruskal–Wallis test with Dunn's test for multiple comparisons for non-parametric data, using Python and Prism 7 (GraphPad) software.

In vitro two-photon electrophysiology

All two-photon electrophysiology experiments were performed with cultured hippocampal neurons in the same intracellular and extracellular solutions as for one-photon electrophysiology characterization. Experiments were conducted on a commercial microscope (Bruker Ultima running PrairieView v5.4) using a Nikon 16×/0.8 NA (CFI75) long-working distance objective for light delivery. For two-photon stimulation, spiral scanning was performed through a defined spiral ROI with 15 μm diameter, with 10 rotations per spiral, and 1.3 ms total exposure duration with 80 MHz laser repetition rate (Coherent Discovery). The axial point-spread-function FWHM of the two-photon stimulation beam was measured to be 6.9+/-0.2 μm at 920 nm using 1 μm diameter beads (Invitrogen Focal Check Slide #1, F36909).

For two-photon action spectra characterization, recordings were conducted in voltage clamp mode at holding voltage of -75 mV. Action spectra were measured in randomized trial order at wavelengths (in nm) of 825, 850, 900, 950, 1000, 1050, 1100, 1150, 1200, 1250, and 1300 at a laser power of 20 mW. We measured the focal shift as we systematically varied wavelengths from 825 to 1300 nm and found that there was a ~25 um difference in focus between 825 and 1300 nm. Therefore, the z-focus was adjusted to compensate for empirically measured focal shifts during randomized wavelength delivery.

No steps were taken to compensate for the potential effects of pulse broadening due to spectral dispersion. All measurements were normalized by the maximum value of the single recording session and then averaged across cells.

Stereotactic surgeries

A midline incision was made to expose the skull and small craniotomies were made above the injection sites using a Meisinger Carbide Burr size 1/4. All virus dilutions were performed in ice-cold PBS and all viruses were produced at the Stanford Gene and Viral Vector Core. Virus injections were delivered with a 10 μL syringe (World Precision Instruments) and 33-gauge beveled needle (World Precision Instruments), injected at 100 nL min^{-1} using an injection pump (World Precision Instruments). For slice physiology experiments, mice were injected with either AAV8-CaMKIIα-ChRmine-p2A-oscarlet (2.0e13 vg/mL) or AAV8-CaMKIIα-rsChRmine-p2A-Oscarlet (7.30e12 vg/mL). One microliter of virus was stereotactically injected bilaterally into the motor cortex of 8-12 week old mice at 1.7 mm AP, 0.75 mm ML, and 1.5 mm DV from the bregma. For fiber photometry experiments, mice were injected with either AAV8-CaMKIIα-GCaMP6m-2A-opsin where "opsin" is one of the three opsins shown in Figure 7: rsChRmine (1.0e12 vg/ml), WT ChRmine (1.0e12 vg/ml), or ChrimsonR (1.0e12 vg/ml). For type-to-type experiments, PV-2a-Cre mice were injected with either a mixture of AAV8-CaMKIIα-rsChRmine-oScarlett-Kv2.1 (3.0e12 vg/ml), AAV8-CaMKIIα-XCaMP-B (8.0e12 vg/ml), and AAVdj-EF1α-DIO-GCaMP6f (3.0e12 vg/ml) or a mixture of AAV8-CaMKIIα-XCaMP-B (8.0e12 vg/ml) and AAV8-EF1α-DIO-GCaMP6m-2A-rsChRmine (5.0e11 vg/ml). 0.7 μl of virus was stereotactically injected unilaterally into the mPFC of 8-12 week old mice at 1.8 mm AP, 0.35 mm ML, and 2.4 mm DV from the bregma. Following injection, the injection needle was held at the injection site for 10 min then slowly withdrawn. Mice were administered 0.5–1.0 mg kg^{-1} subcutaneous buprenorphine-SR (ZooPharma) approximately 30 min before the end of the surgery for post-operative pain management.

Acute slice electrophysiology

Recordings of rsChRmine and ChRmine-expressing pyramidal cells were performed in acute slices from wild-type C57BL/6 mice 4-5 weeks after virus injection. Coronal slices 300 μm in thickness were prepared after intracardial perfusion with ice-cold *N*-methyl-d-glucamine (NMDG) containing cutting solution: 93 mM NMDG, 2.5 mM KCl, 25 mM glucose, 1.2 mM NaH_2PO_4, 10 mM $MgSO_4$, 0.5 mM $CaCl_2$, 30 mM $NaHCO_3$, 5 mM Na ascorbate, 3 mM Na pyruvate, 2 mM thiourea and 20 mM HEPES pH 7.3–7.4. Slices were incubated for 12 min at 34 °C, and then were transported to room temperature oxygenated artificial cerebrospinal fluid (ACSF) solution: 124 mM NaCl, 2.5 mM KCl, 24 mM $NaHCO_3$, 2 mM $CaCl_2$, 2 mM $MgSO_4$, 1.2 mM NaH_2PO_4, 12.5 mM glucose and 5 mM HEPES pH 7.3–7.4.

Current clamp measurements were performed as described in the in vitro electrophysiology section. Briefly, 585 nm light with 5 Hz frequency and 0.7 mW/mm^2 intensity was used at varying pulse-width values (in ms) of 0.5, 1, 2, 5 and 10 to test pulse width, and 585 nm light with 5 Hz frequency and 5 ms pulse-width was used at varying light power densities (in mW/mm^2) of 0.003, 0.01, 0.03, 0.1, 0.3, 0.7, and 1.0. For spike fidelity experiments, 585 nm light with 0.7 mW/mm^2 power density was used, with 1 ms pulse-width for ChRmine variants. Data collection across opsins was randomized and distributed to minimize across-group differences in expression time, room temperature, and related experimental factors.

In vitro characterization using all-optical physiology methods

Dissociated hippocampal neurons were cultured and infected with both red-shifted opsin variants and XCaMP-G or XCaMP-B as previously described (Marshel et al., 2019). One microliter viral suspension of WT ChRmine (AAV8-CaMKIIα-ChRmine-oScarlet-Kv2.1, 1.3e13 vg/mL), rsChRmine (AAV8-CaMKIIα-rsChRmine-oScarlet-Kv2.1, 8.8e12 vg/mL), or hsChRmine (AAV8-CaMKIIα-hsChRmine-oScarlet-Kv2.1, 1.8e13 vg/ml) mixed with 1 μL XCaMP-G (AAV8-CaMKIIα-XCaMP-G, 6.9e12 vg/mL)) or 1 μL XCaMP-B (AAV8-CaMKIIα-XCaMP-B, 2.4e13 vg/mL) was added after 5 DIV. Cultured neurons were used between 12 and 14 DIV for experiments. Coverslips of cultured neurons were transferred from the culture medium to a recording bath filled with Tyrode's solution containing (129 mM NaCl, 5 mM KCl, 30 mM glucose, 25 mM HEPES-NaOH pH 7.4, 1 mM $MgCl_2$ and 3 mM $CaCl_2$) supplemented with 10 μM CNQX and 25 μM APV to prevent contamination from spontaneous and recurrent synaptic activity. Optical stimulation and imaging were performed using a 40×/0.6-NA objective (Leica), sCMOS camera (Hamamatsu, ORCA-Flash4.0) and LED light source (Spectra X Light engine, Lumencor), all coupled to a Leica DMI 6000 B microscope. XCaMP-B or XCaMP-G were excited by 390 nm (Semrock, FF01-390/18) or 488 nm (Semrock, LL01-488-12.5), respectively, with the Spectra X Light engine. XCaMP-B emission was reflected off a quad wavelength dichroic mirror (Semrock, FF409/493/573/652-Di02) for various color light stimulation, and passed through a triple-band emission filter (Semrock, FF01-432/523/702-25). XCaMP-G emission was reflected off a dual wavelength dichroic mirror (Chroma, ZT488/594rpc) for orange light stimulation or another mirror (ZT488/640rpc) for red light stimulation, and passed through a 535-30–nm emission filter (Chroma, ET535/30m). Red-responsive opsins were activated with a Spectra X Light engine filtered either with 585 nm orange light (Semrock, FF01-585/29-25, 2.0 mW/mm^2) or 635 nm red light (Semrock, FF01-635/18-25, 2.0 mW/mm^2). For light sensitivity experiments, 434 nm blue light (Semrock, 434/17), 488 nm cyan light (Semrock, LL01-488-12.5), or 570 nm green light (Chroma, HQ570/20m) with 400 ms pulse-width was used at varying light power densities (in mW/mm^2) of 0.013, 0.066, 0.30 and 1.0.

Fluorescence of XCaMP-B or XCaMP-G was imaged using low-intensity 385 nm (10 $\mu W/mm^2$) or 488 nm (8 $\mu W/mm^2$) laser light, respectively, without substantially activating red-responsive opsin. Images were acquired at 20 Hz using MicroManager (http://micro-manager.org). Light for stimulation was controlled by LabVIEW (National Instruments) and applied every 10 sec at an exposure time of 10, 50, 200 and 800 msec. Imaging data were analyzed in MATLAB (MathWorks). Circular regions of interest (ROIs) were drawn manually based on the averaged image. We performed background subtraction before calculating Ca^{2+} signals. ΔF/F responses were calculated to normalize the signal in each ROI, by dividing by its mean value of total fluorescence intensity and subtracting 1. Noise was calculated as the standard deviation of the total ΔF/F fluctuation 3 sec before the stimulation. Signal-to-noise ratio (SNR) was then computed as ΔF/F response divided by noise. Peak amplitude was calculated from the maximum value during 2

sec after stimulus cessation. To compare red-responsive opsins to triggered XCaMP-G kinetics, we calculated 200 msec exposure-triggered Ca^{2+} transients. Rise time (tpeak) was defined as the time-to-peak from the cessation of the light stimulus to the time point at which maximal-amplitude fluorescence was reached. The decay constants (tau) were determined by single-exponential fit from the peak of the fluorescence response for 2 sec after stimulation.

FIP setup and analysis

We collected bulk fluorescence from targeted brain regions using a single optical fiber while delivering excitation light for fiber photometry as described previously (Inoue et al., 2019; Kim et al., 2016). We have extended these methods to the case of dual excitation wavelengths (380 and 470nm) with stimulation wavelength (590, 720, or 750 nm) delivered through the same fiber to allow tracking of activity in distinct cell populations (sender and receiver) during optogenetic stimulation of the sender population. A low fluorescence 400-μm-diameter 0.66-NA mono fiberoptic cannula (Doric Lenses) was implanted above mPFC for fiber photometry. Cannulas were secured to the skull using a base layer of adhesive dental cement (C&B-Metabond, Parkell), followed by a second layer of cranioplastic cement (Ortho-Jet, Lang). Experiments were conducted 4-6 weeks later for FIP recordings to allow for sufficient viral expression and postsurgery recovery. One end of the patchcord terminated in an SMA connector (Thorlabs, SM1SMA) mounted at the working distance of the objective, and the other end terminated in 2.5-mm-diameter stainless steel ferrules. These ferrules were coupled via bronze sleeves (Doric, SLEEVE_BR_2.5) to ferrules implanted into a mouse. Fiber faces were imaged through a 20×/0.75-NA objective (Nikon, CFI Plan Apo Lambda 20×) through a series of reconfigurable dichroic mirrors.

In the standard configuration, the three LEDs (M385F1, M470F3, and M595F2, Thorlabs) were filtered with 380-14 nm, 473 nm, and 586-20 nm bandpass filters (FF01-380/14-25, LL01-473-25, and FF01- 586/20-25, Semrock). Excitation and optogenetic stimulation light from two sources (470 and 590 nm) was passed to a 525 nm longpass dichroic mirror (T525lpxr, Chroma), and then combined with 380 nm light using a second 425 nm longpass dichroic (T425lpxr, Chroma) before finally being coupled into the optical fiber patch cord using a triple multiband dichroic (69013bs, Chroma). Fluorescence emission passed through multi-bandpass fluorescence emission filter (Semrock, FF01-425/527/685-25) for XCaMP-B and GCaMP6 recording. A 575 nm shortpass filter (Edmund, 575 nm 25 mm diameter, O.D. 4.0 Shortpass filter) was directed into the tube lens to minimize direct LED emission detected by the camera. Imaging optical powers at 380 nm and 470 nm were measured at the far end of the patch cord to be 5 μW and 2.5 μW, respectively. The fluorescence image was focused onto the sensor of a sCMOS camera (Hamamatsu, ORCA-Flash4.0) through a tube lens (Thorlabs, AC254-035-A-ML).

A custom MATLAB (Mathworks, Natick, MA) GUI was written to control the sample illumination protocol as well as provide power modulation pulses to the LEDs (National Instruments, NI PCIe-6343-X) which temporally align the respective LED illumination with camera frame acquisition (HCImage, Hamamatsu). The generic illumination protocol would repeat a sequence of three-frame sampling periods: one isosbestic at 380 nm, one signal at 470 nm and one optogenetic at >470 nm (Figure 7A). Maintaining a dedicated frame for optogenetic excitation faithfully removes any potential cross-excitation artifact from the isosbestic and signal sampling windows.

To quantify spectral cross-excitation of the opsin from signal illumination, the 470 nm LED was additionally pulsed during the optogenetic sampling period. The pulse duration of this additional illumination was matched to the signal pulse width (23 ms). The minimum excitation power for the sweep was equal to that used for the signal pulse (2.5 μW). The digital camera acquired data at a total of 30Hz. Therefore, due to the sequential 3-frame sampling protocol, the isosbestic and signal samples were each acquired at 10 Hz and all optogenetic stimulation would similarly occur at a rate of 10Hz. The duration of this 10 Hz optogenetic stimulation was 2 seconds. To quantify the excitation efficiency of the opsin to orange light at 594 nm, the associated LED was pulsed during the optogenetic sampling period (10 ms pulse width). For light-intensity sweeps, four samples at each power were randomly interleaved with a random ITI between 20 and 30 seconds. Optogenetic excitation in the NIR window at 720 nm and 750 nm were separately characterized using this same protocol (Inoue et al., 2019; Kim et al., 2016). For 720 nm optogenetic stimulation, the 594-nm LED was replaced with a 730-nm LED (M730L5, Thorlabs). The 730-nm laser was filtered with a 716-43 nm bandpass filter (Semrock, FF01-716/43-25). For 750 nm optogenetic stimulation, the 594-nm LED was replaced with a 750-nm laser (CivilLaser). The 750-nm laser was filtered with a 750-10 nm bandpass filter (Thorlabs, FB750-10).

The Pyr-PV impulse response data were acquired using the same optical configuration. A 594 nm LED was delivered using 10 ms pulse width and 1 mW of power. Four samples at each frequency and number were randomly interleaved with an ITI 30 seconds.

The fluorescence signal was calculated with custom written MATLAB scripts. We fit a double exponential to a thresholded version of the fluorescence time series and subtracted the best fit from the unthresholded signal to account for slow bleaching artifacts. Fluorescence signal was normalized within each mouse by calculating the ΔF/F as (F - baseline (F)) / baseline (F), where the baseline was taken from the average during 5 s before optogenetic stimulation. Peak ΔF/F amplitude was calculated from the maximum value during 2 s after the stimulus cessation. Noise was calculated as the standard deviation of the ΔF/F fluctuation during 5 s before optogenetic stimulation. Signal-to-noise ratio (SNR) response was then computed as ΔF/F response divided by noise. Every measurement point (light intensity and wavelength) represents the average of four trials at 20-30 second intervals. The optical EPD50 in Figure 7E was quantified by dividing the ΔF/F amplitude at each light intensity by the ΔF/F amplitude at 1 mW.

Histology and Confocal Microscopy

To analyze the expression pattern of opsin and GCaMP, immunohistochemistry was performed in brain tissue removed from virus-injected mice. Animals were anesthetized and transcardially perfused with ice-cold 1 × PBS followed by 4% paraformaldehyde (PFA) in PBS. Brains were dissected, post-fixed in the same fixatives overnight at 4 °C. Tissues were cut into 60-μm-thick slices with a vibratome (Leica, VT1000) and floated in PBS. For immunohistochemistry, brain slices were blocked with 3 % normal donkey serum / 0.3% Triton X-100 / PBS and incubated with primary antibody diluted in the blocking buffer at 4 °C overnight on a shaker. The antibody used was mouse monoclonal anti-HA tag (1:500, Fisher Scientific A26183). After washing with 0.3% Triton X-100 / PBS, tissue sections were incubated with the secondary antibody, Alexa Fluor 647-conjugated donkey anti-mouse antibody (1:500, A-31571, Thermo Fisher Scientific) and DAPI for 2 h at R.T. and mounted on slides in a tissue-mounting medium containing anti-fade, Polyvinyl alcohol mounting medium with DABCO (Millipore Sigma). Confocal imaging of GCaMP fluorescence, HA antibody staining for localization of the opsin, and DAPI for cytoarchitecture was performed using a Leica TCS SP8 or TCS SP5 confocal scanning laser microscope with a 10×/NA-0.4 or 25×/NA-0.95 water objective. Co-localization was performed using 25× images by annotating GCaMP6m expressing cell body locations and then overlaying these annotations and verifying expression in the anti-HA image. Quantitative analysis of GCaMP expression level of individual mice was performed using 10× image (5-6 z slices at 3 μm intervals through each section) by annotating GCaMP6m expression. The fluorescence intensity of GCaMP6m was quantified from the slice with the highest fluorescence intensity by setting up a 400 μm square ROI directly under the fiber tract using ImageJ (NIH).

QUANTIFICATION AND STATISTICAL ANALYSIS

For the electrophysiology experiments, pClamp 10.6 (Molecular Devices), Python, and Prism 7 (GraphPad) software were used to record and analyze data. Non-parametric tests (Wilcoxon rank-sum test and the signed rank test) were used for singular comparisons. For multiple comparisons, Kruskal-Wallis test was performed and was followed by Dunn's test for post-hoc comparisons. The peak photocurrent was identified as the largest difference in current in the interval from laser onset to laser offset. Tau-off was calculated by fitting a mono exponential curve to the waveform from laser offset to the baseline. Time-to-peak was calculated by measuring the time difference between laser onset and peak current.

To calculate action spectra, we first normalized photocurrents to the peak photocurrent for each cell. Then, these normalized spectra were averaged across cells to produce the action spectra for each opsin variant in both one-photon and two-photon measurements. To calculate EPD50, photocurrents were first normalized to the photocurrent elicited at the highest light power. Linear interpolation was then used to infer the light power level that produced 50% of the max photocurrent.

CellPress
OPEN ACCESS

Supplemental figures

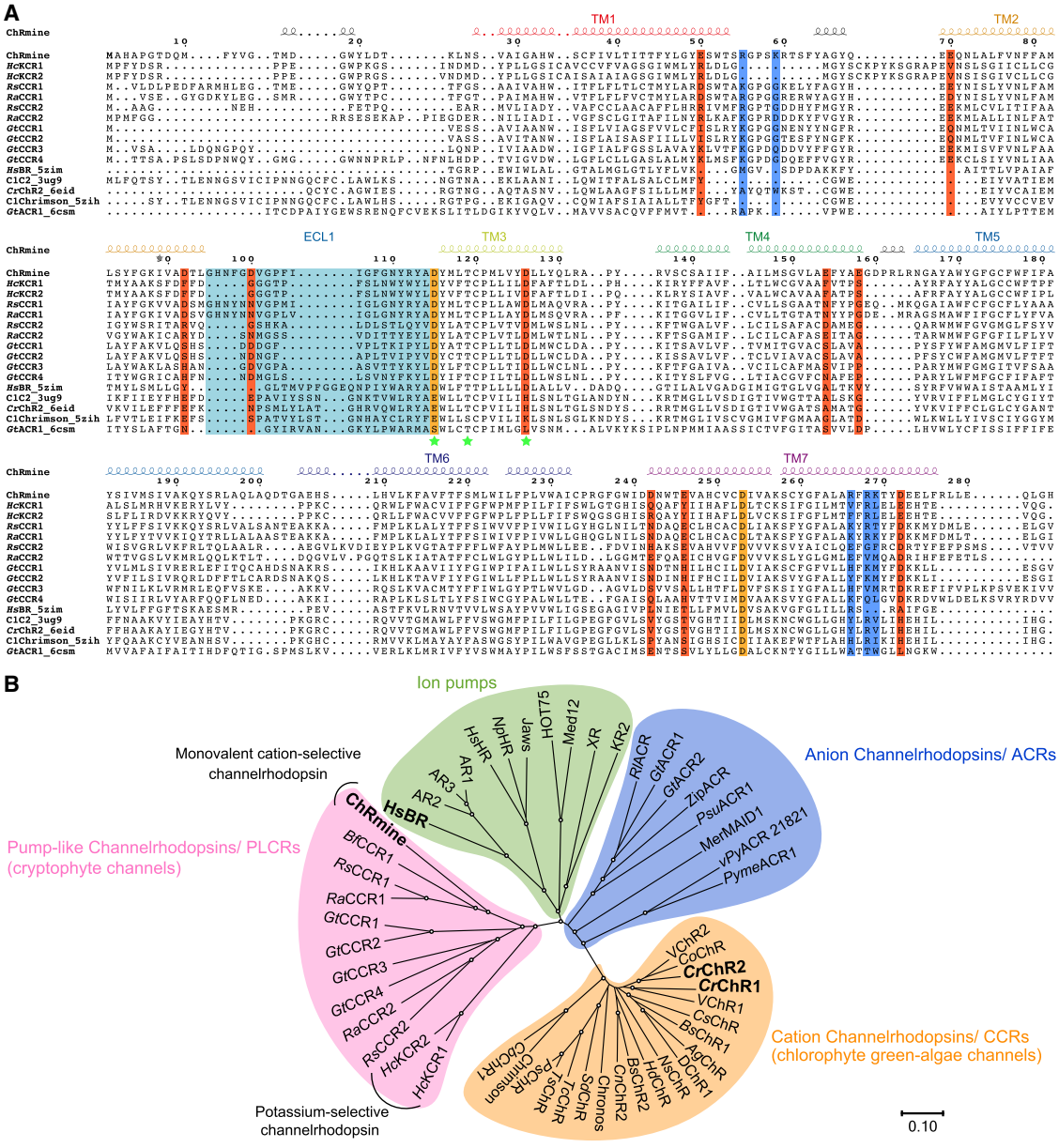

(legend on next page)

Figure S1. Structure-based sequence alignment, phylogenetic tree, and predicted structure of ChRmine, related to Figure 1

(A) The sequences are ChRmine (GenBank: QDS02893.1), *Hc*KCR1 (GenBank: MZ826862) (Govorunova et al., 2021), *Hc*KCR2 (GenBank: MZ826861) (Govorunova et al., 2021), *Ra*CCR1 (GenBank: QIU80793.1), *Rs*CCR1 (GenBank: QIU80800.1), *Ra*CCR2 (GenBank: QIU80796.1), *Rs*CCR2 (GenBank: QIU80801.1), *Gt*CCR1 (GenBank: ANC73520.1), *Gt*CCR2 (GenBank: ANC73518.1), *Gt*CCR3 (GenBank: ANC73519.1), *Gt*CCR4 (GenBank: ARQ20888.1), *Hs*BR (PDB: 5ZIM) (Hasegawa et al., 2018), C1C2 (PDB: 3UG9) (Kato et al., 2012), *Cr*ChR2 (PDB: 6EID) (Volkov et al., 2017), C1Chrimson (PDB: 5ZIH) (Oda et al., 2018), *Gt*ACR1 (PDB: 6CSM) (Kim et al., 2018), *Cr*ChR1 (GenBank: AAL08946.1), VChR1 (GenBank: ABZ90900.1), VChR2 (GenBank: ABZ90902.1), Chronos (GenBank: KF992040.1), *Gt*ACR2 (GenBank: AKN63095.1), *Rl*ACR (GenBank: APZ76712.1), MerMAID1 (GenBank: QCW06519.1) (Oppermann et al., 2019), *Pyme*ACR1 (GenBank: QNU12853.1) (Rozenberg et al., 2020), v*Py*ACR_21821 (GenBank: QNU12854.1) (Rozenberg et al., 2020), *Hs*HR (PDB: 1E12) (Kolbe et al., 2000), *Med12*BPR (PDB: 4JQ6) (Ran et al., 2013), XR (PDB: 3DDL) (Luecke et al., 2008), and KR2 (PDB: 3X3B) (Kato et al., 2015b). The sequence alignment was created using PLOMALS3D (Pei et al., 2008) and ESPript 3 (Robert and Gouet, 2014) servers. Secondary structure elements for ChRmine are shown as coils. Positively and negatively charged residues are highlighted in blue and red, respectively. Green stars represent the DTD motif. The ECL1 of ChRmine is colored light blue. The counterions are colored orange.

(B) An unrooted phylogenetic tree was drawn for representative microbial rhodopsins using the neighbor-joining method (Saitou and Nei, 1987), and 1,000 bootstrap replicates. Evolutionary analyses were conducted in MEGA7 (Kumar et al., 2016). White circles represent bootstrap values >85%.

(C–F) Five predicted models of ChRmine, generated using locally installed AlphaFold2. The ribbon representations are colored by the pLDDT score (low, red; high, cyan).

(C) Plots of the pLDDT score.

(D) The best predicted model superimposed onto the cryo-EM structure (yellow).

(E and F) The detailed comparison of ECL1 (E) and the Schiff base region (F) between the five predicted models and cryo-EM structure. Notably, the C-terminal region of ECL1, including D115, has high pLDDT scores, but the conformation of D115 is not correctly predicted.

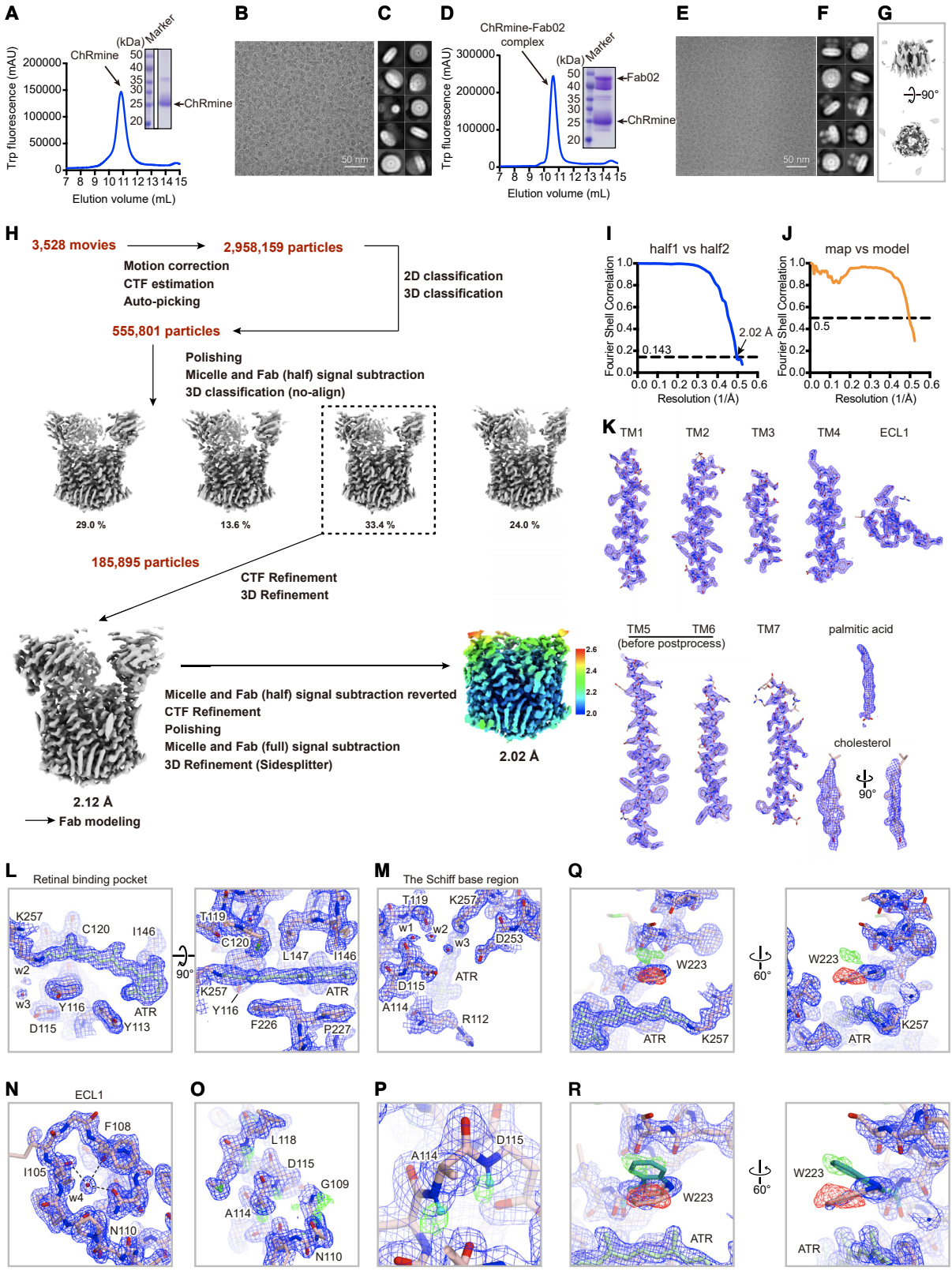

(legend on next page)

Figure S2. Cryo-EM analysis of the ChRmine and ChRmine-Fab02 complex, related to Figure 1

(A–C) Panels corresponding to ChRmine alone. Representative SEC trace with SDS-PAGE as inset (A), representative cryo-EM micrograph (B), and 2D-class averages (C).

(D–F) Panels corresponding to the ChRmine-Fab02 complex. Representative SEC trace with SDS-PAGE as inset (D), representative cryo-EM micrograph (E), and 2D-class averages (F).

(G) Low-resolution reconstruction of ChRmine alone.

(H) Data processing workflow of the ChRmine-Fab02 complex. Final cryo-EM map colored by local resolution.

(I) Fourier shell correlation (FSC) between the two independently refined half-maps.

(J) FSC between the model and the map calculated for the model refined against the full reconstruction.

(K–N) Cryo-EM density (FSC-weighted sharpened map calculated by RELION3.1.1) and model for ChRmine, lipids (K), the retinal binding pocket (L), the Schiff base region (M), and twisted ECL1 (N).

(O and P) Density and model near ECL1 region. FSC-weighted sharpened map calculated by RELION3.1.1 (blue) and F_o-F_c map calculated by Servalcat (green). Positive F_o-F_c difference densities (4.3σ, where σ is the standard deviation within the mask) are observed near nitrogen atoms, suggesting that these densities represent hydrogen atoms.

(Q and R) Possible signal of early photo-intermediate. (Q) Density and model in the retinal binding pocket region. Blue and green maps are FSC-weighted sharpened map calculated by RELION3.1.1 and F_o-F_c maps calculated by Servalcat, respectively. Positive and negative F_o-F_c difference density pairing ($\pm$3.7σ, where σ is the standard deviation within the mask) is observed around W223, suggesting that this density contains information regarding a small population of the early intermediate state, and that W223 moves upward early in the photocycle. (R) Magnified views of (Q).

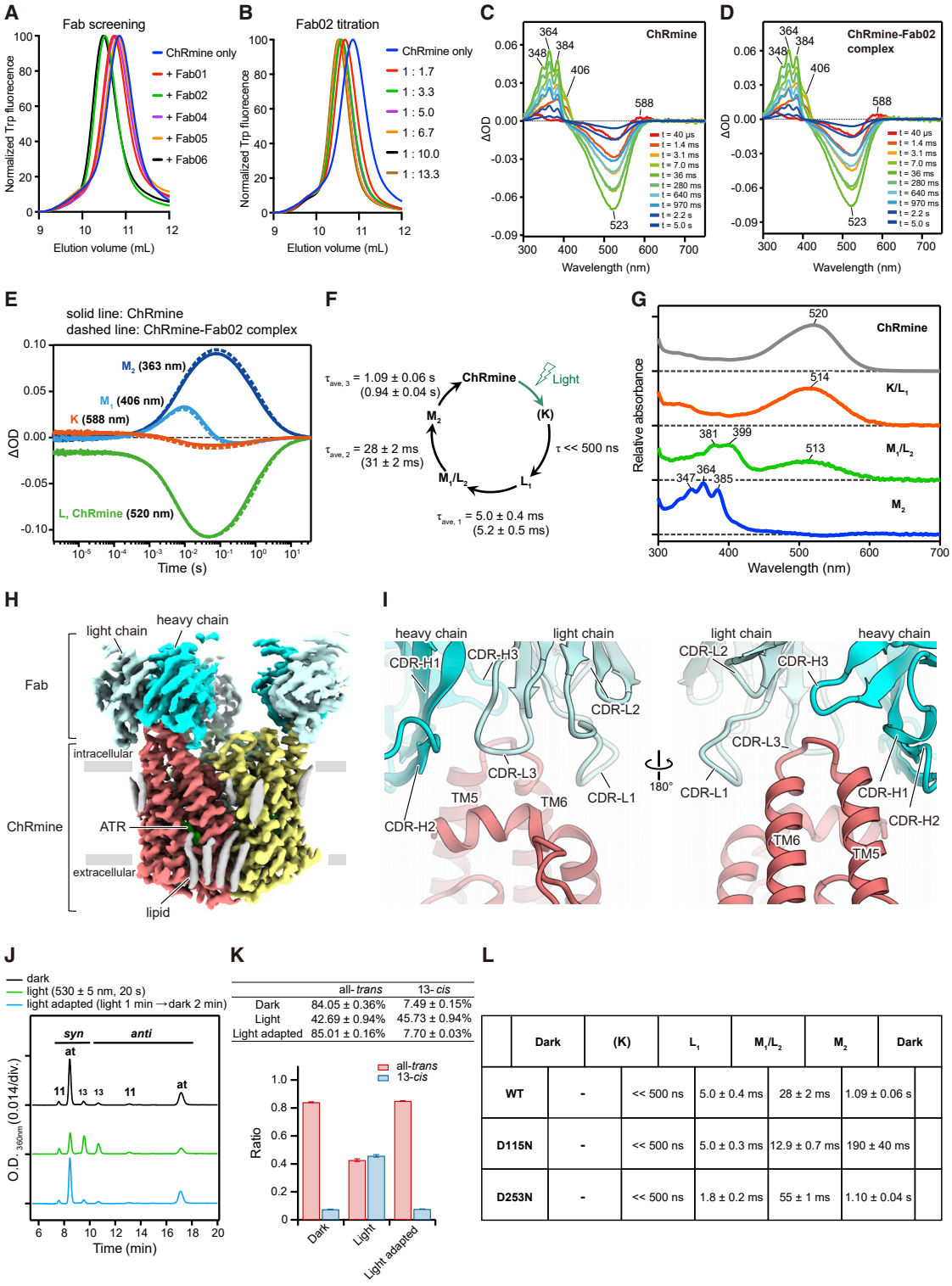

Figure S3. Spectroscopic, structural, and HPLC characterization of the ChRmine and ChRmine-Fab02 complex, related to Figure 1

(A) FSEC screening of Fab fragments.

(B) Titration of the Fab02 fragment against ChRmine.

(C and D) Transient absorption spectra of ChRmine WT (C) and the ChRmine-Fab02 complex (D) excited at λ_{exc} = 532 nm.

(legend continued on next page)

(E) Time-series traces of absorption changes of ChRmine WT (solid line) and the ChRmine-Fab02 complex (dashed line) at 363 (blue), 406 (cyan), 520 (green), and 588 nm (red) probe wavelengths.
(F) Photocycle scheme of ChRmine determined by flash photolysis shown in (E). The lifetimes of ChRmine-Fab02 are shown in parentheses.
(G) The absorption spectra of the initial state (gray), L_1 (orange), M_1/L_2 (green), and M_2 (blue) of ChRmine calculated from the decay-associated spectra of transient absorption changes (Inoue et al., 2013).
(H) Cryo-EM map of the ChRmine-Fab02 complex.
(I) Interactions between ChRmine and Fab02.
(J and K) HPLC analysis of the chromophore configuration of ChRmine. (J) Representative HPLC profiles of the chromophore of ChRmine in the dark (top), under illumination (middle), and after light adaptation (bottom). "At," "11," and "13" indicate the peak of all-*trans*-, 11-*cis*-, and 13-*cis*-retinal oximes, respectively. (K) Calculated composition of all-*trans*- and 13-*cis*-retinal oximes. Data are presented as mean ± SEM (n = 3). Purified samples of ChRmine were prepared with additional supplementation of all-*trans* retinal. Green light (530 ± 5 nm) was used for illumination. Light adaptation was achieved by illumination for 1 min followed by incubation in the dark for 2 min.
(L) Lifetime of each intermediate in ChRmine WT and mutants.

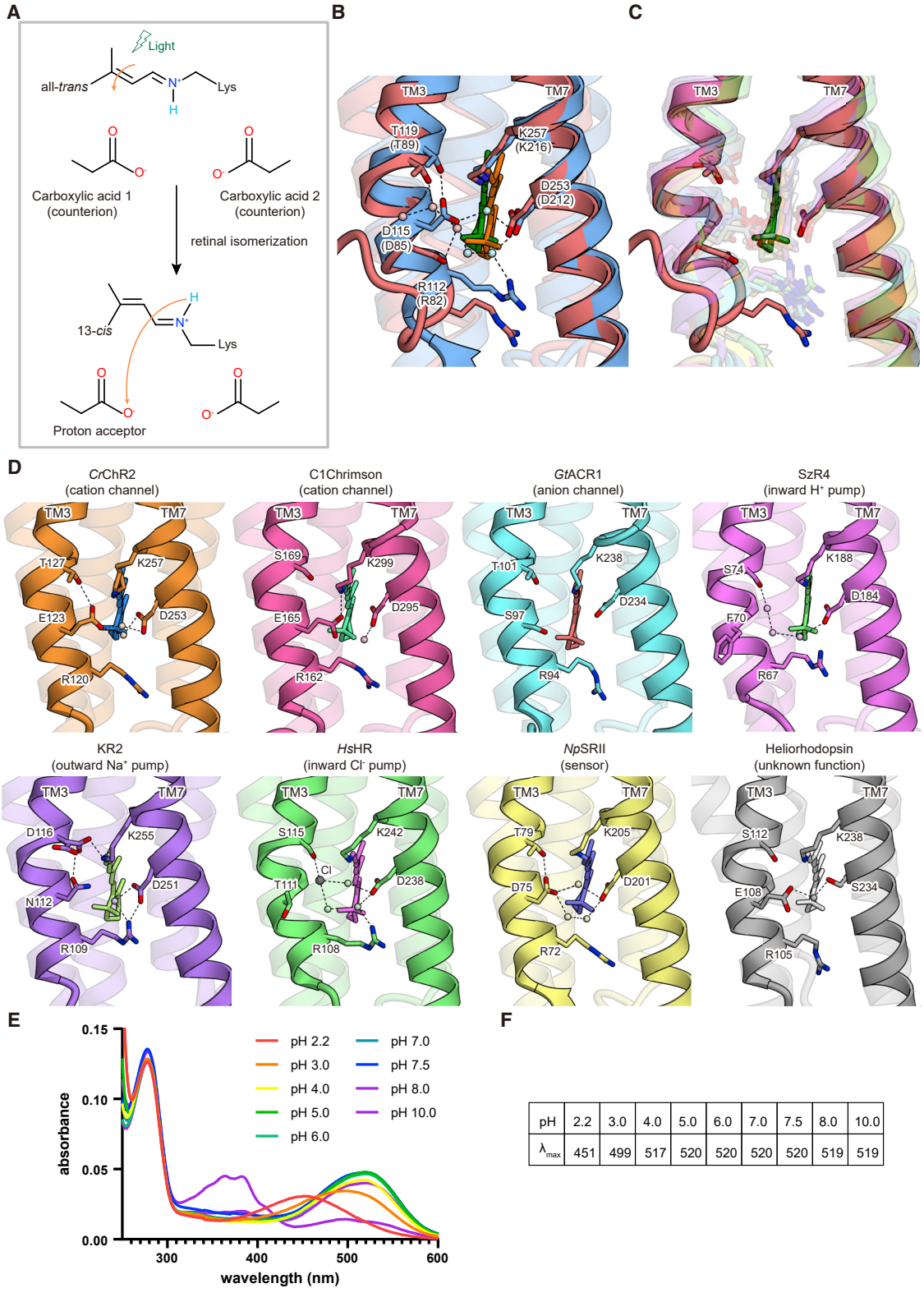

pH	2.2	3.0	4.0	5.0	6.0	7.0	7.5	8.0	10.0
λ_{max}	451	499	517	520	520	520	520	519	519

(legend on next page)

Figure S4. Comparison of the Schiff base regions, related to Figure 2

(A) Concept of the Schiff base counterions and proton acceptor.

(B) The superposed Schiff base region of ChRmine (red) and *Hs*BR (blue). Red and blue spheres represent water molecules of ChRmine and *Hs*BR, respectively. Black dashed lines represent hydrogen bonds.

(C) Superposed Schiff base region of ChRmine (red) and representative microbial rhodopsins (*Cr*ChR2 [Volkov et al., 2017], C1Chrimson [Oda et al., 2018], *Gt*ACR1 [Kim et al., 2018], schizorhodopsin 4 [SzR4] [Higuchi et al., 2021], KR2 [Kato et al., 2015b], *Hs*HR [Kolbe et al., 2000], *Np*SRII [Gordeliy et al., 2002], heliorhodopsin [Shihoya et al., 2019]), displayed with high transparency except for ChRmine.

(D) List of the Schiff base regions of representative microbial rhodopsins.

(E and F) pH titration experiment of WT ChRmine. (E) Absorption spectra of WT ChRmine measured from pH 2.2 to 10.0. (F) The λ_{max} value at each pH.

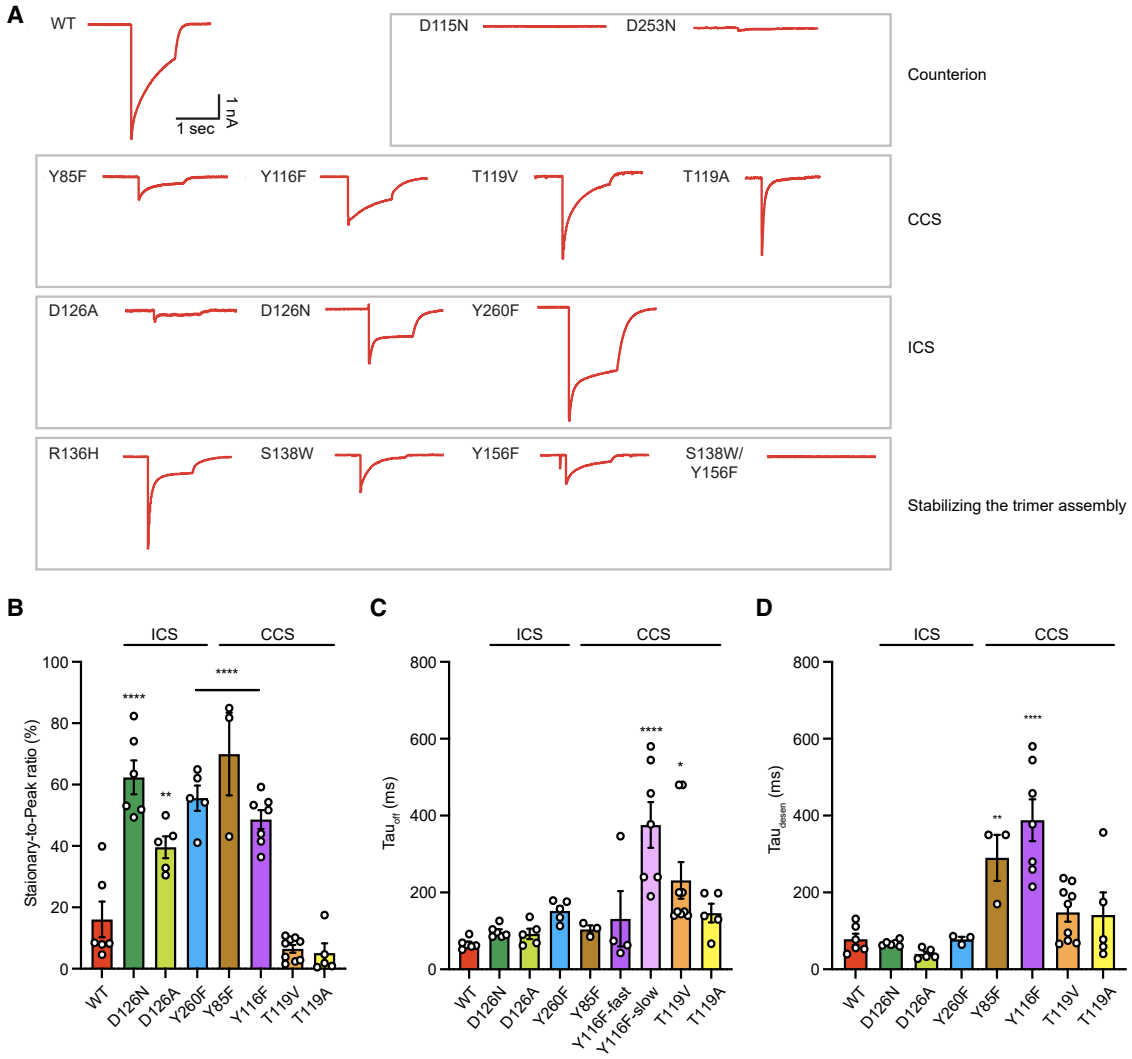

Figure S5. Electrophysiology, related to Figures 2–4

(A) Representative traces of ChRmine WT and 13 mutants expressed in HEK293 cells by lipofectamine transfection, measured at −70 mV holding potential in voltage clamp. Traces were recorded while cells were stimulated with 1.0 s of 1 mW mm^{-2} irradiance at 580 nm.

(B–D) Summary of the steady-to-peak ratio of photocurrents (B), τ_{off} of channel closing (C), and τ_{off} of channel desensitization (=τ_{desen}) (D). Mutants are categorized as the mutants of counterions, central constriction site (CCS), intracellular constriction site (ICS), and the trimer interface. Data are mean ± S.E.M (n = 3–9); one-way ANOVA followed by Dunnett's test. *p < 0.05, **p < 0.01, ***p < 0.001, and ****p < 0.0001.

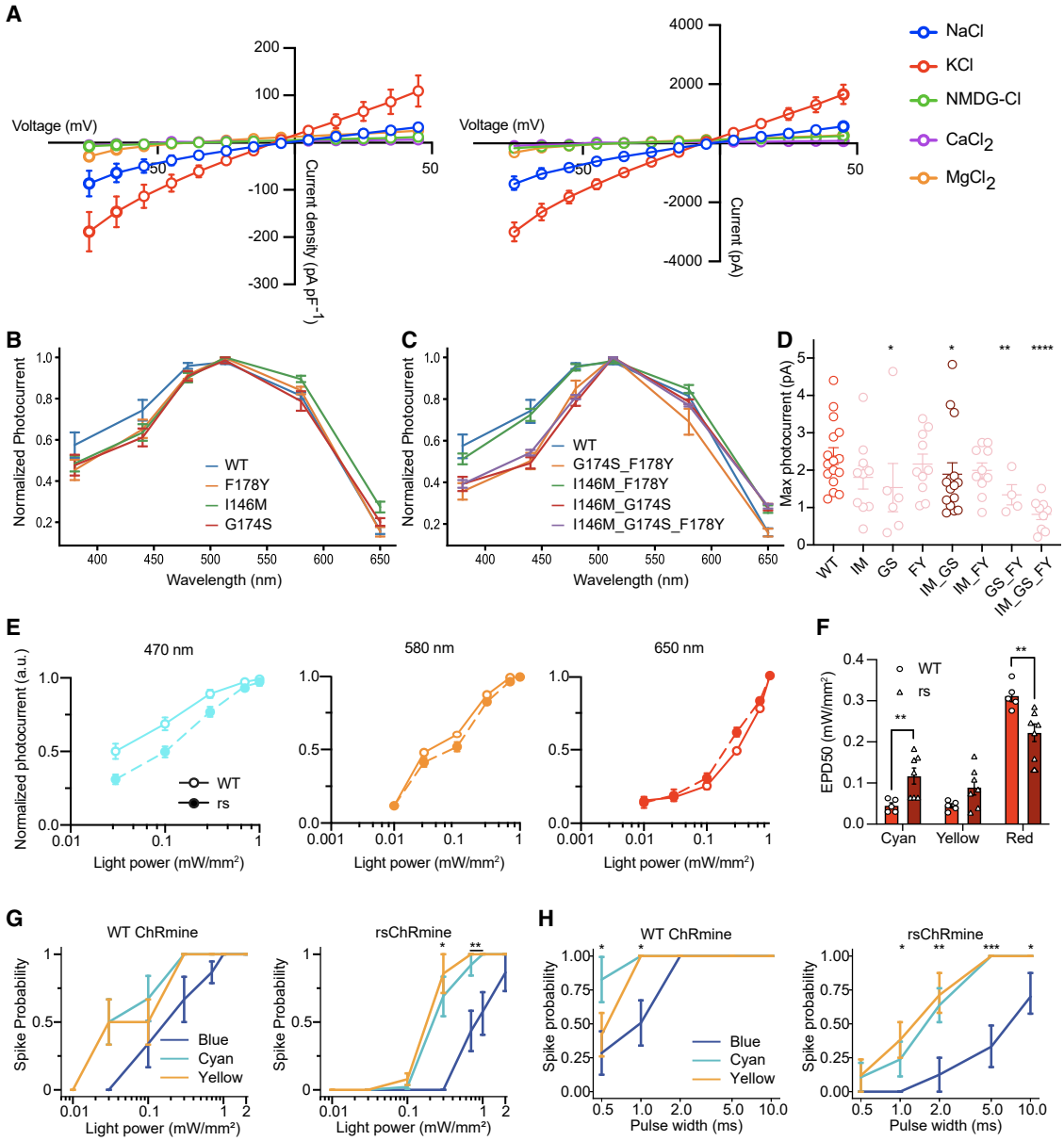

Figure S6. Detailed characterization of rsChRmine, related to Figure 5

(A) The current-voltage dependence of non-normalized (left) and normalized (right) peak photocurrents of ChRmine at different voltages from −75 to 45 mV stimulated with 1 s of 1 mW mm^{-2} irradiance at 580 nm (n = 6–10).

(B and C) Action spectra of single (B), double, and triple (C) mutants of residues in the RBP (n = 4–16).

(D) Peak photocurrents for RBP mutants (n = 4–16, Kruskal-Wallis test with Dunn's test, asterisks denote comparisons with WT ChRmine, *p < 0.05, **p < 0.01, and ****p < 0.0001).

(E) Normalized photocurrent versus light power in cultured neurons with cyan (470 nm), orange (585 nm), and red (650 nm) light (n = 5 for WT and 7 for rs).

(F) Effective power density (EPD50) of WT and rsChRmine (two-tailed Student's t test, n = 5 for WT and 7 for rs, *p < 0.05, **p < 0.01, ***p < 0.001, and ****p < 0.0001).

(G and H) Spike probability versus light intensity (G) and pulse width (H) in cultured neurons expressing opsins (n = 6 for WT and 7 for rs, Kruskal-Wallis test with Dunn's test). All data are mean ± SEM, and sample size n denotes the number of cells unless otherwise noted. *p < 0.05, **p < 0.01, ***p < 0.001, and ****p < 0.0001.

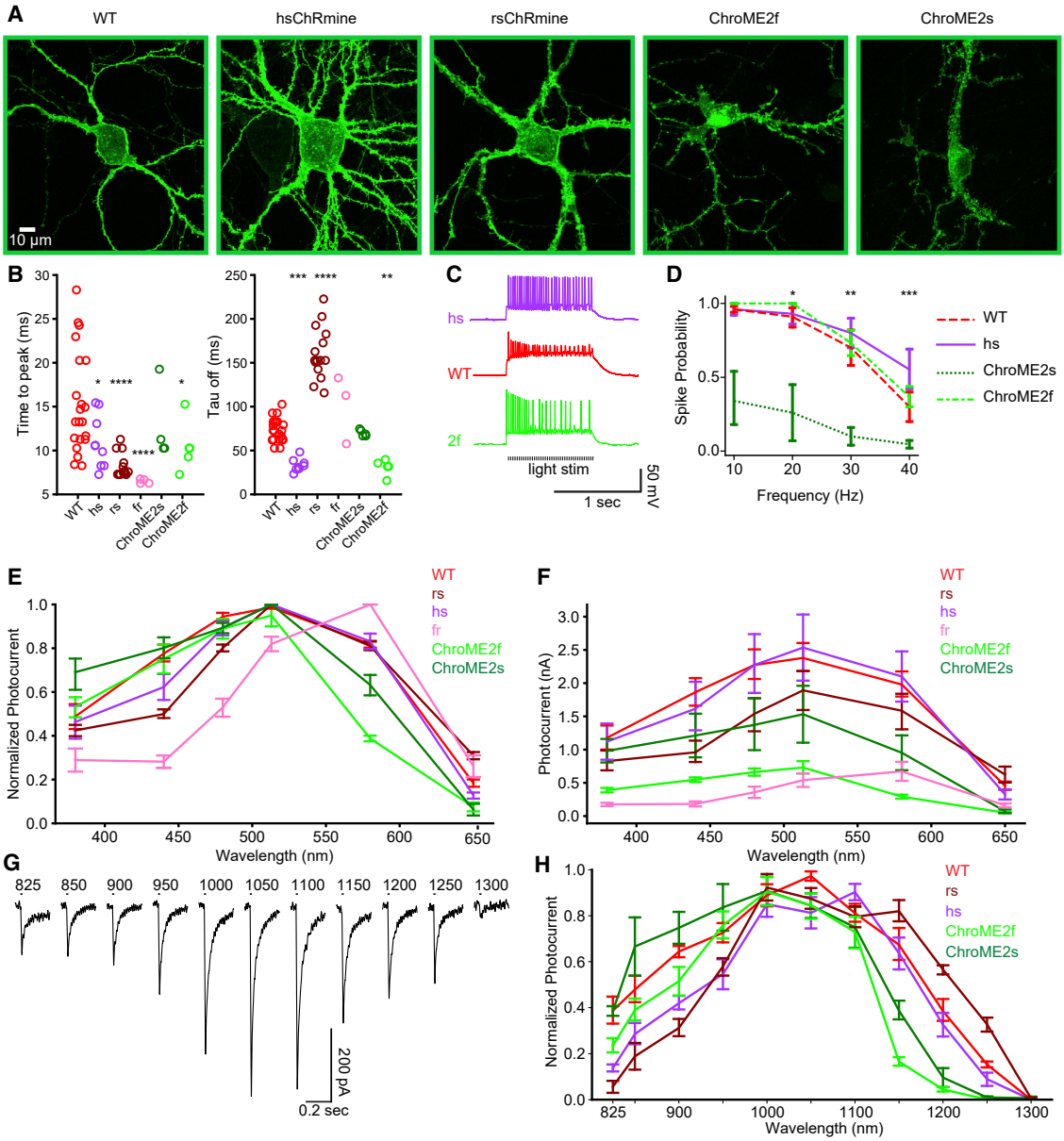

Figure S7. Detailed comparison of ChRmine with ChroME variants, related to Figure 5

(A) Confocal images of WT ChRmine-, hsChRmine-, rsChRmine-, ChroME2f-, and ChroME2s-expressing cultured neurons. Scale bars, 10 µm.

(B) Summary of on (left) and off (right) kinetics of ChRmine and ChroME variants (n = 3–23, Kruskal-Wallis test with Dunn's test. Asterisks denote comparisons with WT ChRmine, *p < 0.05, **p < 0.01, ***p < 0.001, and ****p < 0.0001).

(C) Example current clamp traces of hsChRmine-, WT ChRmine- and ChroME2f-expressing neurons with light stimulation.

(D) Summary of opsin spike fidelity (n = 5 for all mutants, Kruskal-Wallis test with Dunn's test. Asterisks denote comparisons between ChroME2s and WT ChRmine, *p < 0.05, **p < 0.01, and ***p < 0.001).

(E and F) Normalized (E) and peak photocurrent (F) action spectra of ChRmine and ChroME variants (n = 4–16).

(G and H) Example traces of rsChRmine (G) and normalized action spectra (H) of ChRmine and ChroME variants under two-photon excitation (n = 4–6). All data are mean ± SEM, and the sample size n denotes the number of cells unless otherwise noted. For WT ChRmine (compared here under identical conditions alongside other ChRs in the same preparation for rigorous and unbiased comparison of performance regarding photocurrents, action spectra, spike frequency-response, and EPD50), we observed slightly lower spike fidelity than had been observed in Marshel et al. (2019); this can be seen with preparation-to-preparation variance of opsin expression level in cultured neurons.